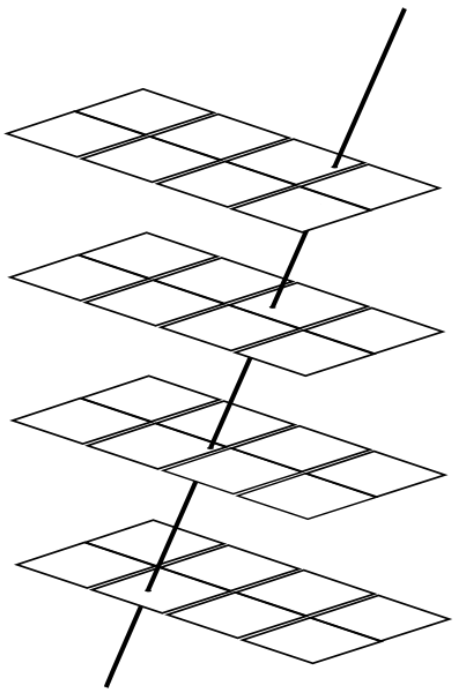
Development and Implementation of a Particle Tracking System Based on Monolithic Active Pixel Sensors



Lennart Halstenberg

2026



MASTER THESIS

Development and Implementation of a Particle Tracking System Based on Monolithic Active Pixel Sensors

submitted by:

Lennart Halstenberg

Münster, 30. Juni 2026

First examiner:

Prof. Dr. Anton Andronic

Second examiner:

Jun-Prof. Dr. Denise Aparecida Moreira de Godoy Willems

Abstract

The work is carried out within the context of the planned ITS3 detector upgrade of the ALICE experiment at CERN, in which the three innermost layers of the Inner Tracking System will be replaced by bent, wafer-scale **M**onolithic **A**ctive **P**ixel **S**ensors (MAPS). This thesis focuses on the commissioning and operation of a particle tracking system based on the babyMOSS, a MAPS prototype developed as part of the ITS3 project. To enable a quantitative analysis of the measurements, a complete reconstruction chain based on *Python3* was implemented, substituting the existing *Corryvreckan* framework, which is not optimally adaptable to the local requirements.

The commissioning and operation of the local setup, as well as the measurement and reconstruction of atmospheric muon trajectories, were successful. The developed framework was validated using both simulated data, measurements of atmospheric muons and data collected during the ITS3 test-beam campaign at the ELSA accelerator in February 2025. The limitations encountered in measuring atmospheric muons were predominantly attributed to the small number of reconstructable tracks, significant multiple scattering of low-energy muons, and residual misalignment. Moreover, the observed event rate was about a factor of four lower than anticipated, which requires further investigation and optimization. In contrast, applying the framework to the data collected at ELSA showed that a sub-binary estimation of the spatial resolution and that the detection efficiency was feasible, thus confirming the overall functionality of the reconstruction chain. Systematic discrepancies in the order of an approximated 5% with respect to reference measurements persist and are mainly ascribed to the use of a simplified straight-line track model and to a not fully recoverable misalignment.

Contents

1 Introduction **1**

2 Experimental Context: ALICE & ITS3 **3**

2.1 ALICE . . . 3

2.1.1 Semiconductor Tracking Detectors . . . 4

2.1.2 ITS3 . . . 6

3 Fundamentals of Semiconductor Pixel Detectors **9**

3.1 Interactions of Particles with Matter . . . 9

3.1.1 Energy Loss of Charged Particles . . . 9

3.2 Semiconductor Particle Detectors . . . 13

3.3 Semiconductor Pixel Detector . . . 17

3.3.1 Position Measurement by Segmentation . . . 17

3.3.2 Hybrid Pixel Detectors . . . 18

3.3.3 **M**onolithic **A**ctive **P**ixel **S**ensors (MAPS) . . . 19

4 The babyMOSS Sensor **21**

4.1 The MOSS and the babyMOSS . . . 21

4.1.1 The **Mo**nolithic **S**titched **S**ensor (MOSS) . . . 21

4.1.2 The babyMOSS . . . 22

4.1.3 The In-Pixel Front-End . . . 23

4.1.4 Readout Cycle . . . 24

4.1.5 The babyMOSS Test System . . . 25

4.2 Characterization Measurements . . . 26

4.2.1 **F**ake **H**it **R**ate (FHR)-scan . . . 26

4.2.2 **Thr**eshold (THR)-scan . . . 27

5 Beam Telescopes and Local Tracking System **29**

5.1 Tracking Telescopes & babyMOSS Beam Telescope . . . 29

5.1.1 Working Principle of a Beam Telescope . . . 29

5.2 Testbeam at ELSA . . . 32
5.2.1 The ELSA Facility and the E3 Beamline . . . 32
5.2.2 Experimental Setup at ELSA . . . 34
5.3 Local Tracking System . . . 35
5.3.1 Atmospheric Muons . . . 35
5.3.2 Mechanical Construction and Readout Chain . . . 38
5.3.3 Threshold and Fake-Hit-Rate Characterization . . . 39

6 Reconstruction and Analysis Framework **43**
6.1 Corryvreckan . . . 43
6.2 The Python3-Based Framework . . . 46
6.2.1 Telescope and Eventreader . . . 46
6.2.2 Tracking . . . 47
6.2.3 Simulation . . . 49
6.2.4 Alignment Procedure . . . 52
6.2.5 DUT Sensor Characterization . . . 56

7 Results **59**
7.1 General Parameters for Simulation and Data Processing . . . 59
7.2 Validation of the Track Reconstruction Algorithm and Expected Performance 61
7.3 Local Tracking System . . . 63
7.3.1 Simulations . . . 64
7.3.2 Data Analysis . . . 71
7.4 ELSA Setup . . . 80
7.4.1 Simulation . . . 81
7.4.2 Data Analysis . . . 83
7.5 Summary . . . 90
7.5.1 Measurement of Atmospheric Muons with the Local Tracking System 90
7.5.2 Validation of the Python-based Framework . . . 90

8 Conclusion **93**

9 Outlook **95**
9.1 Local Tracking System . . . 95
9.2 **A** **L**arge **I**on **C**ollider **E**xperiment (ALICE)3 . . . 97

Bibliography **99**

Appendix **103**

A Uncertainties and Statistical Methods 103
A.1 General Uncertainties and Statistical quantities 103
A.2 Histograms and Gaussian Fits 105
A.3 Trigger Rates 105
A.4 Peak Determination 108
A.5 Spatial Resolution and Detection Efficiency 108
B Parameters 109
C Geometries 110
D Sensor Characterization 114
E Alignment 121
E.1 Local Setup 121
E.2 ELSA 124

Acknowledgments **127**

Acronyms

APTS	**A**nalog **P**ixel **T**est **S**tructure
ALICE	**A** **L**arge **I**on **C**ollider **E**xperiment
ALMIRA	**AL**ICE3 **M**onolithic **I**ntegrated t**R**acking **A**sic
ATLAS	**A** **T**oroidal **L**HC **A**pparatu**S**
bb	**B**ottom half unit
CERN	**C**onseil **E**uropéen pour la **R**echerche **N**ucléaire
CMOS	**C**omplementary **M**etal-**O**xide-**S**emiconductor
CMS	**C**ompact **M**uon **S**olenoid
DAC	**D**igital **A**nalog **C**onverter
DAQ board	**D**ata **A**c**Q**uisition board
DESY	**D**eutsches **E**lektronen-**S**ynchrotron
dof	**d**egrees **o**f **f**reedom
DPTS	**D**igital **P**ixel **T**est **S**tructure
DUT	**D**evice **u**nder **T**est
ECal	**E**lectromagnetic **Cal**orimeter
ELSA	**EL**ektronen-**S**tretcher-**A**ccelerator
EMCal	**E**lectro**M**agnetic **Cal**orimeter
ENC	**E**quivalent **N**oise **C**harge
FCT	**F**orward **C**onversion **T**racker
FHR	**F**ake **H**it **R**ate
FPC	**F**lexible **P**rinted **C**ircuit
FPGA	**F**ield-**P**rogrammable **G**ate **A**rray
HEP	**H**igh **E**nergy **P**hysics
HMPID	**H**igh **M**omentum **P**article **I**dentification **D**etector
HU	**H**alf **U**nit

IT	**I**nner **T**racker
ITS	**I**nner **T**racking **S**ystem
ITS3	ALICE **I**nner **T**racking **S**ystem **3**
LHC	**L**arge **H**adron **C**ollider
LHCb	**L**arge **H**adron **C**ollider **b**eauty
LINAC	**LIN**ear **AC**celerator
LS	**L**ong-**S**hutdown
MAPS	**M**onolithic **A**ctive **P**ixel **S**ensors
MID	**M**uon **I**dentifier **D**etector
MIP	**M**inimal **I**onizing **P**article
ML	**M**iddle **L**ayers
MOSS	**Mo**nolithic **S**titched **S**ensor
MPV	**M**ost **P**robable **V**alue
OT	**O**uter **T**racker
PCB	**P**rinted **C**ircuit **B**oard
PID	**P**article **ID**entification
PMT	**P**hoto**M**ultiplier **T**ube
PTH	**P**ressure, **T**emperature, and **H**umidity
QCD	**Q**uantum **C**hromo **D**ynamic
QGP	**Q**uark-**G**luon-**P**lasma
RICH	**R**ing-**I**maging **CH**erenkov Detector
RMS	**R**oot **M**ean **S**quare
ROI	**R**egion **O**f **I**nterest
RSU	**R**epeated **S**ensor **U**nit
tb	**T**op half unit
TDR	**T**echnical **D**esign **R**eport
THR	**Thr**eshold
TOF	**T**ime **O**f **F**light
TPC	**T**ime **P**rojection **C**hamber
TRD	**T**ransition **R**adiation **D**etector
VD	**V**ertex Detector

1. Introduction

In the process of gathering an understanding of what is commonly referred to as physical reality, progress arises from an interdependent interplay between theoretical modeling and experimental measurement. The latter is determined not only by the intrinsic physical properties and limitations of the measurement apparatus, but also by the theoretical models and assumptions that employ the reconstruction of the phenomena of interest. In **H**igh **E**nergy **P**hysics (HEP), measurements are typically performed using complex detector systems that require sensors manufactured with high precision, as well as an accurate event modeling, in order to extract reliable information about the physical processes under investigation.

This thesis is situated within the broader framework of the planned upgrades to the ALICE experiment at CERN, which is dedicated to the study of ultra-relativistic heavy-ion collisions. A central scientific objective of ALICE is the investigation of **Q**uantum **C**hromo **D**ynamic (QCD), the fundamental theory describing the strong interaction. In particular, the experiment aims to study the **Q**uark-**G**luon-**P**lasma (QGP), a state of matter in which quarks and gluons are deconfined and can, for a short time, exist as quasi-free particles. Since the QGP itself cannot be observed directly, only the particles emerging from it, the ALICE detector comprises a large number of sub-detectors specialized in measuring these particles. Among these, the **I**nner **T**racking **S**ystem (ITS) plays a crucial role in determining the trajectories of charged particles with high precision. The primary objective of the forthcoming ALICE **I**nner **T**racking **S**ystem **3** (ITS3) upgrade is to enhance the tracking performance of the ITS by employing bent, wafer-scale MAPS sensors.

Recent advances in photolithographic processing have enabled several innovative approaches, including stitching techniques to fabricate wafer-scale sensors, as implemented in the ITS3 project, and the production of large-area tracking sensors, as planned for the future ALICE3 experiment.

The primary objective of this thesis is the commissioning and operation of a particle-tracking setup based on the babyMOSS sensor, a MAPS prototype developed within the ITS3 project, thereby establishing a robust foundation for subsequent activities such as local sensor tests, possible characterization measurements, and the potential development of a laboratory course for students.

In parallel with the work presented in this thesis, several test-beam sensor characterization campaigns for the ITS3 project were participated in, both to contribute to the overall project effort and to acquire practical experience in the operation and application of the sensors. Since these activities do not directly address the central research question of the present study, they will not be discussed in further detail, except where they are pertinent to the scope of this work.

To contextualize the content of this thesis, Chapter 2 provides a concise introduction to the scientific relevance of silicon pixel tracking detectors, embedded within an overview of the forthcoming ITS upgrade at ALICE. Subsequently, Chapter 3 presents the fundamental operating principles of silicon pixel sensors. This is followed in Chapter 4 by a detailed description of the babyMOSS device employed in the present study, and in Chapter 5 by a comprehensive overview of the detector configurations and particle sources used in the measurements.

To enable quantitative interpretation of the measurement results, the thesis further aims to implement a complete reconstruction chain, including track reconstruction, detector alignment, and, ultimately, sensor characterization, as introduced in Chapter 6. Because the reliability of any measurement is inherently tied to the validity of the underlying models, the proposed framework is systematically assessed for limitations arising from simplifying assumptions in Chapter 7. In a first step, this assessment was carried out using implemented simulation tools and data collected with babyMOSS tracking setups. As the Physics Department of the University of Münster does not operate a particle accelerator, this work is part of a long-standing tradition of using atmospheric muons as a source of high-energy particles. This approach was used, on the one hand, to assess the performance of the experimental setup and the developed reconstruction framework and, on the other hand, to examine whether precise sensor characterization is achievable under these conditions. To further evaluate the developed framework, data from an ITS3 test-beam campaign recorded at the ELSA electron accelerator were analyzed to perform a qualitative review of the full reconstruction-chain.

2. Experimental Context: ALICE & ITS3

This section contextualizes the frame in which the works for this thesis have been carried out. As the central objective of this thesis is the operation of the babyMOSS prototype sensors, which are a result of the ALICE ITS3 project, the following chapter will begin with a general presentation of the ALICE detector in Section 2.1. This will be followed by a general introduction to semiconductor pixel trackers in Section 2.1.1 to provide a summary of their conceptual working principle and their key parameters. The section will be followed by a brief overview of the planned ITS3 upgrade in Sec. 2.1.2.

2.1. ALICE

A **L**arge **I**on **C**ollider **E**xperiment (ALICE) is one of the four large-scale experiments installed at the **L**arge **H**adron **C**ollider (LHC). The LHC is a synchrotron accelerator with a circumference of 27.7 km, located at **C**onseil **E**uropéen pour la **R**echerche **N**ucléaire (CERN). It constitutes the final stage of the CERN accelerator complex and provides proton–proton collisions at a center-of-mass energy of $\sqrt{s} = 13.6\,\text{TeV}$, as well as nucleon–nucleon center-of-mass energies of $\sqrt{s_{\text{NN}}} = 8.8\,\text{TeV}$ for Pb–Pb and $\sqrt{s_{\text{NN}}} = 5.5\,\text{TeV}$ for p–Pb collisions in Run 3 [1]. The collider features four interaction points where the two counter-rotating beams intersect. At each of these locations, one of the four major experiments, ATLAS, CMS, LHCb, and ALICE is installed [2].

The ALICE detector is a general-purpose apparatus optimized for investigating QCD matter at extreme energy densities, particularly the formation and properties of the QGP in heavy-ion collisions[1]. A schematic representation of the current ALICE detector layout is shown in Fig. 2.1. In its present configuration, charged-particle trajectories and primary interaction vertices are reconstructed by the **I**nner **T**racking **S**ystem (ITS) and the **T**ime **P**rojection **C**hamber (TPC), which together provide the principal tracking capabilities and momentum determination. Particle identification and tracking are further enhanced by the **T**ransition **R**adiation **D**etector (TRD) dedicated to electron identification and by the **T**ime **O**f **F**light (TOF) for precision timing measurements [1]. These subsystems are complemented by

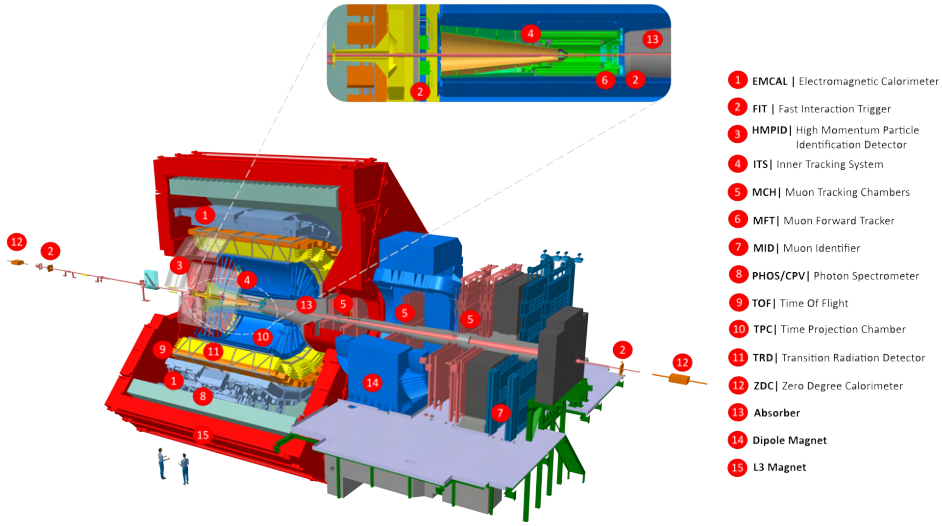


Figure 2.1.: Schematic view of the current ALICE detector systems, adapted from [1].

several calorimeters, such as the **E**lectro**M**agnetic **Cal**orimeter (EMCal), and by dedicated muon-identification systems including the **H**igh **M**omentum **P**article **I**dentification **D**etector (HMPID). The central barrel is operated inside a solenoidal magnetic field created by a non-superconducting solenoid with $B = 0.5\,\mathrm{T}$. In addition, the detector contains a forward muon arm, which employs a non-superconducting dipole magnet, absorbers and multiple tracking detectors[1].

2.1.1. Semiconductor Tracking Detectors

Beyond reconstructing particle trajectories (tracking) to study the trajectories themselves, a central challenge in HEP is separating primary and secondary vertices (vertexing). To reliably differentiate between primary and secondary vertices, a high sensor granularity is required in order to identify individual trajectories and reconstruct them with sufficient precision. A high precision in track reconstruction results in greater precision of vertex reconstruction, which allows disentanglement of the vertices if precise enough. A schematic representation of a measurement with a pixel detector of particles produced at a primary and a secondary vertex is shown in Fig. 2.2. The particle trajectories are reconstructed from the discrete measurement points recorded along their paths. Typical examples of measure-

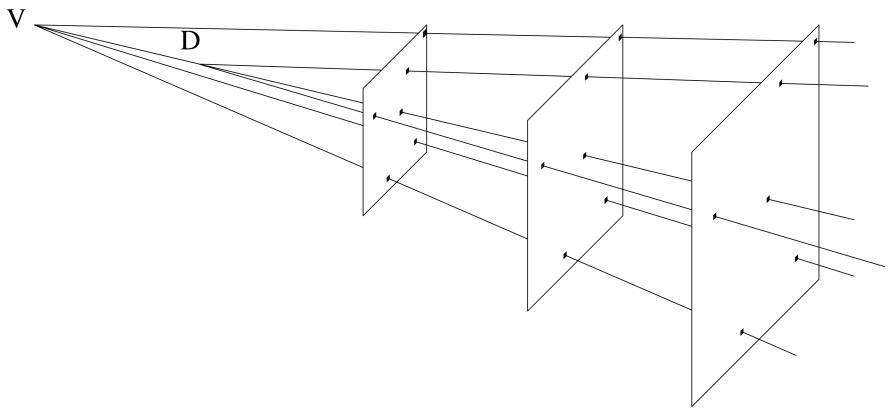


Figure 2.2.: Schematic of a short-lived particle decay with the collision vertex V and the decay vertex D. Each rectangle resembles a pixel detector layer with the respective point of measurement. Taken from [3]

ments that require precise vertexing included the measurement of the very short-lived τ lepton, for which the distance between the interaction point (primary vertex) and the decay point (secondary vertex) amounts to only a few millimeters [4], while in the study of heavy-flavor decays, candidates like the Λ_c with a mean proper decay length of 60 µm [5] require even higher precisions in modern detectors.
The precision of vertex reconstruction can be expressed via the uncertainty on the impact parameter, which is defined as the distance of closest approach of the reconstructed trajectory to the interaction point in the transverse plane. For a simplified configuration with two one-dimensional detector layers, this uncertainty can be approximated by

$$\sigma_b^2 = \left(\frac{r_1}{r_2 - r_1}\,\sigma_{spa,2}\right)^2 + \left(\frac{r_2}{r_2 - r_1}\,\sigma_{spa,1}\right)^2 + \sigma_{\mathrm{ms}}^2,$$

where r_1 and r_2 denote the distances of the two sensors from the vertex, with r_1 denoting distance of the sensor closest to the vertex [4]. $\sigma_{spa,1}$ and $\sigma_{spa,2}$ are the spatial resolutions of the respective sensors. The term σ_{ms} represents an additional contribution dominated by multiple Coulomb scattering of the particle in the first detector layer (and the beam pipe) [4]. This contribution is determined primarily by the material budget x/X_0, which will be discussed in more detail in Sec. 3.1.1.

From this relation, it follows that the lever arm between r_1 and r_2 should be maximized, while at the same time the distance between the vertex and the first detector layer r_1 should be minimized. In addition, the traversed material budget should be as small as possible [4].

Owing to their high granularity (small σ_{spa}) and the low material budgets x/X_0 that can be

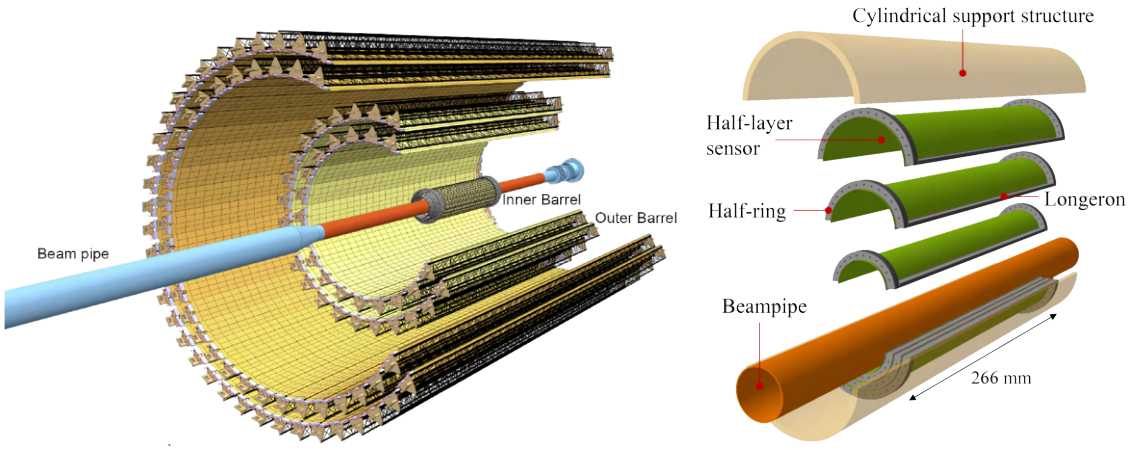


Figure 2.3.: Schematics of the ITS2 (1), taken from [7] and the ITS3 detectors (2), taken from [6]

achieved, silicon pixel sensors are increasingly coming into focus as the technology matures, as exemplified by the recent ITS3 project.

2.1.2. ITS3

As described above, the **I**nner **T**racking **S**ystem (ITS) is a major contributor to the ALICE tracking performance, which is crucial for the reconstruction of tracks to the primary vertex [1]. To further enhance the tracking and vertexing performance, the three innermost layers will be upgraded within the LS2 of the LHC [6], which is scheduled from 2026-2029 in the ALICE **I**nner **T**racking **S**ystem **3** (ITS3)-project.
The current version (ITS2) consists of seven layers containing 24000 of so-called ALPIDE **M**onolithic **A**ctive **P**ixel **S**ensors (MAPS) sensors with a pixel size of 29 µm × 27 µm. A schematic can be found in Fig. 2.3(left). The sensors are mounted on staves and arranged in a cylindrical configuration around the interaction point. The three innermost layers have a material budget of 0.36 % X_0/layer and the innermost layer has a radius of r_1=22 mm around the interaction point [7] with nine ALPIDE units on each stave. It features a positional resolution of about 5 µm.

The objective of the ITS3 project is to replace all layers of the innermost barrel with two wafer-scale bend half-barrels. A schematic is shown in Fig. 2.3(right). This is enabled by moving from the initially used 180 nm process to 65 nm technology for production, which allows a larger wafer size as well as higher circuitry density [6]. Another factor is the usage of the stitching process, which allows wafer-sized production of sensors, as it extends the

usual limit of the mask size in photo-lithographic production by implementing a higher-level connection. The application of which is a novelty in HEP[1]. Further, the sensor is thinned to a thickness of about 50 µm to allow cylindrical bending of the waver-scale sensor [8]. Effectively, the project aims to reduce the material budget to 0.07 % X_0/layer via multiple factors that are achieved by the novel approach. The major contributors are the reduced power consumption of the sensors, which eliminates the need for water cooling, as well as the removal of the staves and the FPC [6], which were required in the ITS2 for support and power supply and readout. These will be implemented by moving the power supply and readout structures to the sides, where they are connected using so-called endcaps. Together with a reduced radius, with an innermost layer radius of 18 mm, this would allow a doubling of the impact parameter resolution up to a transverse momentum p_T of about 5 GeV/c [6]. Within the development phase, multiple test structures and prototype sensors such as the **A**nalog **P**ixel **T**est **S**tructure (APTS), the **D**igital **P**ixel **T**est **S**tructure (DPTS), as well as the **Mo**nolithic **S**titched **S**ensor (MOSS) and babyMOSS have been developed and tested within multiple characterization campaigns to develop the final sensor (for further reading see [6]). The latter will be used in this thesis and discussed in more detail in Ch. 4.

[1] At the point of publication of the ITS3 **T**echnical **D**esign **R**eport (TDR) [6]

3. Fundamentals of Semiconductor Pixel Detectors

Semiconductor pixel detectors are playing an increasingly central role in experimental particle physics as technological limitations are reduced and fabrication costs continue to decrease. This chapter is devoted to the fundamental principles of silicon pixel detectors and their realization as **M**onolithic **A**ctive **P**ixel **S**ensorss (MAPSs)(see Sec. 3.3.3). The subsequent chapter will introduce the essential concepts governing the interaction of charged particles with matter (see Sec. 3.1) and the basic operating principles of semiconductor detectors (see Sec. 3.2). Building upon these foundations, it will then address semiconductor particle detectors capable of providing spatial information on traversing particles (see Sec. 3.3), thereby enabling their deployment in high-precision particle tracking systems.

3.1. Interactions of Particles with Matter

The detection of a particle fundamentally relies on quantifying the energy it deposits while traversing the sensor medium. Although a variety of detector concepts exist, a large class of detection mechanisms, including semiconductor detectors, is based on the measurement of energy loss arising from ionization processes within the detector material.

In the following, the fundamental principles governing the interaction of charged particles with matter will be discussed. This section covers both the energy loss experienced by a particle as it propagates through successive material layers and the associated change of its trajectory. At this point, it should be noted that the described sensors allow the detection of photons as well. However, as this is not relevant to the subject of this thesis (see Ch. 5), it will not be discussed any further (for further reading see, for example [9]).

3.1.1. Energy Loss of Charged Particles

When traversing a detector, particles that carry electric charge and have a nonzero rest mass deposit a portion of their kinetic energy through interactions with the detector medium.

The magnitude of this energy loss, and thus the deposited energy, is determined by the physical properties of the detector material and by the kinematic and characteristics of the incident particles[4].

The Bethe-Bloch Equation

The mean specific energy loss, denoted by $\langle dE/dx \rangle$, is used to quantify the average energy loss of a charged particle traversing a material [4]. This quantity characterizes the energy loss dE of the particle per unit path length dx in a given medium. In the energy range relevant to the present work, the mean specific energy loss is commonly approximated by the Bethe–Bloch formula, which describes the ionization energy loss arising from Rutherford scattering of the incident particles on bound (shell) electrons of the medium. It is given by

$$-\left\langle \frac{dE}{dx} \right\rangle = K \frac{Z}{A} \frac{z^2}{\beta^2} \left[\frac{1}{2} \ln \left(\frac{2 m_e c^2 \beta^2 \gamma^2 W_{\max}}{I^2} \right) - \beta^2 - \frac{\delta(\beta\gamma)}{2} \right] \tag{3.1}$$

[10]. Here, $K = 4\pi N_A r_e^2 m_e c^2 \approx 0.307\,\mathrm{MeV\,cm^2/g}$, where $r_e = e^2/(4\pi\epsilon_0 m_e c^2) \approx 2.8\,\mathrm{fm}$ is the classical electron radius, z is the charge number of the incident particle, and Z and A denote the atomic number and mass number of the absorber material, respectively[4]. The quantities β and γ are the usual relativistic factors, $\beta = v/c$ and $\gamma = 1/\sqrt{1-\beta^2}$, and m_e is the electron mass. Furthermore, $W_{\max}$ is the maximum kinetic energy transferable to a free electron in a single collision, I is the mean excitation potential of the medium, and $\delta(\beta\gamma)$ is the density-effect correction term that becomes relevant at higher energies [4].

The Bethe–Bloch expression in the form of Eq. (3.1) is valid for momenta corresponding to $0.1 \lesssim \beta\gamma \lesssim 1000$ [10] and for heavy charged particles. An important exception is the case of electrons and positrons, for which additional contributions from $e^- e^-$ and $e^+ e^-$ interactions must be taken into account [4].

The characteristic dependence of the mean specific energy loss rate, as described for example by Eq. (3.1), is illustrated in Fig. 3.1 for various particles and absorber materials. The energy loss first decreases with increasing momentum until it reaches a minimum at $\beta\gamma \approx 3$–3.5 [4]. Particles with $\beta\gamma$ in this minimum region are referred to as **M**inimal **I**onizing **P**articles (MIPs) [4]. For larger values of $\beta\gamma$, the mean specific energy loss increases again, and for $\beta\gamma \gtrsim 1000$, radiative effects (such as bremsstrahlung, pair production, and photonuclear interactions) become significant and must be taken into consideration[4].

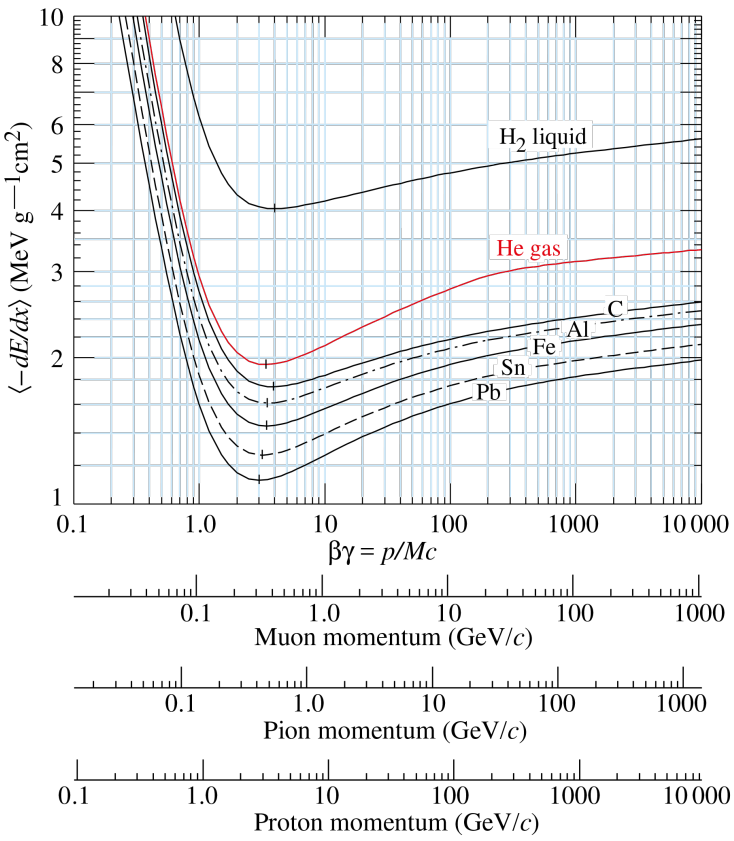


Figure 3.1.: Mean energy-loss rate for different (liquid) materials. Radiative effects are not included. Taken from [10].

Most Probable Energy Loss

Equation (3.1) describes the mean energy loss of a charged particle traversing a given medium. In practice, however, stochastic fluctuations of the energy loss give rise to an asymmetric probability distribution of possible energy deposits. Consequently, the arithmetic mean is shifted toward less probable but comparatively larger energy losses relative to the **M**ost **P**robable **V**alue (MPV) [4]. This affects not only determinations of momentum or mean energy loss, but is also relevant for particle detection, since the detector types considered (See Ch, 4) here require a minimum threshold in the deposited energy in order to register a signal. This can be accounted for either by employing the (approximated) energy-loss distribution for particles of known energy or by imposing a lower cutoff on the distribution at a specified energy threshold [4].

For absorber layers of moderate thickness, the energy-loss distribution can be approximated

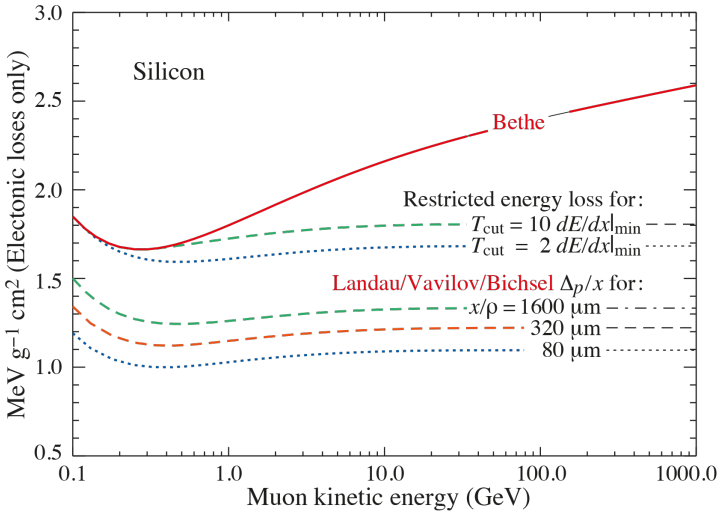


Figure 3.2.: From top to bottom: (1) Specific mean (electronic) energy loss of muons in silicon according to the Bethe–Bloch formula. (2) & (3) Mean (electronic) energy loss for truncated energy-loss distributions, where a lower cut is applied at the specified value per collision ($dE/dx|_{min} = 1.664\,\mathrm{MeV\,cm^2/g}$ [10]). (4)–(6) Most probable (electronic) energy loss per unit path length according to the Landau–Vavilov distribution for different layer thicknesses. Taken from [10].

by a scaled and shifted Landau distribution, commonly referred to as the Landau–Vavilov distribution. From this, an expression for the most probable value (MPV) of the energy loss can be derived as

$$\Delta_p = \xi \left[\ln\left(\frac{2m_e c^2 \beta^2 \gamma^2}{I}\right) + \ln\left(\frac{\xi}{I}\right) + j - \beta^2 - \delta(\beta\gamma) \right], \quad \xi = \frac{1}{2} K \frac{Z}{A} \frac{z^2}{\beta^2} \Delta x \tag{3.2}$$

where Δx denotes the path length of the particle in the medium and $j = 0.2$ [10]. Although the Landau–Vavilov distribution itself does not accurately describe very thin silicon layers, Eq. (3.2) remains valid, as the most probable energy loss is still reproduced with good accuracy [10]. The difference between the mean energy loss and the most probable energy loss for muons traversing silicon layers is illustrated in Fig. 3.2. As shown there, this difference is substantial and increases as the silicon layer thickness decreases. This clarification is therefore relevant to thin silicon detector layers, like for example the planned ITS3, that is expected to have a per-layer thickness of 50 µm [8].

Multiple Scattering

In addition to energy loss, the interaction of charged particles with matter leads to a modification of their initial trajectories. These deflections, which constitute a crucial obstacle in particle track reconstruction, are discussed in the following.

As a consequence of Rutherford scattering on the constituents of a material, charged particles experience angular deviations of their trajectories while traversing matter. The dominant contribution to this process originates from Coulomb interactions between the incident particle and the atomic nuclei of the medium. The probability that a particle is scattered to a given angle in a single interaction is described by the Rutherford differential cross section[4].

If the number of scattering interactions within a given material layer exceeds approximately 20, the cumulative effect of these numerous small-angle deflections can be treated within the framework of Molière's theory of multiple Coulomb scattering[4]. In this regime, the angular distribution of the projected scattering angle after a finite number of interactions, denoted by θ_{plane}, can be approximated by a Gaussian distribution,

$$f(\theta_{\text{plane}})\, d\theta_{\text{plane}} = \frac{1}{\sqrt{2\pi}\,\theta_0} \exp\left(-\frac{\theta_{\text{plane}}^2}{2\theta_0^2} \right) d\theta_{\text{plane}}, \tag{3.3}$$

where θ_0 represents the standard deviation of the distribution [4]. The quantity θ_0 can be estimated using the Highland formula,

$$\theta_0 = \frac{13.6\,\text{MeV}}{p\,\beta}\, z \sqrt{\frac{x}{X_0}} \left(1 + 0.038 \ln \frac{x}{X_0} \right), \tag{3.4}$$

where p is the particle momentum, β is the particle's velocity in units of the speed of light, and x is the thickness of the scattering medium. The parameter X_0 denotes the radiation length of the material, defined as the mean distance over which an electron loses a fraction $1 - \frac{1}{e}$ of its initial energy [4]. Considering the full three-dimensional problem, the standard deviation of the spatial scattering angle with respect to $\theta = 0$ is then given by [4]

$$\sqrt{\langle \theta^2 \rangle} = \sqrt{2}\theta_0. \tag{3.5}$$

3.2. Semiconductor Particle Detectors

Following the discussion of the mechanisms by which charged particles deposit energy in matter, this section addresses how the corresponding energy loss after a particle interaction

can be converted into a measurable signal in semiconductor materials. After a brief description of semiconductor properties, including doping and the formation of the p-n junction, the use of these structures as detector systems will be introduced.

Semiconductors and Doping

The conductive properties of solid-state materials are predominantly determined by the upper energy levels of their constituent atoms. In crystalline solids, such as those forming a periodic lattice, the overlapping atomic energy levels give rise to continuous energy bands. Based on the size of the energy gap (band gap) between the two highest energy bands, materials can be classified into three categories: insulators, semiconductors, and conductors.

In insulators, the electrons are strongly bound in the lower valence band, resulting in a large band gap to the higher-lying conduction band, typically in the order of $E_G \sim 9\,\mathrm{eV}$[4]. Consequently, thermal excitation at room temperature is insufficient to promote a significant number of electrons into the conduction band, and electrical conductivity is very low. In contrast to this, the valence band and conduction band of conductors either overlap or the valence band is only partially filled. In such materials, charge carriers can move freely, leading to high electrical conductivity.

Semiconductors occupy an intermediate position between these two categories. The bond strength between neighboring atoms is weaker than in insulators, and the resulting band gap is typically of the order $E_G \sim 1\,\mathrm{eV}$[4]. In this case, transitions of electrons from the valence band to the conduction band can be induced by thermal excitations or by external electromagnetic fields [4]. The most commonly used material in semiconductor detector technology is silicon. Silicon has a band gap of 1.12 eV [11] and belongs to group IV of the periodic table. In its crystalline form, each silicon atom forms covalent bonds with four nearest neighbors in a tetrahedral configuration.

The electronic properties of a semiconductor crystal can be tailored by the intentional introduction of impurities into the crystal lattice, a process known as doping. In doped semiconductors, the number of valence electrons of the dopant atoms differs from that of the host lattice atoms, which modifies the carrier concentration and, consequently, the conductivity [4].

Two principal types of doping can be distinguished: p-type and n-type doping [4]. In p-type doping, dopant atoms possess fewer valence electrons than the host atoms. For silicon, a typical p-type dopant is boron, which belongs to group III of the periodic table. When boron is incorporated into the silicon lattice, it substitutes a silicon atom but provides only three valence electrons for bonding instead of four. This leads to the formation of an acceptor

level and introduces a weakly bound hole into the lattice, which can act as a mobile positive charge carrier.

In n-type doping, dopant atoms have more valence electrons than the host atoms. In the case of a silicon semiconductor, phosphorus, a group V element, is commonly used. A phosphorus atom substituting for a silicon atom contributes an additional valence electron, which is only weakly bound and can be thermally excited into the conduction band. Therefore phosphorus acts as a donor, increasing the concentration of free electrons, which serve as the dominant charge carriers in n-type silicon [4].

The pn-Junction

A pn-junction is formed by bringing a p-doped and an n-doped semiconductor into contact. In isolation, the Fermi level E_F lies close to the conduction band edge E_L in n-type material and near the valence band edge E_V in p-type material. Upon establishing contact, the difference in the initial Fermi levels drives a thermally induced diffusion of majority charge carriers across the junction [11] (see Fig. 3.3)(1). Electrons diffuse from the n-doped region into the p-doped region, while holes diffuse in the opposite direction, leading to recombination of electrons and holes in the vicinity of the interface between the p- and n-doped regions [4].

After recombination, only the ionized donor and acceptor atoms remain, so that the material in the interface region is no longer electrically neutral. A surplus of negatively charged, ionized acceptors develops on the p-doped side, and a corresponding excess of positively charged, ionized donors appears on the n-doped side. The resulting space charge region gives rise to an internal electrostatic potential difference across the interface. This built-up electric field induces a drift current of charge carriers in a direction opposite to that of the diffusive current of the majority carriers. The drift current increases as diffusion and recombination proceed, until an equilibrium state is reached in which the drift and diffusion currents exactly compensate each other [4].

The region in which free charge carriers have been depleted by recombination, and which is therefore dominated by the fixed charges of the ionized dopants, is referred to as the depletion zone (or depletion region). In thermal equilibrium, a finite potential difference across this region remains, known as the built-in voltage U_{bi}.[1]

The application of an external voltage to the pn-junction modifies the properties of the depletion region by altering the motion of charge carriers. An external voltage U_{ext}, often denoted as back bias when applied with the same polarity as the built-in voltage U_{bi},

[1] In silicon, the built-in voltage is typically $U_{\mathrm{Bi,Si}} \approx 0.6\,\mathrm{V}$ [4].

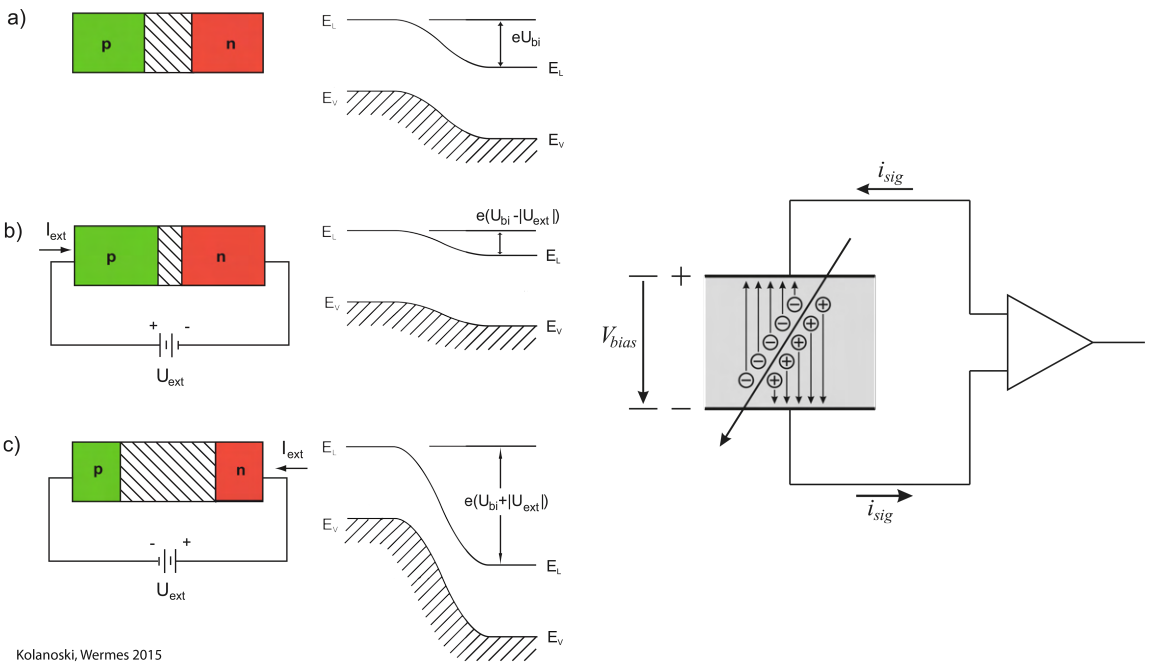


Figure 3.3.: (1) Schematic representation of a pn-junction and the corresponding band structure with and without an applied external voltage U_{ext} [4]. (2) Schematic of an ionization chamber, e.g. a semiconductor detector, showing the induced signal current i_{sig} and the applied bias voltage V_{bias} [11].

increases the total potential difference across the depletion zone. This enhanced potential suppresses carrier diffusion across the junction and leads to a widening of the depletion region [4].

Conversely, when U_{ext} is applied with polarity opposite to U_{bi} (forward bias), the effective potential barrier is reduced. The corresponding decrease in the electric field strength lowers the drift component opposing diffusion, thereby facilitating carrier injection across the junction. As a consequence, the width of the depletion zone decreases under forward-bias conditions [4].

Signal Formation

The operating principle of semiconductor detectors is that of an ionization chamber [3]. As described in Section 3.1, particles deposit energy when crossing a material. In a semiconductor, a part of this energy will create electron-hole pairs. In a 300 µm silicon layer for example a MIP has a mean energy loss of $\frac{dE}{dx}$ 117 keV/300 µm with a MPV of 84 keV/300 µm[4]. Under the assumption of 3.65 eV required energy loss per electron hole pair in silicon at 300 K[4], this will lead to a mean of 32000 generated hole pairs with a MPV of 23000 [4]. If

this process occurs in a sufficiently strong electric field, the charge carriers will be separated. The movement of the charge carriers will then induce an electrical signal when moving to the poles. This electrical signal can then be measured with electrodes on the sides of the detector [4] as can be seen in Fig. 3.3.

3.3. Semiconductor Pixel Detector

For most applications in particle physics, a positional detection of the particle is required. With semiconductor particle detectors, this is achieved by structuring the detector. The following section will focus on pixel-structured detectors and different implementations of these systems.

3.3.1. Position Measurement by Segmentation

Spatial information is obtained by segmenting the detector into multiple semi-independent elements. A schematic can be seen in Fig. 3.4 (1).

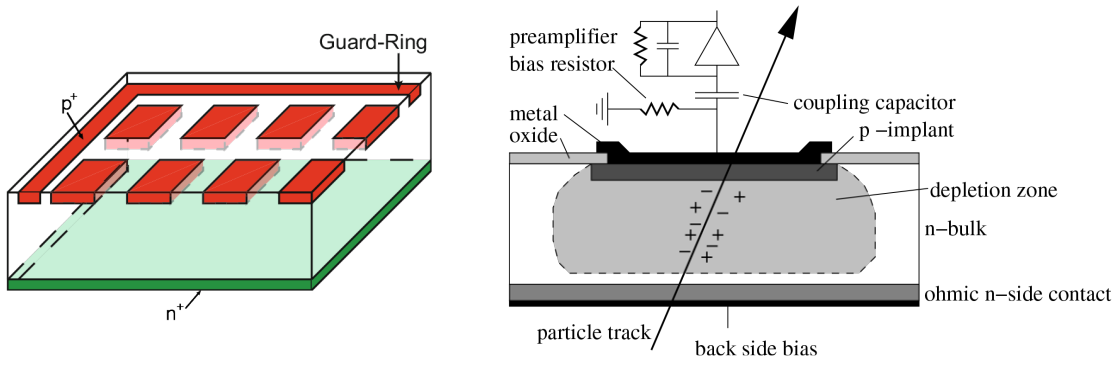


Figure 3.4.: Schematic of a segmented semiconductor pad, i.e., pixel detector in total (1) (modified from [4]) and in cross-section of a single pad (2) [3].

The material is strongly n-doped (n^+) at the bottom, followed by a comparably thick, less heavily n-doped (n^-) regime (n-bulk). To receive spatial information, the surface is not completely p-doped (p^+) but segmented into smaller elements in both surface directions. These segments are called pads or, if the length of one edge falls into the range of some 100μm or lower, pixels[4]. Figure 3.4 shows a schematic cross-section of a single pad. A depletion zone will form between the n-bulk and the p-implant. If an ionizing particle crosses the sensor, the generated charge will form an electronic signal on the corresponding electrodes. This signal can then be captured and processed by a connected circuit. Assigning the electrodes to a specific area of the detector will then allow to locate the generated charge

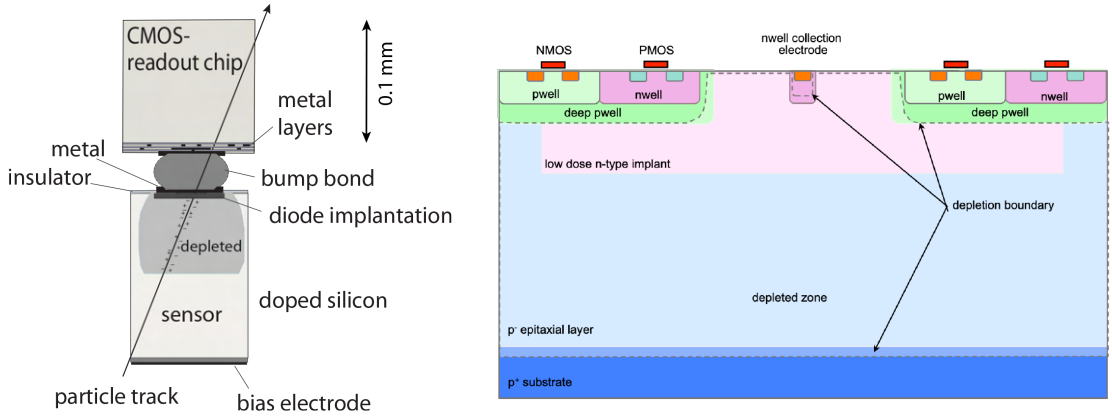


Figure 3.5.: Cross-section of a single pixel design that was the basis of the MAPS babyMOSS sensor[6] (1) and cross-section of a single sensor and readout cell of a hybrid pixel sensor. [9]

at the level of individual pads or pixels. The emerging spatial resolution can be enhanced by the effect of charge sharing in which a signal is not only obtained from the primary pad or pixel but from the next neighbor relative to the intersection point of the incident particle [3]. This will be further discussed in Section 6.2.5.1.

3.3.2. Hybrid Pixel Detectors

For the production of hybrid pixel detectors, the sensor diode and the readout are produced as two separate components. A schematic can be found in Fig.3.5(1). Both components will share the same geometrical grid structure to allow electrical connection of both components in the final production step. This so-called bonding can be performed in multiple ways. Fig.3.5 shows a schematic example where the readout structure and sensor are connected via a bump contact that closes the electrical contact. This separated approach offers many advantages. Firstly, the variety of sensitive materials that can be used is broadened compared to the later presented MAPS approach, as the silicon-based **C**omplementary **M**etal-**O**xide-**S**emiconductor (CMOS) readout works independently [3]. This broadens the adjustability of the sensors to the respective use case. Also, both structures can be designed independently of each other, which reduces the need to take the other component into account in the development of the components. This also allows reuse of a well-designed readout structure on a new sensor design [4], which lowers production costs by avoiding the redesign of the readout.

However, there are some downsides that come with this technology. For example, the bond-

ing process is rather complex, which entails higher production costs. Also, the production process results in an increased thickness (in comparison to MAPS), which increases multiple scattering (see Sec. 3.1.1) in the detector, which complicates track reconstruction.

3.3.3. Monolithic Active Pixel Sensors (MAPS)

In **M**onolithic **A**ctive **P**ixel **S**ensorss (MAPSs), the readout structure and the sensor diode are unified in one monolithic unit. While the segmented structure remains, the CMOS readout is placed on the epitaxial layer. A fundamental scheme used in the ITS3 project is shown in Fig. 3.5(2). The p^- doped epitaxial layer is placed on the p^+ doped substrate. The depletion zone builds between the low-dose n-type implant in which the collection electrode sits and the substrate. As the CMOS structures would compete with the charge collection process, they are shielded by a deep p-well (a p-doped regime). Due to the widespread use of the fundamental production process, as well as the elimination of the need for more complex bonding processes, the initial costs for sensor production fall. Together with the possibility of a reduced thickness in comparison to hybrid pixel sensors [4], the technology becomes a promising candidate in larger particle tracking detectors.

4. The babyMOSS Sensor

The sensor used in this work is the so-called babyMOSS, one of the MAPS prototypes developed within the ALICE **I**nner **T**racking **S**ystem **3** (ITS3) project. This chapter first introduces the sensor and its peripheral readout system (Sec. 4.1). It then describes the fake-hit-rate and threshold measurements used to characterize a sensor and to determine suitable operating points (see Sec. 4.2).

4.1. The MOSS and the babyMOSS

This section begins by introducing the babyMOSS (Sec. 4.1.2), starting with the stitched **Mo**nolithic **S**titched **S**ensor (MOSS) device from which it is derived (Sec. 4.1.1). It then describes the in-pixel front-end (Sec. 4.1.3), readout scheme (Sec. 4.1.4), and test system (Sec. 4.1.5).

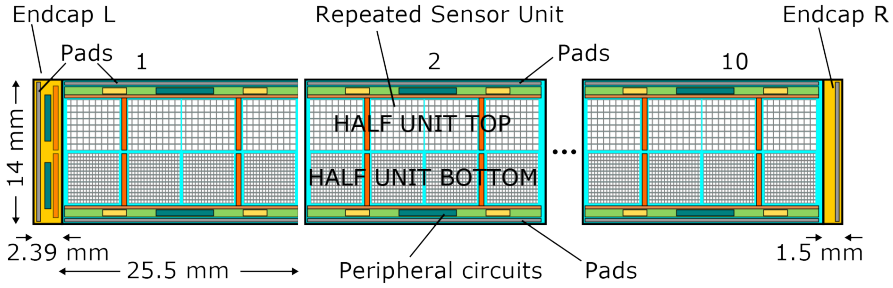


Figure 4.1.: Schematic of the MOSS consisting of ten RSUs, each divided into a top half and bottom half unit [6].

4.1.1. The Monolithic Stitched Sensor (MOSS)

Within the context of the ITS3 project, several MAPS prototypes have been developed to evaluate and refine various elements of the sensor system. Among these is the MOSS, conceived specifically to further investigate the possibility of employing stitching technology

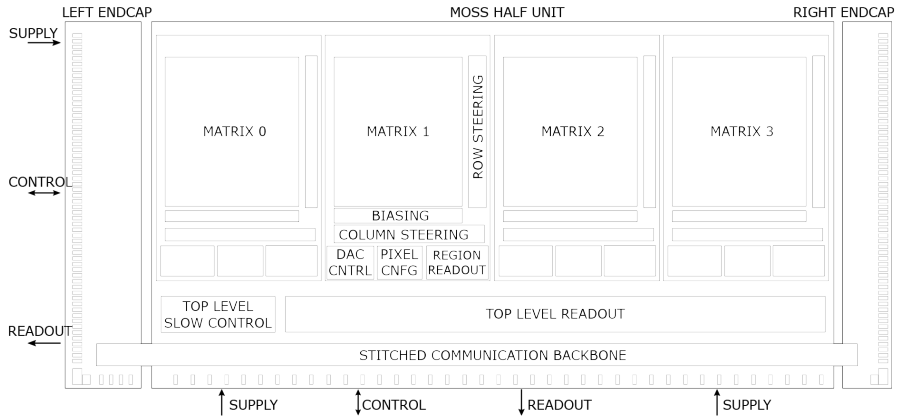


Figure 4.2.: Block diagram illustrating a single RSU of the MOSS, i.e. babyMOSS, including supply readout and control.[6]

in the ITS3. Stitching allows the photo-lithographic manufacturing of structures that exceed the size of the usual design reticle of 3 by 2 cm [6] defined by the photomask. Stitching applies a higher-level interconnection to connect the separated units of the given size to allow building larger structures. The MOSS comprises ten stitched **R**epeated **S**ensor **U**nits (RSUs), which are enclosed by an endcap on each side (Fig. 4.1). Every RSU is subdivided into two half units, which constitute independent sensor units with distinct characteristics. The stitched communication backbone (Fig. 4.2) enables control and readout exclusively from the left endcap and is supported by connectors on each individual half unit [6].

4.1.2. The babyMOSS

Due to the high modularity of the design, the RSUs can be deployed not only in a stitched configuration but also as a standalone device referred to as babyMOSS. Because of its smaller size, this sensor simplifies the implementation into test and characterization setups. In accordance with the architecture of a single RSU, the babyMOSS contains two **H**alf **U**nits (HUs). The so-called **T**op half unit (tb) hosts four 256 $\times$ 256 pixel matrices, also called regions, with a pixel pitch of 22.5 µm. The **B**ottom half unit (bb) is designed in a more compact form, featuring four higher-density matrices with 320 $\times$ 320 pixels and a pixel pitch of 18 µm. As illustrated in Fig. 4.2, each half unit is equipped with its own analog biasing block and a dedicated region readout structure [6]. Furthermore, every half unit contains a top-level readout and a top-level peripheral control system, and can be powered and controlled either exclusively from the left endcap, exclusively via the pads along the long edge, or in a hybrid configuration employing both interfaces.

4.1.3. The In-Pixel Front-End

The front-end of each pixel contains an analog part and a digital part. The digital regime controls the masking of the pixel and the pulsing, which allows to inject charge into the collection diode for characterizing the sensor at different settings [12, 13]. In the analog front-end, the obtained voltage signal is processed by multiple stages, amplifying and discriminating the signal whilst also recharging the collection diode after an event. A simplified version of the analog pixel front-end of the babyMOSS is shown in Figure 4.3.

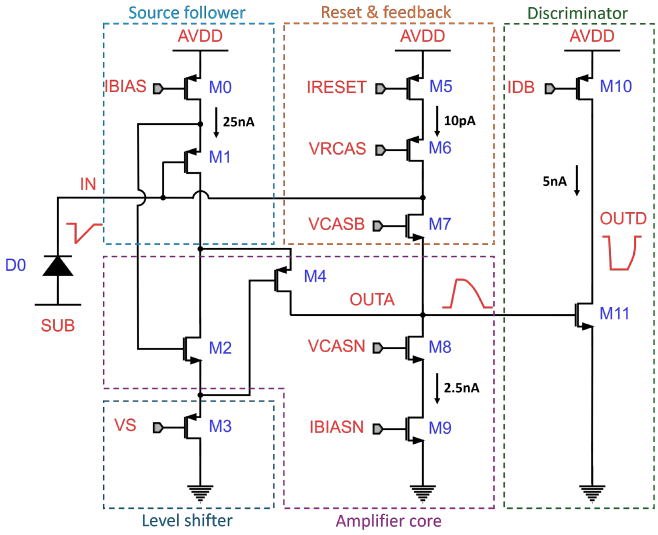


Figure 4.3.: Simplified version of the in-pixel front-end of the babyMOSS sensor. Taken from [13]

As described in Ch. 3, electron-hole pairs are created within the sensor when a charged particle deposits energy in the active area. Due to the electric field in the depletion zone, these charges are moving towards their closest collection diode D0, which is directly coupled to the gate of the input transistor M1 itself, which is set up in a source follower configuration to reduce the impact of its gate-source capacitance [13]. It is biased by the major biasing current I_{BIAS} controlled by M0 (IBIAS). The source of M1 is connected to the gate of M2, which is acting as a common source amplifier. This stage effectively acts as an inverting amplifier, which is expanded into a cascode-like topology using the transistor M4 and the bias current I_{BIASN}, which is provided by M8 (VCASN) and M9 (IBIASN) [13]. Additionally, a level shifter is implemented by the transistor M3 (VS/VSHIFT), shifting the source voltage of M2, which broadens the operational margin of the sensor. The so far described stage is acting as a two-stage amplification inverting stage. The amplification of this system is controlled by the parameters IBIASN, VCASN, IBIASN and VSHIFT, controlling the baseline as well as the biasing currents I_{BIAS} and I_{BIASN}.
The amplified signal is then digitized by a discriminator stage that is set up by the transistors M10 (IDB) and M11, efficiently acting as a current comparator. M10 (IDB) is providing a current I_{DB} higher than the standby current of M11 [14]. The high I_{DB} results in a high OUTD in the standby state. An incoming signal will then lead to an increase of current

in M11 until it exceeds I_{DB}, which will lead to a discharge of OUTD to the ground. The threshold of this discrimination stage can therefore be steered by the setting of I_{DB}.
As mentioned above, the collection diode is recharged after an event. The reset current I_{RESET} is set up by the transistors M5 (IRESET) and M6 (VRCAS). The recharge process is regulated by the feedback transistor M7 (VCASB), which also sets the working point of the input node. M7 passes the I_{RESET} current into the collection diode due to its falling gate to source voltage after an event. This leads to a recharge of the collection diode. Together, the reset current IRESET and the feedback transistor VCASB are setting the output baseline of the amplification stage [13]. It can be concluded that the overall charge threshold of the front-end is shaped by the tuning of the amplification gain (IBIASN, VSHIFT, VCASN, IBIASN), the amplification output baseline (IRESET, VRCAS, VCASB) and by the threshold of the discriminator (IDB). For the purpose of sensor optimization, the implementation of the front-end varies from region to region. A table with the variations can be found in the appendix Tab. A.1.
Lastly, the parameter V_{psub}, which is applied to the sensor externally, is to be mentioned. It denotes the back-bias voltage applied to the sensors and substantially decreases the effective threshold. As the parameters of the front-end do not work independently, the application of a typical V_{psub}=−1.2 V requires the adjustment of the remaining parameters as well, indicating, for example, the requirement of a higher setting of VCASB.

4.1.4. Readout Cycle

Definition 1. *Hit: A logically high return of the pixel front-end.*

During the readout procedure, each pixel will return a binary hit information, i.e., whether a signal has surpassed the threshold or not. The babyMOSS requires a trigger signal in order to access this hit information. A schematic timeline of the readout sequence is shown in Fig. 4.4. The babyMOSS receives a trigger from an external source, such as a scintillator-based trigger system (which will be described in Sec. 5.1.1). In this exam-

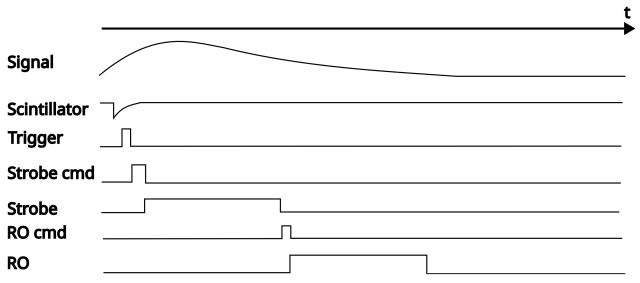


Figure 4.4.: Schematic timeline of a readout process of the babyMOSS (not to scale). Taken from [15] with kind permission of Alexander Rachev.

ple, a charged particle traverses the setup and generates a signal in a scintillator detector. This signal causes the trigger logic board to issue a trigger signal, which is then forwarded to the babyMOSS. Upon receiving this trigger, the chip sends a strobe command (*Strobe cmd*) to each pixel. During the resulting strobe window (*Strobe*), whose duration can be adjusted, the digital hit state of each pixel that coincides with the strobe pulse is captured and stored in a latch [12]. Once this interval has ended, a readout command (*RO cmd*) is issued and the stored hit information is subsequently retrieved from the latch (*RO*).

4.1.5. The babyMOSS Test System

To operate a babyMOSS, a three-component setup is used, as can be seen in Figure 4.5. The system is managed by the **D**ata **Ac****Q**uisition board (DAQ board), which is controlled from a PC via a USB-A interface. The DAQ board provides connectors for the power supply and *LEMO* interfaces for receiving external trigger signals (*TRG IN*), the sending of busy signals (*BSY OUT*) that indicate an ongoing readout cycle, and for applying the back-bias voltage V_{PSUB}. If no back-bias voltage is used, the connector is shorted with a $0\,\Omega$ shunt (as shown in Fig. 4.5). For synchronized operation of several detector layers, the DAQ board is equipped with a TRG OUT port that forwards the TRG IN signal and a BSY IN port. When the chip itself is not executing a readout cycle, the DAQ board passes

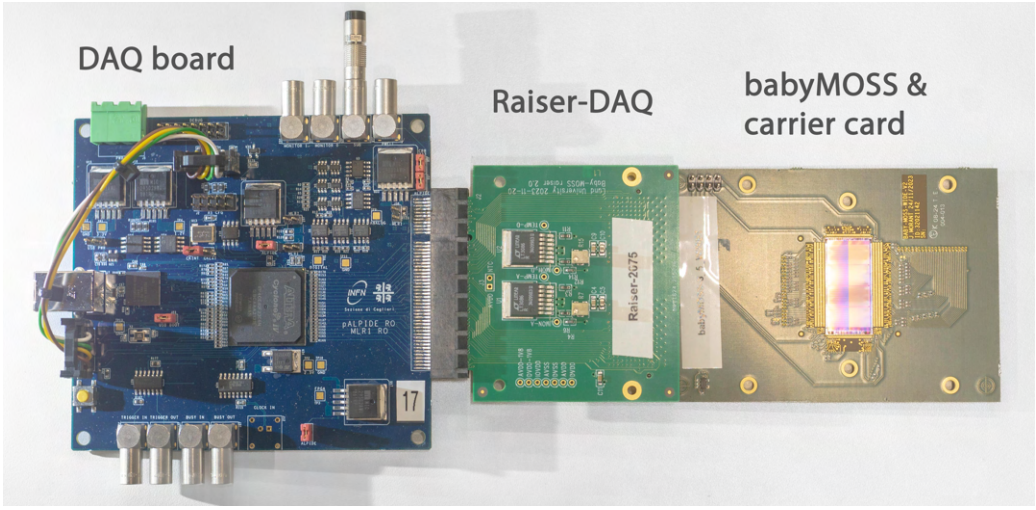


Figure 4.5.: Photograph of the babyMOSS test system

the signal from the BSY IN port through to the BSY OUT port.

The DAQ board was originally developed for the ALPIDE sensor; therefore, operating a

babyMOSS sensor required rerouting specific data lines and adjusting the control of the supply voltages. This functionality is provided by the Raiser-DAQ, which acts as the interface between the DAQ board and the carrier card.
The Raiser-DAQ and the carrier card are linked via a 560-pin connector. In addition, the Raiser-DAQ can receive the **P**ressure, **T**emperature, and **H**umidity (PTH) sensor signal from the carrier card through a dedicated two-pin connection.
The babyMOSS chip itself is glued to the carrier card, a passive **P**rinted **C**ircuit **B**oard (PCB). Electrical contact between the carrier card and the babyMOSS is established through wire bonds connecting the babyMOSS pads to the corresponding pads on the carrier card (see for instance [15]).

4.2. Characterization Measurements

Two standard measurements are used throughout this work to characterize the babyMOSS and identify operating points and noisy pixels: the **F**ake **H**it **R**ate (FHR) and the **Thr**eshold (THR). Both are described in the following section.

4.2.1. Fake Hit Rate (FHR)-scan

Definition 2. ***F**ake **H**it **R**ate (FHR): The rate of registered hits per pixel in the absence of incident particles and without any pixel pulsing.*

The **F**ake **H**it **R**ate (FHR) of the pixel matrix is determined by performing a large number of readout cycles via the DAQ board while no pulsing is applied. To minimize external perturbations, the sensor is shielded from ambient light and oriented vertically to reduce the sensor area exposed to atmospheric radiation. From these measurements, the FHR is obtained as

$$FHR = \frac{N_{hits}}{N_{triggers} \cdot N_{Pixels}}, \tag{4.1}$$

where N_{hits} denotes the total number of registered hits within the matrix, $N_{triggers}$ the total number of induced readout cycles, and N_{Pixels} the number of pixels contained in the matrix. The statistical uncertainty is estimated assuming a binomial distribution and a confidence level of 68.3%.

In addition to providing an estimate of the FHR, the described measurement allows the identification of noisy pixels by identifying pixels whose individual FHRs exceeds a predefined threshold frequency.

4.2.2. Threshold (THR)-scan

Definition 3. ***Thr**eshold (THR): The threshold of the in-pixel deposited charge required to generate a logically high response at the pixel front-end.*

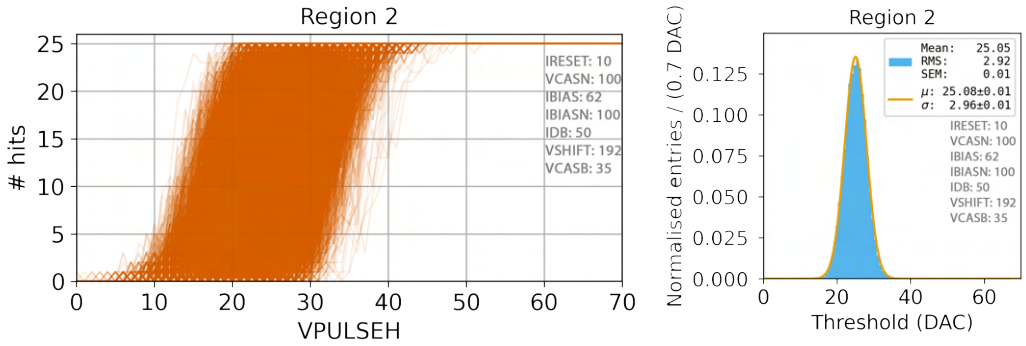


Figure 4.6.: Exemplary results of a babyMOSS region 2 THR-scan. The s-curves of the individual pixels (top) and the resulting threshold distribution (bottom). VPULSEH and the threshold are given in DAC

For the **Thr**eshold (THR) scan, a charge injection is performed on each pixel within a given region to estimate the charge threshold necessary to induce a pixel hit, i.e. to register a positive hit response in that pixel. The injected charge is given by $Q_{inj} = C_{inj} \cdot V_{PULSEH}$ and is varied by stepping V_{PULSEH} from 0 to 70 **D**igital **A**nalog **C**onverter (DAC) steps [8, 16]. For each DAC step, a total of 25 charge pulses is injected into each pixel, and the corresponding number of recorded hits is measured.

Plotting the collected hits for each step against each VPULSEH step results in a so-called S-curve for well-performing pixels. An example S-curve obtained from one of the babyMOSS detectors used in this work is shown in Fig. 4.6. The derivative of the S-curve can be fitted with a Gaussian function (see Fig. 4.6). The mean of this Gaussian fit represents the average threshold of the corresponding region, while the standard deviation provides the **E**quivalent **N**oise **C**harge (ENC), which quantifies the electronic noise associated with the in-pixel front-end and the sensing node [8, 16]. For sensor characterization and for studying the impact of configuration settings and environmental conditions, the average threshold and noise of each region are evaluated (see Fig. 4.6). In addition to determining the noise and threshold distributions, the threshold scan also allows the identification of noisy pixels[1] and bad pixels[2] within a region.

[1] Pixels that fire without injection
[2] Pixels not firing despite injection

5. Beam Telescopes and Local Tracking System

This chapter introduces the two experimental setups used in this work. Both are based on the concept of a beam telescope, a detector arrangement developed for the characterization of silicon detectors. Sec. 5.1 will describe the general operational principle of a beam telescope and its specific implementation as a babyMOSS beam telescope. On this basis, the two setups together with the corresponding particle source used for the measurements are presented: the conventional beam telescope operated during the February 2025 ITS3 testbeam campaign at **EL**ektronen-**S**tretcher-**A**ccelerator (ELSA) (Sec. 5.2.2) and the local tracking system commissioned at the University of Münster for the measurement of atmospheric muons (Sec. 5.3) which was deduced from the initial babyMOSS beam telescope structure.

5.1. Tracking Telescopes & babyMOSS Beam Telescope

The term testbeam describes an experimental phase in detector development in which the sensors are exposed to ionizing radiation created by a particle accelerator for the purpose of (prototype-) sensor characterization. Typically, the measurements are not carried out by a single sensor but by a setup of several sensor planes dedicated to this purpose. This section introduces the measurement principle of a beam telescope and its implementation within the ITS3 project, the babyMOSS beam telescope, including its trigger scheme and the *EUDAQ2*-based data acquisition framework.

5.1.1. Working Principle of a Beam Telescope

In addition to sensor-specific tests, the spatial resolution and the detection efficiency are the two key performance factors that are commonly tested. In silicon detector characterization, the measurements for these parameters are typically carried out via a so-called beam telescope. The typical structure of such a setup can be seen in Fig. 5.1. The setup is

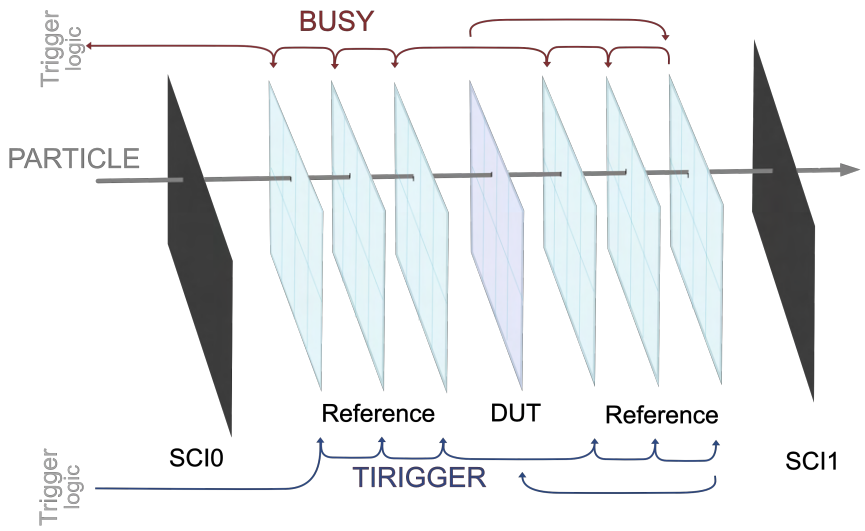


Figure 5.1.: Conceptual sketch of a beam telescope. The scintillator detectors trigger measurements of the enclosed silicon detectors via the trigger logic when a particle traverses. The reference layers allow for reconstructing the particle's point of intersection on the DUT-layer

placed within the particle beam so that the beam axis crosses orthogonally through every sensor. The sensor, which is characterized as the so-called **D**evice **u**nder **T**est (DUT), is set up between a certain number of reference layers which are distributed upstream and downstream[1] around the DUT. The data obtained by the reference layers is then used to reconstruct the particle's trajectory independently of the DUT. As the geometry of the telescope is known, the impact position of the particles on the DUT can be reconstructed from the successful reconstruction of the trajectory. The position of the estimated impact on the DUT can then be used to scan the DUT for hits that can be associated with the estimated trajectory. The information on whether, under certain selected restrictions, a hit can be associated with the calculated trajectory, provides information about the detector efficiency. The resulting residual[2] allows to reconstruct the spatial resolution from the DUT. The details of these calculations will be discussed in Ch.6. Further readings on beam telescopes in general can also be found in the literature on the EUDET telescope (for example [17]) which is a long-standing example of such a setup.

[1] Upstream: Direction that is pointing against the direction of movement of the particles in the laboratory frame. Downstream: Direction that is pointing in the same direction as the direction of movement of the particles in the laboratory frame.

[2] The distance between the reconstructed impact position and the impact position measured by DUT

The babyMOSS beam telescope

The babyMOSS is a triggered sensor (see Ch.4) that requires an external signal for each readout cycle. The primary signal initiating a readout cycle is provided by two scintillator detectors. In the beam telescope configuration under consideration, an external trigger signal is generated by a dedicated ITS3 trigger board. The trigger board is controlled via an **F**ield-**P**rogrammable **G**ate **A**rray (FPGA) board (*ICE40HX1K-STICK-EVN*) and contains four BNC connectors that serve as inputs for signals from the trigger detectors. The FPGA is configured by a software that has been developed within the ITS3 project (see [18]). The setup can be configured to issue a trigger signal based either on a selected single input channel or to require a temporal coincidence of signals from a defined subset of detectors, when the rising edge of an input signal exceeds a certain predefined threshold. The trigger input signals will be synchronized to the internal 100.5 MHz clock and stretched to two clock cycles for the coincidence measurement [18]. In addition, the board is capable of using signals from any detector input, or from the dedicated BNC input connector (IN) as a veto. This veto functionality can be used to suppress the generation of trigger signals during the detector readout cycle or to operate dedicated veto detectors. Under fulfillment of the configured conditions, the system will schedule a 100 ns long trigger signal within 50 to 60 ns[18].

In the beam telescope considered here, the trigger system employs two scintillation detectors located upstream and downstream of the telescope. The logic board is configured to generate a trigger signal when a coincident signal from both scintillation detectors is present and no veto signal is received. The active area of the scintillation detectors is chosen such that the scintillators cover the sensitive area of the detector surface with minimal excess. This configuration reduces the fraction of measured particles that do not traverse all detector layers. When the setup is operated with the specified **P**hoto**M**ultiplier **T**ube (PMT) (*Hamamatsu H10492003*), it also supplies power to the aforementioned and can therefore control not only the voltage threshold but also the PMT gain. For this mode of operation, the trigger system requires an additional $-12\,\mathrm{V}$ and $12\,\mathrm{V}$ power supply.

To achieve synchronized data acquisition across all layers, the trigger signal generated by the logic board is distributed downstream to all reference planes and subsequently to the DUT (see Fig. 5.1). During a readout cycle, each DAQ board will return a BUSY signal on its BUSY OUT port, which is propagated reversely through the chain of boards to the trigger logic board. As long as any BUSY signal is active, the trigger system is inhibited from issuing further trigger signals, thereby preventing the initiation of a new event until the readout of all boards has been completed.

EUDAQ2

For both data acquisition and detector control, the *EUDAQ2* software framework is employed [19]. *EUDAQ2* is a C++-based framework specifically designed for testbeam data acquisition. It manages data streams and the control of one or more *producer* modules, which are interfacing the detectors via a run-control module. The raw data streams from the producers are merged and written to raw binary data files, which constitute the input for subsequent analysis. In addition to data handling, the software records and monitors key operational parameters of each *EUDAQ2* module [20].

In the context of the ITS3 project, modules for detector readout and control, as well as for data handling, storage, and monitoring, have been developed and integrated into *EUDAQ2*. The extended framework initializes the sensor and readout system with configuration settings provided via a dedicated configuration file. This enables the control of the front-end and readout parameters discussed in Chapter 4. During data taking, the DAQ board transmits the acquired data for each readout cycle to a PC via a USB interface. The data packet received from each sensor is processed by a dedicated producer instance, which interprets every packet as a distinct detector event.

Since this data acquisition scheme treats every detector layer as an independent instance, an asynchronous readout across layers would result in non-coincident event time windows between sensors. For an accurate reconstruction of particle trajectories, a synchronized readout across the entire telescope, coordinated, for example, by the trigger board, is therefore essential.

5.2. Testbeam at ELSA

This section describes the measurement performed during a ITS3 testbeam campaign at ELSA in February 2025. First, the ELSA facility and the E3 beamline will be introduced. After this, the telescope setup operated during this test beam is presented.

5.2.1. The ELSA Facility and the E3 Beamline

The **EL**ektronen-**S**tretcher-**A**ccelerator (ELSA) is an electron accelerator in Bonn, Germany, providing an up to 3.5 GeV electron beam [21]. The general structure of the facility can be found in Fig. 5.2. For the acceleration process, electrons are extracted from a 50 keV electron source and then pre-accelerated by the **LIN**ear **AC**celerator (LINAC)2, linear pre-accelaractor achieving a particle energy of up to 26 MeV. Following LINAC2, the electron

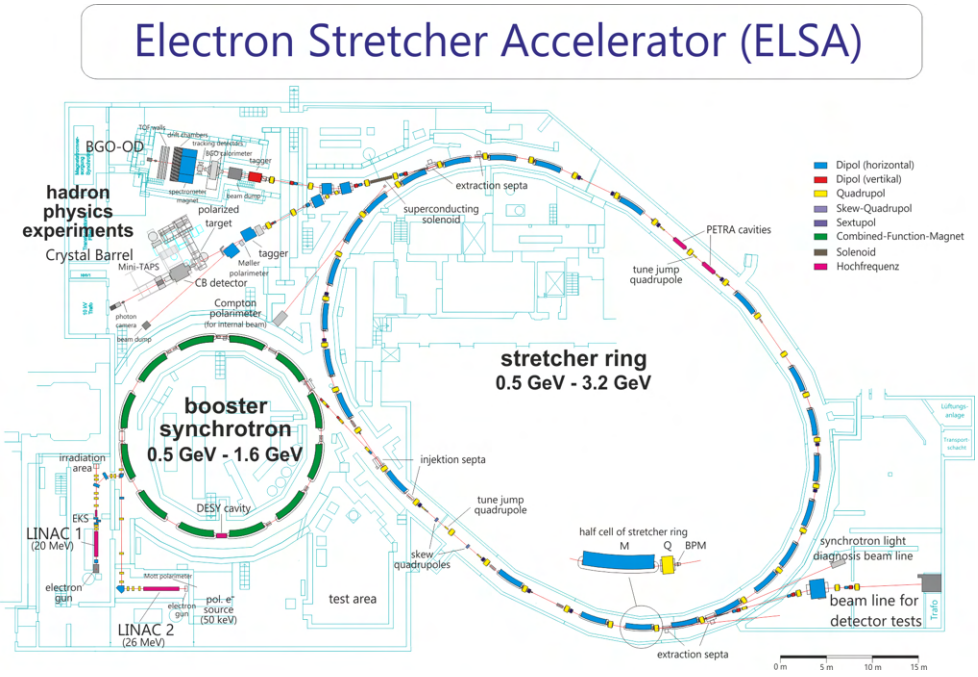


Figure 5.2.: Structural map of the ELSA facility in Bonn[22]

beam is further accelerated in the booster synchrotron system, a synchrotron achieving energies up to 1.6 GeV. In the final stage, the electron stretcher ring, the electrons are accelerated to their final energy of about 2.5 GeV to 3.2 GeV. From this point, the electron beam is ready for extraction for the two experiments CB-EKSA/Taps and BGO-OD at the first extraction point or at the second extraction point for usage at the E3 beamline, which is where the measurement used in this work was performed. In the latest test beams performed at ELSA for the ITS3 project, the extraction for E3 was performed parasitically using a septum magnet, so that extraction points 1 and 2 are served within the same operational timeframe. The E3 beamline is providing low current electron beams with beam rates between 1 kHz and 100 kHz with the beam initial energy of 2.5 GeV to 3.2 GeV. The resulting beam spot can qualitatively be described as an ellipse with an asymmetric center (see Fig. 7.18). During the performance of these testbeam a rate-dependent change of the beam profile was observed [23, 24].
A picture of this beamline can be found in Fig.5.3. The beamline features a table with a power supply for placing the test-beam set-ups, as well as a laser spot for aligning the setups in the beam.

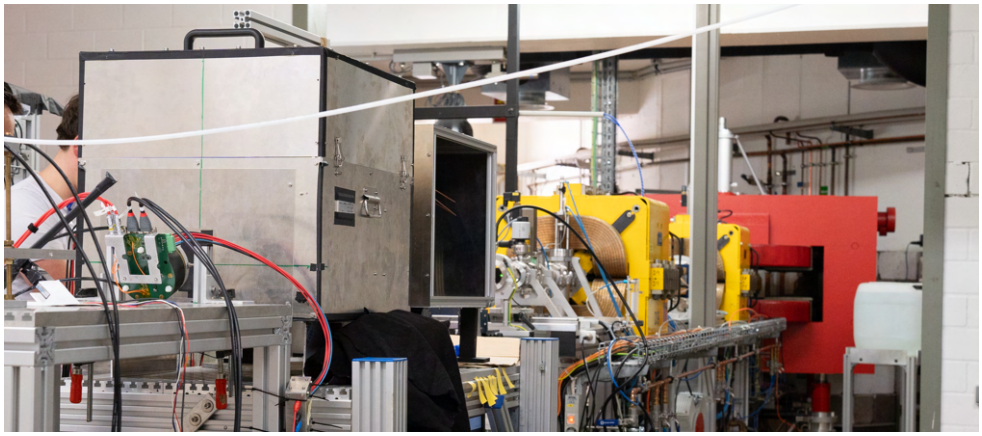


Figure 5.3.: Picture of the E3 testbeam area on a testbeam at ELSA in December 2024. From background to foreground: In red, a dipole for bending the beam; in yellow, two quadrupole magnets for shaping the beam spot; the beam outlet with a scintillator detector for beam control or a laser spot marker for alignment of the testbeam setup; A table for testbeam setups with two beam telescopes placed on it.

5.2.2. Experimental Setup at ELSA

The setup operated during the February 2025 ITS3 testbeam campaign at ELSA is a conventional babyMOSS beam telescope with a dedicated DUT (see Sec. 5.1.1). A picture of the setup operated can be found in Fig.5.4. The power supply of the complete setup was carried out by two *Rohde & Schwarz HMP4040* power supply units. As can be seen from Fig. 5.4, 6 babyMOSS reference layers have been operated in total. Just like in Fig.5.1, an innermost babyMOSS sensor (layer 3, babyMOSS-3_2_W05D5) was added and operated as DUT. The detectors' carrier cards are held in a custom-made aluminum bracket, which is screwed onto an M6 grid with a 2.5 cm spacing. To protect the sensors from light and debris, the complete setup is covered in an aluminum casing. While the power supply of the surrounding reference layers was performed via a daisy chain connected to one single channel of the power supply unit, the DUT was operated via a separate power supply chain and respective channel. For triggering the ITS3 trigger system described in Sec. 5.1.1 that is operated in coincidental operation using two 35 mm × 25 mm × 5 mm plastic scintillators (type Scionix EJ-200) each attached to a *Hamamatsu H10492003* PMT module. The trigger system is powered via a *Rohde & Schwarz HMP4040* to −12 V and 12 V via a 3-pole PCB terminal plug. For the operation in back-bias mode, a dedicated channel of the power supply is used that is connected to the respective DUT *LEMO* adapter. The telescope's geometry assumed for the analysis can be found in A.4. The data analyzed in Ch. 7 was measured under the application of a back bias V_{PSUB}=−1.2 V.

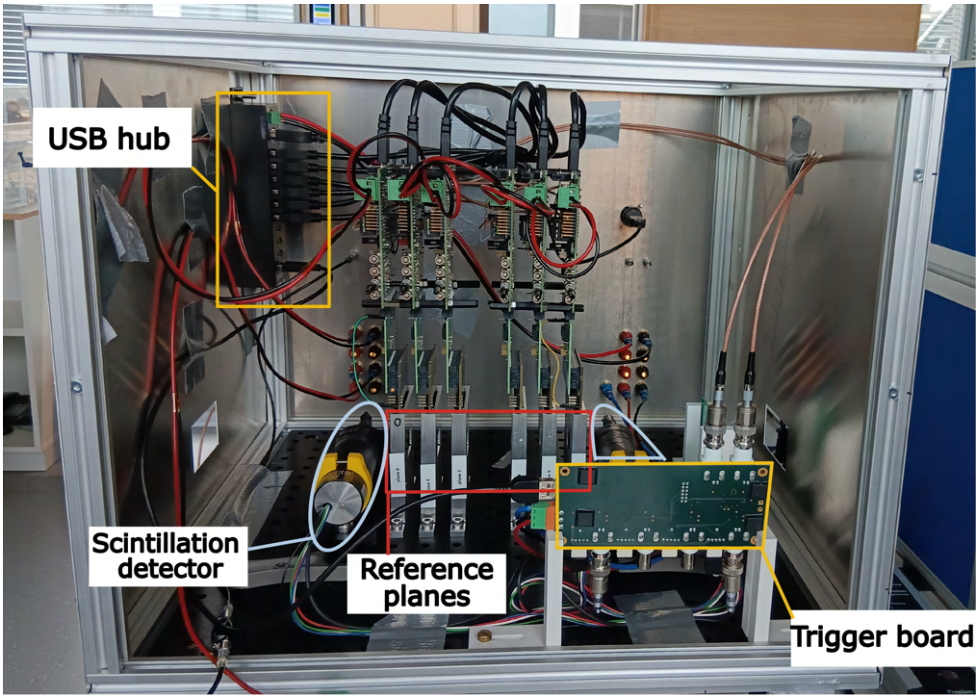


Figure 5.4.: Picture of the setup operated at the testbeam at ELSA in February 2025 [25] annotations from Alexander Rachev photograph provided with kind permission by Iaroslav Panasenko.

5.3. Local Tracking System

This section describes the setup commissioned locally at the University of Münster, which is dedicated to the measurement of atmospheric muons. As these muons constitute the particle source detected by the setup, their relevant properties are introduced first (see Sec. 5.3.1). The construction is then presented (see Sec. 5.3.2), followed by the characterization of two sets of front-end configuration used to determine an operating point for the measurements presented in Ch. 7 (see Sec. 5.3.3).

5.3.1. Atmospheric Muons

The particles measured by the local tracking system are atmospheric muons. As their properties are relevant to the design of the local tracking system as well as for the analysis presented in chapter 7, the following section will introduce their origin and properties. The composition and characteristics of cosmic rays resulting from cosmic accelerators are changed within interaction of primary cosmic rays and the atoms of the Earth's atmosphere. The particles produced in these interactions are referred to as secondary atmospheric rays.

The dominant particles of these are pions and kaons [26], which subsequently generate a muon flux via the decay channels

$$\pi^+ \longrightarrow \mu^+ + \nu_\mu, \quad \pi^- \longrightarrow \mu^- + \bar{\nu}_\mu; \quad K^+ \longrightarrow \mu^+ + \nu_\mu, \quad K^- \longrightarrow \mu^- + \bar{\nu}_\mu$$

which makes up about 80 % of the atmospheric particles arriving at sea level.
The muons arriving at sea level have a certain characteristic angular distribution and energy spectrum that arises from their origin and the underlying production processes. The key mechanisms behind these distributions will not be reviewed in detail here. Nevertheless, these characteristic distributions have an impact on the expected results, which is why an approximation of the aforementioned distributions is introduced. The following approximations of the muon flux are derived from [27].
The distribution function of atmospheric muons in regard to the zenith angle and the muon's momentum can be approximated by

$$I(E,\theta) = I_0\, N\, (E_0 + E)^{-n} \left(1 + \frac{E}{\epsilon}\right)^{-1} D(\theta)^{-(n-1)}. \tag{5.1}$$

where I_0 is the overall energy independent muon flux for $\theta = 0$ and the normalization parameter N is given by $N = (n-1)(E_0 + E_c)^{n-1}$ with the cut off energy of the model E_c and the energy loss parameter E_0. The ratio of the path length traversed by a muon arriving from an inclined direction to the path length of a muon arriving from the vertical direction $D(\theta)$ is given by

$$D(\theta) = \frac{S}{d} = \sqrt{\left(\frac{R^2}{d^2}\cos^2\theta + 2\frac{R}{d} + 1\right)} - \frac{R}{d}\cos\theta.$$

where R is the radius of the Earth and S is the inclined distance of the muon, whilst d is the vertical direction. Under the assumption of a flat earth, the function $D(\theta)$ can be approximated by $D(\theta) \approx \frac{1}{cos(\theta)}$, which results in a muon flux in dependence of the zenith angle θ

$$\Phi(\theta) = I_0 \cos^{n-1}\theta \tag{5.2}$$

where n = 3, resulting from a decay probability and the stronger absorption of muons from inclined directions, as the particle's path length within the atmosphere increases with these angles [26]. This approximation is valid for smaller zenith angles but fails to describe the data sufficiently for higher zenith angles, as can be seen in Fig. 5.5.

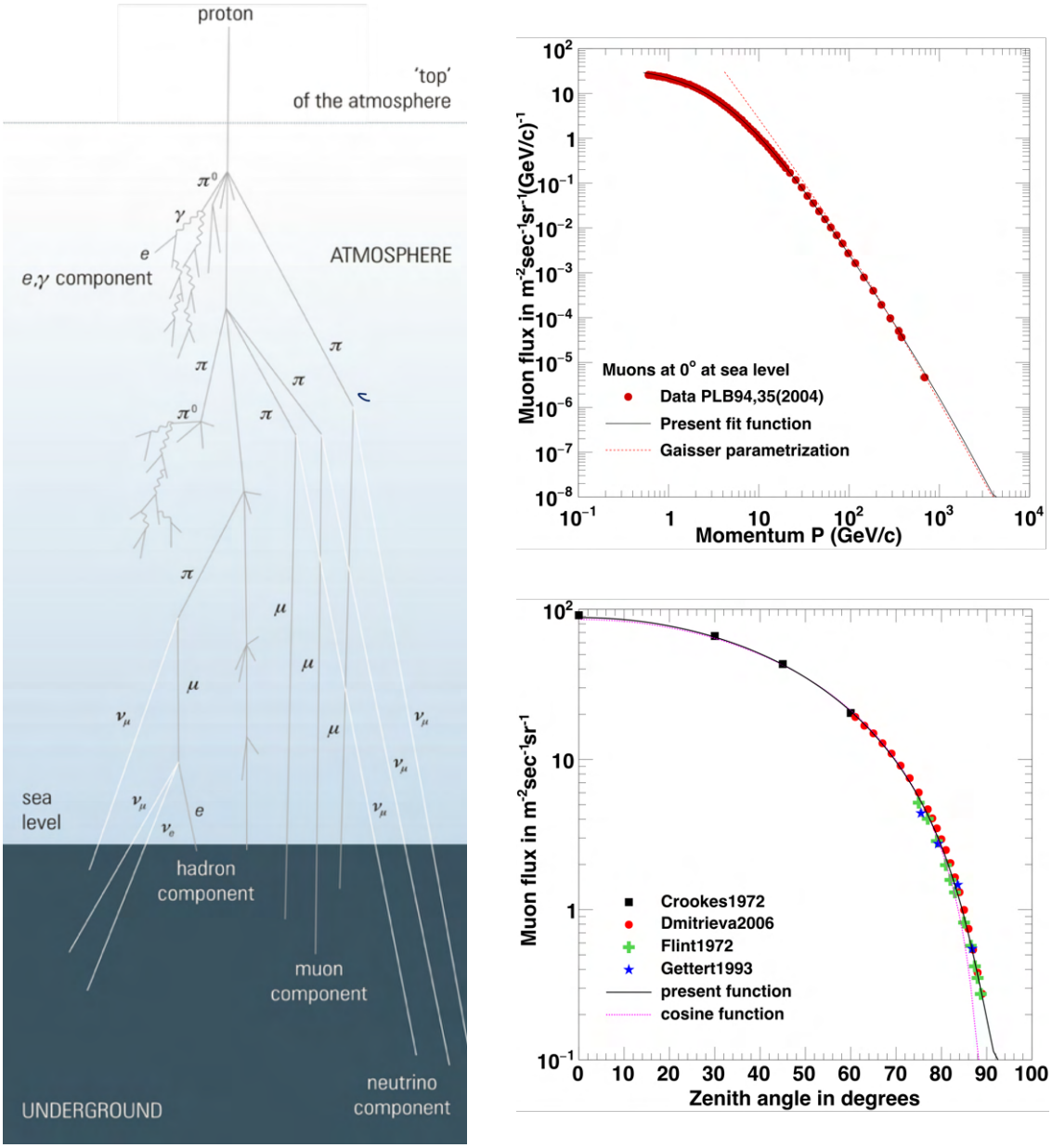


Figure 5.5.: **Left:** Production processes of secondary atmospheric particles in the atmosphere (from [26]) **Right:** Measured muon-flux at sea level and commonly used models compared to the models from [27] for the flux of atmospheric muons in dependence of the muons momentum (top) and the Zenith angle relative to the earths atmosphere (bottom) from [27].

5.3.2. Mechanical Construction and Readout Chain

The Setup commissioned within this work is dedicated to measuring atmospheric muons (Sec. 5.3.1). Conceptually, it is a streamlined version of the typical babyMOSS beam telescope (Sec. 5.1.1), optimized for the predominantly vertical incidence of atmospheric muons on the Earth's surface. Accordingly, the entire system is arranged in a vertical stack. Since the setup is not primarily intended for sensor characterization, no sensor is explicitly

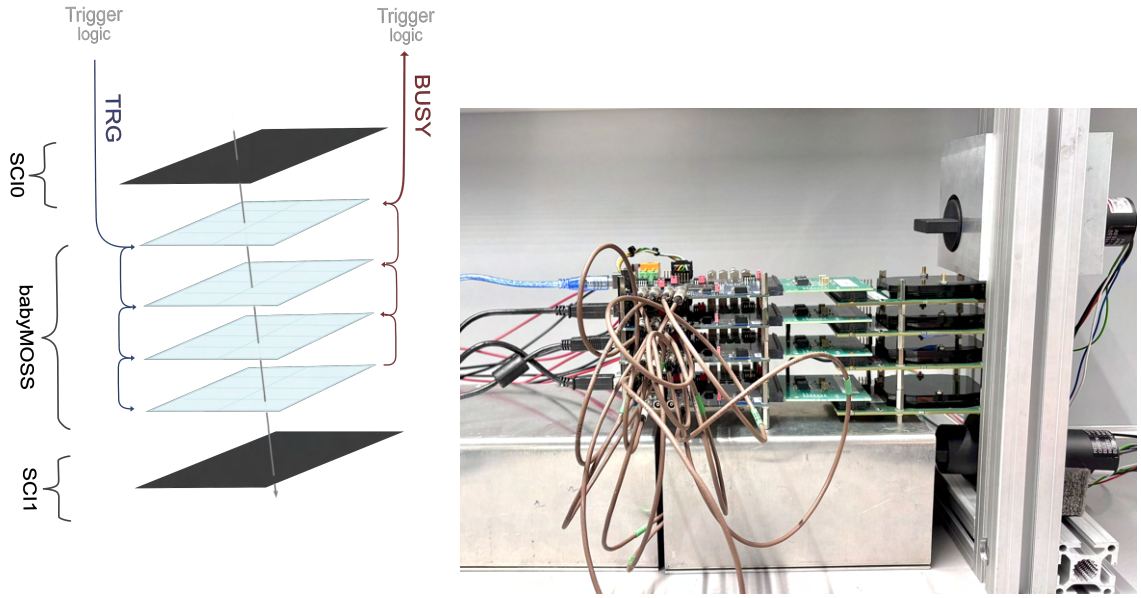


Figure 5.6.: (1) Conceptual sketch of the local tracking system. The telescope is stacked vertically and contains only four layers, of which none is declared as DUT. The signals are therefore propagated from top to bottom and backwards
(2) A picture of the local tracking system. The brown *LEMO* cables are propagating the TRG and BUSY signal, the babyMOSS sensors themselves are covered with the black polycarbonate covers, and the scintillators are installed using frame holders.

set as the DUT and therefore no sensor has a separate power supply or a specific position in the trigger chain. Instead, the trigger signal is propagated downwards through all detector layers, while the busy signal is routed in the opposite direction, back upwards to the trigger logic. Instead of an aluminum casing, the telescope is shielded from the light and debris via protective polycarbonate covers. Each test system module is independently supplied with 5 V from a *Rohde & Schwarz HMP4030* power supply via the PCB terminal connector of the DAQ board. In the operation, no DUT is specifically determined.
Although no sensor has been declared as DUT in the measurement, further discussions,

such as the attempted sensor characterization (see Sec. 7.3.2.4), will handle the second-highest sensor (layer 1,babyMOSS-3_4_W20E1) as DUT. This sensor has a defective tb region 2 and is therefore least suitable as a reference layer for track reconstruction. The trigger system employs two plastic scintillators connected to *Hamamatsu H10492003* PMT modules with internal amplification. Trigger management is handled by an ITS3 trigger board, which is powered from −12 V to 12 V by a *Rohde & Schwarz HMP4030* via a 3-pole PCB terminal plug. The scintillator detectors PMTs are powered directly from the trigger board, enabling precise control of the PMT supply voltage, and thus the PMT gain through the trigger board interface. The telescope layers are mounted on steel standoffs and positioned on an aluminum box, creating sufficient clearance to install an additional scintillator beneath the lowest detector layer. The measured geometrical properties of the setup can be found in Tab. A.3

5.3.3. Threshold and Fake-Hit-Rate Characterization

Before the setup is operated, a suitable working point of the babyMOSS front-end was established. To this end, the dependence of the pixel threshold and the FHR on the relevant transistor settings is characterized. For all measurements performed with the local tracking system presented in this work, no bias voltage V_{PSUB} was applied, which corresponds to a higher threshold over all measurements in comparison to the V_{PSUB} operation performed at ELSA. As described in Sec. 4.1.3, the babyMOSS front-end can be configured by adjusting

Table 5.1.: Front-end transistor settings for the two Setting combinations used. The standard settings (left) and the settings used for the final measurement performed with the local tracking system (right).

Setting	**Settings 1 (DAC)**	**Settings 2 (DAC)**
IBIAS	62	62
ISBIASN	100	100
IRESET	10	5
IDB	50	10
VSHIFT	192	191
VCASN	64	30
VCASB	var	var

eight fundamental transistors. A key parameter determining the pixel threshold is the bias of the feedback transistor M7, referred to as VCASB. The babyMOSS has been characterized using two different complete front-end configuration sets, while VCASB is systematically varied. For each configuration, the FHR and threshold are measured to determine an appropriate value of the VCASB parameter. The corresponding transistor settings are listed in Tab. 5.1.

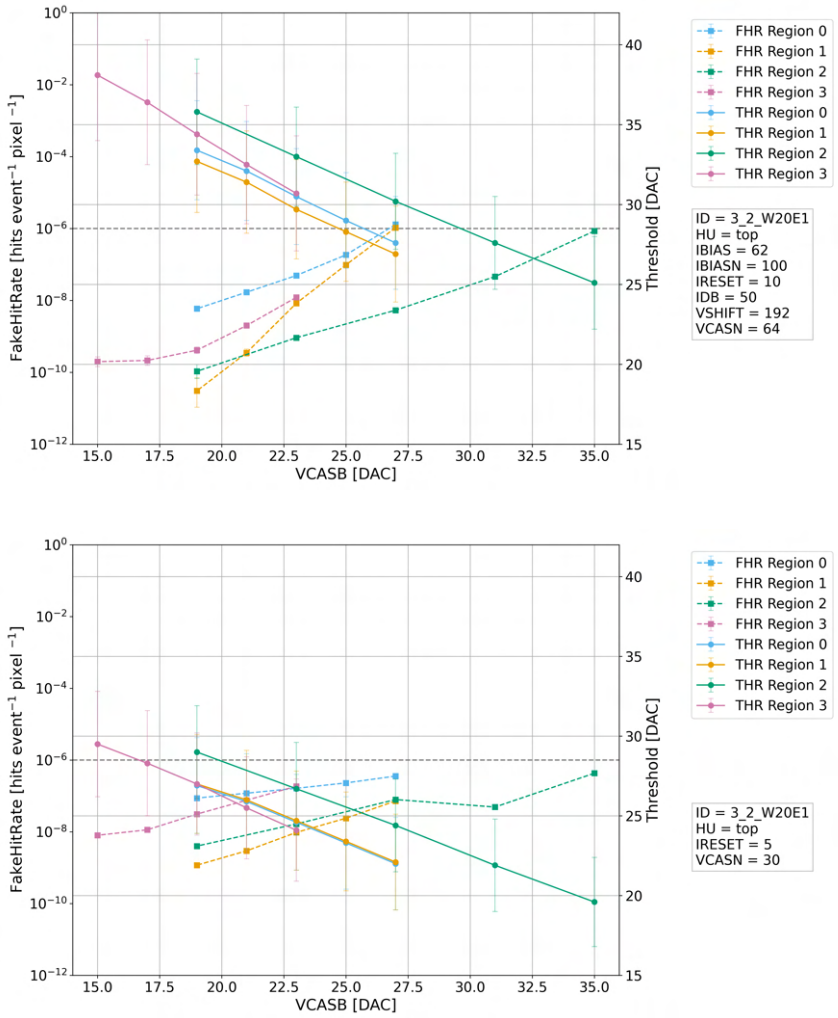


Figure 5.7.: Results of threshold and FHR scans of the four tb regions of the babyMOSS-3_2_W20E1 sensor, for two sets of fundamental transistor settings and varying VCASB at room temperature ((1): Set 1, (2) Set 2 from Tab. 5.1) connecting lines do not represent measured or fitted values but just connect the points of measurement for better visibility.

Representative results of the threshold and FHR scans are shown in Fig. 5.7 (additional results for the remaining sensors are provided in App. Sec. D). The data exhibit a clear dependence of the average pixel threshold on VCASB: an increase in VCASB leads to a reduction of the average threshold for both front-end configurations. An increase in the FHR is observed in both configurations, as it is expected from previous measurements with this front-end [12].

For the sensor shown in Fig. 5.7, the FHR remains below the ITS3 requirement of $\mathrm{FHR}_{\mathrm{max}} = 10^{-6}$ hits/(event·pixel) [6] over the investigated VCASB range, whereas some of the other sensors exhibit higher FHRs at elevated VCASB values (e.g. Fig. A.2). Furthermore, it can be observed that, at a given VCASB value, all regions reach lower thresholds for configuration 2 in comparison to configuration 1, while the corresponding FHR remains at a comparable level to that obtained with configuration 1.

6. Reconstruction and Analysis Framework

To perform sensor characterization using data recorded by the setups described in Ch. 5, the data from all sensors involved must be analyzed in a unified process. Within the ITS3 project, the data format produced by the MOSS and babyMOSS was incorporated into the *Corryvreckan* analysis framework. This makes it the commonly used approach for analyzing data from a babyMOSS telescope. However, this common approach is not perfectly suitable for the data recorded with the local tracking system as will be discussed in Sec. 6.1. The typical steps of the full reconstruction chain are shown in Fig. 6.1. The

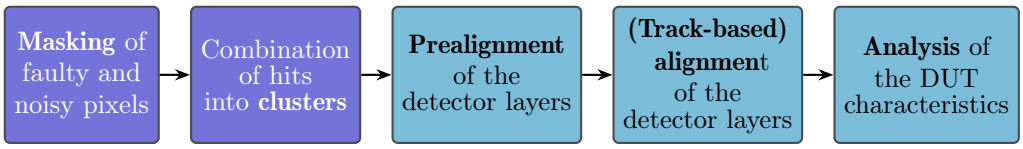


Figure 6.1.: Typical reconstruction chain for the DUT characterization. The steps performed by *Corryvreckan* in this work are marked in blue and the steps performed by the *Python3*-based framework developed in Sec. 6.2 marked in cyan.

figure also shows which steps will be carried out with the *Corryvreckan* framework and which will be performed by the *Python3*-based framework developed which is presented in Sec. 6.2 of Ch. 7.
This chapter will therefore introduce the elements of analysis from *Corryvreckan* used within this work in Sec. 6.1 and will discuss why it is not entirely suitable for the data measured with the local tracking system. The *Python3*-based framework developed within this work as an alternative to the *Corryvreckan* framework for the remaining steps of the typical analysis approach will then be presented in Sec. 6.2.

6.1. Corryvreckan

Corryvreckan is a modular framework for the reconstruction and analysis of testbeam data, in which the reconstruction chain is split into individually configurable modules. This section introduces the modules used in this work based on the *Corryvreckan* manual [28] and subsequently discusses why the framework alone is not sufficient for the reconstruction

and analysis of data recorded with the local tracking system (see Sec. 6.1).
The data reconstruction chain depicted in Fig. 6.1 is broken down into a sequence of discrete processing steps, each executed by individually configurable modules. Each of the modules is initiated via a corresponding configuration file that calls the modules required for the step of the reconstruction chain. In this work, only the first two steps are performed in *Corryvreckan*, while the remaining steps are carried out in the framework described in Sec. 6.2.
The following section provides a detailed description of the modules employed in this work. The advanced core components of the standard *Corryvreckan* reconstruction chain are not included, as they were not applicable in this work.

EventLoader

The framework includes an extensible eventloader module for reading data from the original raw data format. The framework not only supports the reconstruction of a single detector type within a single setup, but also allows the integration of data from multiple detector types into a unified reconstruction environment through a broad range of event loader modules. Among these, the `[EventLoaderEUDAQ2]` allows reading data acquired with *EUDAQ2* (see Section 5). When provided with the correct detector type, the framework routes the data to the corresponding *EUDAQ2* `[StandardEventConverter]` module, a module adjusted to the specific detector geometry, and converts the raw data files into the native data format of the *Corryvreckan* framework. The module that was developed in the context of ITS3 treats every region of a babyMOSS sensor as an individual instance of the *EUDAQ2* `[StandardPlane]` class, i.e., as an independent detector unit. Consequently, all regions will be handled as separate sensor entities in the following steps of the reconstruction chain within *Corryvreckan*.

MaskCreator

For an accurate reconstruction of particle trajectories, it is beneficial to minimize, as far as possible, the contribution of noisy pixels to the data set. The *Corryvreckan* data framework supports the exclusion of individual pixels based on their spatial coordinates when provided with an appropriate mask file. Such mask files can either be generated externally by a dedicated algorithm, for example using the measurement data obtained in the procedures described in Chapter 5, or they can be created within the reconstruction chain by the `[MaskCreator]` module. In this study, the `[MaskCreator]` is operated in frequency mode, in which a predefined threshold on the per-pixel hit rate is applied to identify noisy

pixels. Pixels exhibiting counting rates exceeding the configured frequency threshold are classified as noisy, subsequently masked, and thus excluded from all further analysis steps.

Clustering4D

To mitigate the effects of charge sharing (see Sec. 6.2.5.1), the positional information is refined by combining the hit information into clusters. This clustering procedure is carried out via the `[Clustering4D]` module. Since neither timing nor charge information is obtained from the sensor, the module determines the local spatial coordinates by averaging the positions of neighboring hits located within a predefined radius of one pixel around a given hit. The module allows to exlude all hits that are falling out of a pre-defined **R**egion **O**f **I**nterest (ROI). As parts of the babyMOSS underside are obscured by the PCB of the carrier card, it is common practice to define a ROI in the PCB-free area in order to reduce the effect of multiple scattering caused by the increased material budget in this peripheral region. Based on the determined local position of the cluster, the module reconstructs the global position with respect to the given global coordinates and geometry of the sensors. The data can be extracted via the `[FileWriter]` module that stores all information obtained[1] into a textfile.

Limitations in the further Reconstruction

Following the reconstruction of the probable particle impact position, the detector's physical misalignment is corrected to enable an accurate reconstruction of particle trajectories. The limitations of the current state of the framework for the measurements performed in this work can be subdivided into two main aspects. First, the number of reconstructed particle trajectories in this study is expected to be several orders of magnitude lower than in a typical test-beam campaign, since the flux of impinging particles in an atmospheric-muon measurement is significantly reduced and the time frame of data taking is limited to a certain extent. Second, to the best of the author's knowledge, the framework is not capable of treating all regions of a babyMOSS layer as a single, fully integrated sensor module. Within the current framework, each sensor unit is associated with one specific layer. In contrast, in the case of babyMOSS and the present processing approach, multiple sensor modules (i.e., distinct regions) operate on the same physical layer (i.e., the babyMOSS), which is not natively supported by the existing framework design. Therefore, the common

[1] This includes the Region identification number, local and global position as well as the size of cluster in rows and columns and the collected charge.

approach in ITS3 sensor characterization consists of treating each DUT region, together with the corresponding regions on the reference layers, as an independent sensor stack. In test-beam campaigns, these limitations are less critical, because the event statistics within a stack of regions are generally sufficient for robust alignment and subsequent analysis owing to the substantially higher particle rates. Moreover, the comparatively low angular divergence of a particle beam reduces the probability that an individual particle will traverse multiple distinct regions within the telescope, further simplifying the track reconstruction. This contrasts with the expected angular distribution of atmospheric muons (Sec. 5.3.1).

6.2. The Python3-Based Framework

As described in Sec. 6.1, the *Corryvreckan* framework is not sufficient for the full reconstruction of the data taken within this work. Further reconstruction is therefore carried out in an independent framework that extracts data from text files obtained from the *Corryvreckan* clustering module. To allow accessibility for a wide range of users, a *Python3*-based approach is chosen. The following sections will introduce the implemented approach[2] to track reconstruction in Sec. 6.2.2 and the detector alignment procedure in Sec. 6.2.4. The proceedings in the developed chain, will still follow the standard reconstruction chain and ideas of the *Corryvreckan*-framework. To verify data and reconstruction procedures, the module also includes simulation of atmospheric particles on a given detector geometry, which will be presented in Sec. 6.2.3. The last section will then present an approach to DUT sensor characterization.

6.2.1. Telescope and Eventreader

The event reader, telescope geometry reader, and geometry visualization are modified versions of an existing framework originally developed for previous test beam data analysis in [33], and are used here with the kind permission of the original author, Berkin Ulukutlu. The cluster converter turns the *Corryvreckan* [`Clustering4D`] module output file into a compact *pickle* file that contains all available cluster information, such as local and global positions as well as size. The event reader scans the *pickle* file event-by-event and instanti-

[2]It should be noted at this point that, for the implementation and debugging of the specific code developed to put the concepts listed here into practice in Python 3, various tools were used in some instances to assist with the process. However, the implementation is based solely on the ideas mentioned here and is the work of the author and the sources cited. The tools used, therefore, do not constitute a conceptual source of the content presented. As a standard practice has not yet been established, the tools/models used are cited directly here: [29], [30], [31], [32]. After using the respective tool/model, the author reviewed and edited the content as needed and takes full responsibility for the content of this thesis.

ates each cluster, with all information available, in separate events. The detector geometry is obtained from a geometry file using the same syntax as *Corryvreckan* detector configuration files via the telescope geometry reader that instantiates each babyMOSS layer, including all given regions, with their respective rotation and global positions as a telescope. Besides this, scintillators can be instantiated, including their size and global position, based on an independent configuration file.

6.2.2. Tracking

Definition 4. *Local coordinate system: Cartesian coordinate system (u,v,m) defined with respect to the center of a single sensor module.*

Definition 5. *Global coordinate system: Cartesian coordinate system (x,y,z) defined with respect to the full detector system.*

The track reconstruction is performed on the basis of the global positions of the clusters reconstructed from a single event. After the masking of pixels (see Sec. 6.1), each cluster is treated as an equally likely potential particle intersection. As a model of the particle trajectory, a simple three-dimensional straight-line was selected, due to the high expected energy regime, which is associated with reduced multiple scattering (see Sec. 3.1.1) and the simplicity of the approach. However, it must be noticed that this is a rough approximation that neglects multi-scattering completely.
To reconstruct the track and allow comparability between track candidates, an χ^2 reduction-based approach is chosen that will be introduced in the following.
The quality of the particle trajectory reconstruction is evaluated by a χ^2 calculation following

$$\chi^2 = \sum_k \varepsilon^T_{\text{track,k}} V_k^{-1} \varepsilon_{\text{track,k}}, \qquad V = \begin{pmatrix} \sigma^2_{u,\text{sensor}} & 0 \\ 0 & \sigma^2_{v,\text{sensor}} \end{pmatrix} \tag{6.1}$$

where the index k denotes the clusters considered for the respective track [34]. In the given equation, $\varepsilon_{\text{track,k}}$ is the residual of each cluster associated with the track and V_k is the covariance matrix of the cluster measurement, where in local coordinates σ_{sensor} is the spatial resolution of the measuring sensor in u and v direction. The spatial resolution σ_{sensor} is assumed to be the binary resolution of the sensor $\sigma_{bin} = p/\sqrt{12}$ where p is the pixel pitch of the sensor (compare Sec. 6.2.5.1). The residual vector $\varepsilon_{\text{track}}$ of a cluster can be derived from local coordinates via

$$\varepsilon_{\text{track}} = \begin{pmatrix} u_x - u_m \\ v_x - v_m \end{pmatrix}. \tag{6.2}$$

where u_x and v_x denote the sensor track intersection in local coordinates while u_m and v_m

refer to the measured cluster position. In the following, the reduced χ^2_r, i.e., the χ^2 normalized to the number of available **d**egrees **o**f **f**reedoms (dofs), i.e., the number of measurements minus the number of fitted track parameters, will be used as the final indicator of a track's fit quality.

Given the high energy regime, the fact that the detector layers can be assumed as thin, and that no magnetic field is applied, the particle's trajectory is modeled via a straight line equation

$$f(z) = \begin{pmatrix} x_0 + m_x z \\ y_0 + m_y z \end{pmatrix}. \tag{6.3}$$

where x_0 and y_0 denote the functions x- and y-intersects and m_x and m_y are the slope of the trajectory in x and y direction.

The track reconstruction of a given cluster combination is then performed via a weighted parameter fit of Eq. (6.3), minimizing Eq.(6.1). The fit is carried out by solving the weighted problem

$$\begin{pmatrix} \frac{1}{\sqrt{V_{xx,1}}} & \frac{1}{\sqrt{V_{xx,1}}} z_1 \\ \vdots & \vdots \\ \frac{1}{\sqrt{V_{xx,k}}} & \frac{1}{\sqrt{V_{xx,k}}} z_k \end{pmatrix} \begin{pmatrix} x_0 \\ m_x \end{pmatrix} \stackrel{!}{=} \begin{pmatrix} \frac{1}{\sqrt{V_{xx,1}}} x_1 \\ \vdots \\ \frac{1}{\sqrt{V_{xx,k}}} x_k \end{pmatrix} \tag{6.4}$$

via the *linalg.lstsq()* least-square solver from the *numpy* [35] library for the x and y part of (6.3). In the given equation, the matrix elements V_{xx} and V_{yy} denote the matrix elements of the covariance matrix of the cluster position in global coordinates.

This procedure is performed by filtering the events for a pre-configured minimal number of layers that have at least one cluster measured. After this event selection, every cluster permutation containing the maximum amount of hit layers within the event is iterated, and the track with the lowest χ^2_r is selected for further processing. For selecting the tracks, a maximal χ^2_r as well as a spatial cut in the form of a maximum allowed per-cluster residual $|\varepsilon|$ can be set up. If no track can be found to match the criteria within the first set of cluster permutations, the number of minimum hit layers per permutation is reduced, and the procedure is repeated until a track matching the criteria is found or the minimum number of hit layers is reached, and no track will be returned.

As for the DUT analysis, the unbiased residuals $\varepsilon_{track,DUT}$ and $\varepsilon_{traj,DUT}$ are required; excluding the track finding algorithm allows for excluding all clusters on a certain custom DUT-layer. If a DUT-layer is set, the algorithm searches a cluster on the DUT in a given radius $\varepsilon_{DUT,max}$ around the track intersection point q_x in local DUT coordinates.

6.2.3. Simulation

To validate, supplement, and test the methodology and software developed within this section, a simulator module was implemented. This module enables different particles with custom parameters to be simulated on a given detector geometry. The goal is to recreate atmospheric muon events and accelerator beam events in order to obtain expected values for the parameters and distributions used in the analysis, and to determine additional parameters that are necessary for carrying out the analysis.

Atmospheric muons

The simulation of atmospheric muons is employed both to verify the performance of the individual software modules and to produce reference datasets. As input, the simulator can take any given detector geometry, which serves as the basis for the simulation. The process is initiated at the uppermost sensor or scintillator, where a random reference point is generated. From this point, an initial particle trajectory is defined by assigning a random azimuthal angle drawn from a uniform distribution over all angles and a zenith angle sampled according to a $\cos\theta_2$ distribution (see Sec. (5.2)). Multiple scattering (see Sec. 3.1.1) is modeled by placing discrete scattering centers along the simulated track. At each scattering center, the original trajectory is altered by applying a random azimuthal angle drawn from a uniform distribution (assuming isotropic scattering) and by adding a scattering angle $\theta_{\text{Scattering}}$ to the initial zenith angle. The scattering angle is sampled from a Gaussian distribution as defined in Eq. (3.3). The standard deviation of this distribution is approximated using the Highland formula (Eq. (3.4) resp. (3.5)). Consequently, sampling from this distribution requires several input parameters that describe both the particle properties and the material budget of the scatterers. For the simulation the particle mass and charge are configurable via the interface, with a muon mass of $m_\mu = (105.658\,375\,5 \pm 0.000\,002\,3)\,\text{MeV}$ [10] and an electron mass of $m_{e^-} = (0.510\,998\,950\,69 \pm 0.000\,000\,000\,16)\,\text{MeV}$ [10] where the respective uncertainty of measurement is neglected. A fixed particle momentum can be specified. For a more realistic representation of the scattering behavior of atmospheric particles, the particle energy can alternatively be drawn from the distribution given in Eq. (5.1), and the corresponding momentum is then computed via $p = \sqrt{E^2 - m^2}$. The parameters for the sampling of Eq.(5.1) were thereby extracted from [27] for a dataset recorded at Durham (UK) and can be found in Tab. A.2.

The particle is subsequently propagated through the specified detector configuration, with the cumulative effect of multiple scattering incorporated by applying the above procedure at each scattering center. The corresponding values for the radiation lengths X_0, and thus

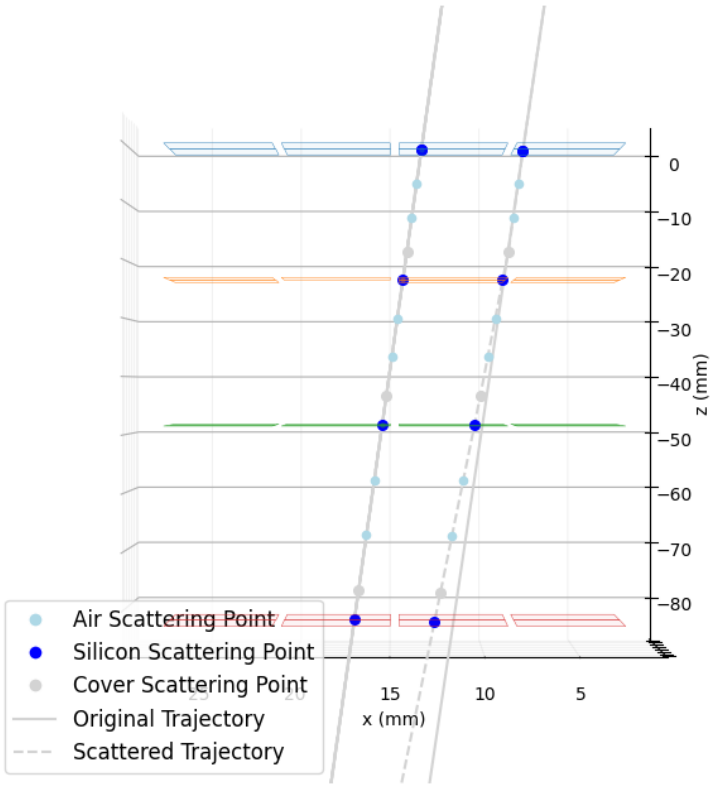


Figure 6.2.: Example of the simulated trajectory of a slightly scattered atmospheric muon (left) with and a highly scattered muon atmospheric (right)

the corresponding material thickness fractions x/X_0, are summarized in Tab. 6.1.

Scatterer	x/X_0
Cover (Polycarbonate, $x \approx 1\,\text{mm}$)	$X_0 = 34.59\,\text{cm}$ [10] $x/X_0 = 0.289\%$
Air (dry, 1 atm, e.g. $x = 1\,\text{cm}$)	$X_0 = 30\,390\,\text{cm}$ [10] $x/X_0 = 0.00329\%$
babyMOSS	$x/X_0 = 0.007\%$

Table 6.1.: Material budget contributions assumed for the different scattering media.

For the babyMOSS detector, a total material budget is assumed to be known, and it is further assumed that the resulting multiple scattering can be completely characterized by this effective material budget. The babyMOSS covers (see Fig. 5.6) are represented in the model as polycarbonate. The air gap, which in reality forms a comparatively thick scattering region, is approximated in the simulation by two thin air-scattering layers positioned symmetrically along the distance between one babyMOSS layer and the cover of the following layer. This was adapted from [17]. An illustration of the simulated scattering sequence

along the trajectory for two atmospheric muons is shown in Fig. 6.2, where a strongly scattered case for the lower-energy muon is chosen. One can clearly observe how the highly scattered trajectory significantly deviates from the particle's initial path.

From each scattering element, the trajectory is propagated further until it reaches the next scattering layer or intersects a sensor. Since a ROI is also defined in the final analysis, the simulator provides the option to specify an on-sensor ROI and to register only those trajectory intersections that lie within this ROI as sensor hits. For every sensor hit, both the true impact position $\mathbf{q}_{\text{traj}}$ and the center coordinates $\mathbf{q_m}$ of the hit pixel are recorded. This allows for an advanced residuals estimation

$$\varepsilon_{\text{traj}} = q_{\text{traj}} - q_x \tag{6.5}$$

that does consider the distance between track impact position q_x and impact position of the simulated trajectory q_{traj} on a layer. For subsequent analysis, the pixel-center coordinate is used to emulate a more realistic sensor spatial resolution. The pixel locations within the matrix are modeled as an ideal rectangular lattice, constructed by repeatedly adding the pixel pitch to the matrix's corner coordinate. In practice, this means that every hit is rounded up to the nearest determined pixel center coordinate, neglecting the effect of charge sharing (see Sec. 6.2.5.1). The simulated output is generated in the same format as the experimental data and can therefore be processed using the identical reconstruction and analysis pipeline.

Accelerator Beam

The simulation of an accelerator beam applies the same particle propagation procedure as the simulation of atmospheric muons, but uses different starting parameters. The beam is assumed to be Gaussian-shaped in x and y direction around the beam center $\underline{\mathbf{R}}_{center,i}$ with a standard deviation of $\sigma_{beam,i}$. This results in an elliptical shape for $\sigma_{beam,x} \neq \sigma_{beam,y}$. Also, it is assumed that the beam has a certain spread θ_{beam} around the beam axis. To simulate this, a random point on the first scintillator or sensor layer is sampled from the Gaussian distributions shaped by $\underline{\mathbf{R}}_{center,i}$ and $\sigma_{beam,i}$. Then, an azimuthal angle is sampled uniformly, again assuming isotropic scattering, and a zenith angle is sampled following a Gaussian distribution centered at 0 with a width of the beam angle θ_{beam}. From this point, the scattering and propagation process is carried out in the same way as described in Sec. 6.2.3.

6.2.4. Alignment Procedure

An important part in the reconstruction of physical events within a detector is the transformation from a sensor system of reference to the global lab-system. The transformation of the pixel addresses to the detector's local Cartesian coordinate system is in this setup carried out via the clustering module, which transfers the hit position of a cluster to the local coordinate system based on the on-chip pixel position. As in a track reconstruction as performed within this work, not only the positional information of a single sensor but also of the complete detector setup is required. The next step is to transfer each sensor's local positions to the global detector framework, where the positional information is considered relative to a certain reference plane, so an event can be reconstructed within the detector frame. The transformation of a global position vector $\mathbf{r}$ to the corresponding local coordinate vector $\mathbf{q}$ is given by

$$\mathbf{q} = \underline{\mathbf{R}}(\mathbf{r} - \mathbf{r}_0), \tag{6.6}$$

where $\mathbf{r}_0$ denotes the initial assumed center position of the sensor and $\underline{\mathbf{R}}$ is the rotation matrix specifying a sensor's initially assumed orientation in the global coordinate system. To determine these transformation parameters, the detector is physically measured, and the obtained information (from now on referred to as initial geometry) is used to reconstruct a cluster's global position. As measurements are limited in their positional resolution, the initial geometry is imprecise to a certain degree, limiting the precision of the reconstruction of physical events. A common approach is therefore to increase the precision of this transformation based on the recorded data in a process referred to as alignment. The overall obstacle of the processes can be described by the determination of the corrections of the translational offset $\Delta\mathbf{q} = (\Delta u, \Delta v, \Delta w)$ and a rotation $\Delta\underline{\mathbf{R}}$. The corrected transformation can then be written as

$$\mathbf{q} \;\rightarrow\; \mathbf{q}_c = \boldsymbol{\Delta}\underline{\mathbf{R}}\,\underline{\mathbf{R}}(\mathbf{r} - \mathbf{r}_0) - \Delta\mathbf{q}. \tag{6.7}$$

The alignment procedure employed here can be subdivided into two stages: a coarse, correlation-based prealignment and a more precise, track-based alignment.

6.2.4.1. Prealignment

The prealignment is the first step in the applied alignment procedure. The goal is to apply a fast non-track-based coarse alignment to allow track reconstruction in the next step. For the prealignment, one detector layer is chosen as the reference layer[3], and the remaining,

[3] At this point, it should be noted that the reference layer in the alignment does not, in itself, relate to the reference layers in the setup's construction. It is simply a matter of examining the misalignment relative

non-reference layers are aligned iteratively, proceeding from the geometrically highest to the lowest layer.
It is assumed that, for a properly aligned setup, a particle traversing the telescope under a (near-)vertical incidence angle produces hits in a certain distribution around the identical local coordinates in each sensor, which follows from the manifold aspects of multiple scattering and further fluctuations that shape the incident particle's path. The relative physical shift between two layers can thus be extracted from the offset observed in the differences of the hit positions expressed in their respective local coordinate systems. Since the track incidence angles follow a certain distribution, this offset is determined from the distribution's center position.
In the iterative procedure, for each non-reference layer, all available events are processed, and the differences between the cluster positions in the local u and v coordinates are accumulated. The resulting distributions are histogrammed and fitted with a Gaussian function

$$f(\mathbf{r}_{i,j}) = \frac{1}{\sigma_{i,j}\sqrt{2\pi}} \exp\left[-\frac{(\mathbf{r}_{i,j} - \mu_{i,j})^2}{2\sigma_{i,j}^2}\right], \quad i = u, v;\ j = 0, 1, 2, \ldots, N_{\text{layers}}, \tag{6.8}$$

where $\underline{\mathbf{R}}_{i,j}$ denotes the positional difference between hits in the respective layers, $\mu_{i,j}$ is the mean of the distribution, and $\sigma_{i,j}$ is its standard deviation. The positions of the layer centers, as well as the corresponding cluster coordinates, are then corrected by shifting them by the mean value $\mu_{i,j}$ obtained from the Gaussian fit e.g. $\Delta q_{\text{prealignment}} = (\mu_{u,j}, \mu_{v,j}, 0)$.

6.2.4.2. Track-Based Alignment

The precise track-based alignment step does not only consider the x and y offset of each layer, but also the vertical z misalignment as well as the rotation misalignment of each sensor where $\underline{\mathbf{R}}$ will be given by $\underline{\mathbf{R}} = \Delta\underline{\mathbf{R}}_\gamma \Delta\underline{\mathbf{R}}_\beta \Delta\underline{\mathbf{R}}_\alpha$, with $\Delta\underline{\mathbf{R}}_\alpha$, $\Delta\underline{\mathbf{R}}_\beta$ and $\Delta\underline{\mathbf{R}}_\gamma$ denoting the rotation matrices corresponding to small rotations by $\Delta\alpha$, $\Delta\beta$ and $\Delta\gamma$ around the current u-, v- and w-axes of the sensor. The process is a track-based approach following the descriptions of [34].

Layer Alignment To determine the alignment parameters of a single layer, the track-finding algorithm (see Sec. 6.2.2) is applied to the data in order to obtain the current track residuals ε (see Eq. (6.2)) for each sensor layer. The alignment procedure is carried out as a minimization of the track χ^2 (see Eq. (6.1)) with respect to the alignment parameter vector $\mathbf{p} = (\Delta u, \Delta v, \Delta w, \Delta\alpha, \Delta\beta, \Delta\gamma)$, based on the correction of the track intersection

to a reference point (the selected reference layer), which is regarded as fixed and is also referred to as the reference layer.

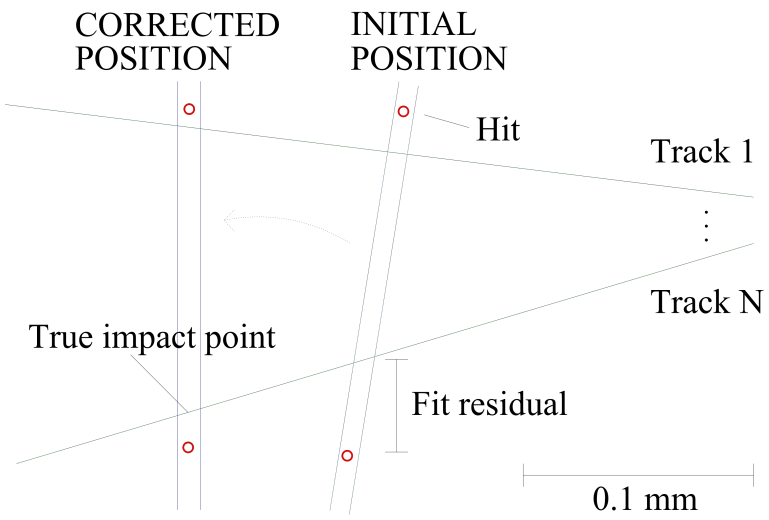


Figure 6.3.: Sketch of an aligned (left) and a unaligned sensor in the initially assumed geometry (right) in track reconstruction taken from [34]

point $\mathbf{q}_x^c$ in local coordinates, under the assumption that tracks are straight in the vicinity of the sensor. Effectively, this procedure minimizes the residual of the reconstructed track intersection and the measured position in the local system ε_{track} (see Eq.(6.2)). A sketch of the effect of the shift can be seen in Fig. 6.3. The general solution of this χ^2-minimization problem of the incremental alignment parameter $\delta\mathbf{p}$ leads to

$$\left[\sum_j \underline{\mathbf{J_j}}^T \underline{\mathbf{V_j}}^{-1} \underline{\mathbf{J_j}}\right] \delta\mathbf{p} = \left[\sum_j \underline{\mathbf{J_j}}^T \underline{\mathbf{V_j}}^{-1} \varepsilon_\mathbf{j}\right], \tag{6.9}$$

where $\underline{J}_j = \nabla_\mathbf{p}\, \varepsilon_j(\mathbf{p})$ is the Jacobian matrix of the residual $\varepsilon_j(\mathbf{p})$ with respect to the alignment parameter vector $\mathbf{p}$, and $\underline{V}_j$ is the covariance matrix of the corresponding measurement. Under the assumption of small misalignment angles, the Jacobian matrix can be approximated by

$$\underline{\mathbf{J_j}} = \begin{pmatrix} -1 & 0 \\ 0 & -1 \\ \tan\psi & \tan\vartheta \\ v_x \tan\psi & v_x \tan\vartheta \\ u_x \tan\psi & u_x \tan\vartheta \\ v_x & -u_x \end{pmatrix}, \tag{6.10}$$

where ψ is the angle between the track and the vw-plane, and ϑ is the angle between the track and the uw-plane.

Under these assumptions, the shift of the track intersection point q_x due to a given correction $\delta\mathbf{p}$ can be expressed as

$$\Delta u_x = -\Delta u + \delta \tan\psi + \Delta\gamma\, v_x, \tag{6.11}$$

$$\Delta v_x = -\Delta v + \delta \tan\vartheta - \Delta\gamma\, u_x, \tag{6.12}$$

[34] with $\delta = \Delta w + \Delta\beta\, u_x + \Delta\alpha\, v_x$. Consequently, the dependence of the residuals $\varepsilon(\delta\mathbf{p})$ on the alignment parameters is linear, and the system of equations resulting from Eq. (6.9) is linear as well. Therefore, the solution can be obtained using standard linear solvers, for example the applied *linalg.solve()* from the *numpy* library[36].

The resulting corrections can then be used to transform a cluster's local detector position to a corrected global position. The corresponding coordinate transformation is given by

$$\mathbf{r}_c = (\underline{\mathbf{R}}\,\Delta\underline{\mathbf{R}})^{-1}\mathbf{q} + (\mathbf{r}_0 + \Delta\mathbf{r}), \tag{6.13}$$

where $\mathbf{r}_c$ denotes the corrected global position and $\Delta\mathbf{r}$ is the global counterpart of the local shift $\Delta\mathbf{q}$.

Iterative Procedure To perform the procedure on a full setup, a reference layer is selected, and the corrections are determined with respect to the reference layer. As the approach is track-based, but the track reconstruction relies on the reconstruction of the global positions, the procedure is carried out iteratively. The procedure starts with a track reconstruction step, followed by the determination of the alignment corrections for each layer except the reference layer, as described below, and if selected, a DUT-layer. After the correction is found for each layer, the global cluster positions are recalculated based on the corrected transform, and the track finding algorithm is re-performed based on these new global positions. This procedure is repeated until convergence is achieved. The convergence criteria can either be set to convergence of all correction parameters or on the overall positional shift given by the maximal median change of the tracks' residuals per layer determined via Eq. (6.2.4.2), which is selected as the default due to a higher observed stability. Furthermore, the alignment procedure can be carried out in several stages, where the track-finding algorithm is executed with varying selection criteria (e.g. progressively lower χ^2_r thresholds). This allows one to utilize the enhanced track reconstruction achievable once the misalignment is reduced, thereby improving the quality of the tracks used for the alignment.

DUT Alignment The DUT is excluded from the previous track-based alignment procedure and follows after all alignment steps have been performed. This is done to avoid an artificial

improvement of the performance of this layer by biasing the DUT track residuals. The DUT alignment is performed in the same manner as in the described the layer alignment procedure. However, the tracking is performed under exclusion of the DUT-layer, such that it is performed on the basis of the unbiased DUT track residuals $\varepsilon_{\text{track,DUT}}$.

6.2.5. DUT Sensor Characterization

The following chapter will introduce the spatial resolution σ_{spa} and detection efficiency ε as fundamental figures of merit in silicon pixel sensors and show how the values can be determined in the developed framework. Also, measurements from the February 2025 ITS3 testbeam campaign at ELSA, recorded and analyzed by Iaroslav Panasenko, will represent the reference for the analysis presented in Ch. 7.

6.2.5.1. Spatial Resolution

A typical figure of merit in particle tracking sensors is the sensor's spatial resolution σ_{spa}, which quantifies a sensor's intrinsic ability to reconstruct a traversing particle's position. For sensors with a binary readout like the babyMOSS, this spatial resolution can be approximated by the so-called binary resolution, which is given by

$$\sigma_{bin} = \frac{p}{\sqrt{12}} \tag{6.14}$$

where p denotes the respective pixel pitch of each sensor [3]. This is a theoretical approximation derived under the assumption that the effect of charge sharing can be neglected. For the HUs of the babyMOSS, this would result in binary resolutions of about $\sigma_{bin,tb} = 6.5\,\mu\text{m}$ and $\sigma_{bin,bb} = 5.2\,\mu\text{m}$. Because charge sharing between pixels is present to some degree, the spatial resolution is lower than the binary resolution.This is due to the fact that, if charge is collected from several neighboring pixels, the spatial information is obtained by averaging the positions of all pixels that return a hit due to initial or residual charge movement (cluster). An important parameter to reflect here is not only the amount of occurring charge sharing but also the threshold of the pixels, as the application of clustering is only possible if both pixels return a hit. An exemplary measurement of the dependency of cluster size and the occurring improvement of the spatial resolution in a babyMOSS bb regions can be found in Fig. 6.4. It can be seen how the average cluster size is rising with smaller thresholds and how the quality of the spatial resolution is improving. Also, the spatial resolution can be observed below the binary resolution over the complete range of thresholds measured.
To determine a sensor's actual spatial resolution σ_{spa}, it is assumed that the width of the

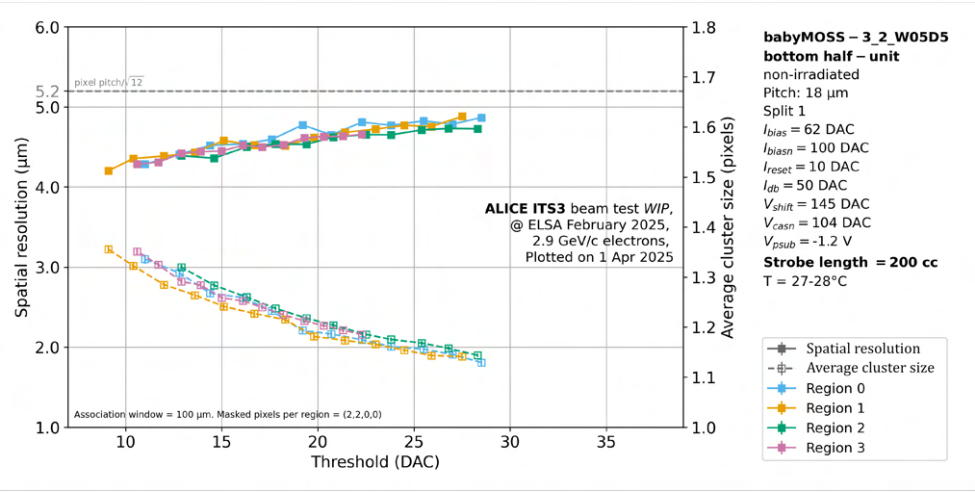


Figure 6.4.: Spatial resolution and average cluster size of babyMOSS-3_2_W05D5 bb. Measured under the given settings on the February 2025 ITS3 testbeam campaign at ELSA. Produced by and featured with the kind permission of Iaroslav Panasenko.

distribution of track residuals $\varepsilon_{\text{track}}$ (see Eq.(6.2)) is composed by

$$\sigma_{res}^2 = \sigma_{spa}^2 + \sigma_{\text{track}}^2 \tag{6.15}$$

with the tracking resolution σ_{track} and the intrinsic sensor resolution σ_{spa}[17]. In other works [23, 24] the tracking resolution is determined via the telescope optimizer tool from Magnus Mager [37]. As this tool assumes advanced trackers for the error propagation and does not allow considering energy distribution and angular distribution like expected for atmospheric muons (see Sec. 5.3.1), this approach does not cover the expected tracking resolution achieved with the setup and track finding procedure at hand. For this work, it is therefore assumed that the tracking resolution σ_{track} denotes the width of the residual distribution between reconstructed track intersections q_{true} and the particle trajectory intersections q_{traj} e.g. the standard deviation of the $\varepsilon_{\text{DUT,traj}}$ distribution that can be obtained by tracking data generated via the simulator described in Sec. 6.2.3. The resulting width is obtained by fitting a Gaussian distribution (see Sec. A.2) to the resulting histogram, taking into account that this is only an approximation of the actual distribution width that results from the multiple scattering in the specific setup. Further σ_{res} denotes the unbiased track residual distributions standard deviation obtained from the measurement data. The spatial resolution in one sensor dimension (u or v) can then be obtained from

$$\sigma_{\text{spa},i} = \sqrt{\sigma_{\text{res},i}^2 - \sigma_{\text{track},i}^2}, \qquad i \in \{u, v\}. \tag{6.16}$$

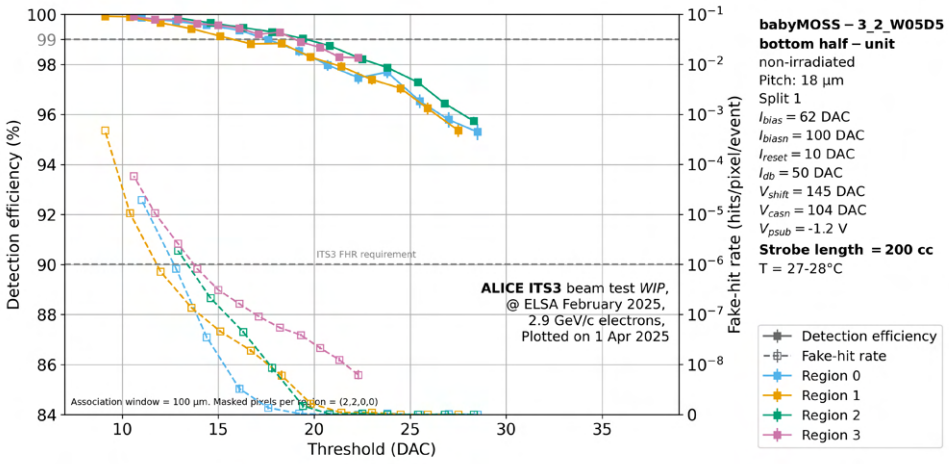


Figure 6.5.: Detection effiency and FHR of babyMOSS-3_2_W05D5 bb. Measured under the given settings on the February 2025 ITS3 testbeam campaign at ELSA. Produced by and featured with the kind permission of Iaroslav Panasenko.

6.2.5.2. Detection Efficiency

The detection efficiency of a pixel detector quantifies its ability to detect a traversing particle. Besides the general charge deposit, this figure is highly dependent on the pixel threshold as the information of present charge depositions is only obtained if the pixel returns a hit signal. An exemplary measurement of the dependency of the detection efficiency in babyMOSS bb regions can be found in Fig. 6.5. It can be seen how the detection efficiency improves with a lower threshold. However, the FHR rises accordingly, indicating the higher level of noise that comes with the lower threshold. In testbeam measurement, the detection efficiency is the fraction of tracks intersecting the DUT that are associated to a cluster within a certain defined area around the track intersection (see Sec. 6.2.2),

$$\epsilon = k/n. \tag{6.17}$$

Here, k is the number of matched clusters and n is the total number of tracks whose extrapolation falls into a DUT region. The association window of the DUT cluster is defined by the maximum allowed track residual $\varepsilon_{DUT,max}$.

7. Results

Having established the experimental setup and analysis framework in the previous chapters, this chapter presents the application and evaluation of the tracking system's performance. In the first section, general parameters that apply to all subsequent analysis sections are defined (see Sec. 7.1). Afterwards, Sec. 7.2 estimates the expected performance and its impact on the track reconstruction for both experimental geometries across different particle momenta.

The subsequent sections form the core of this analysis, applying the described tools to both experimental setups. First, Sec. 7.3 describes the testing of the local tracking system's operability as well as its capability to measure and reconstruct the trajectories of atmospheric muons. Second, an advanced qualitative evaluation of the software framework developed is presented. This is achieved by applying the reconstruction chain to the data recorded during the February 2025 ITS3 testbeam campaign at ELSA. This serves to examine the framework's ability to process experimental data up to the determination of sensor characteristics, such as the spatial resolution and detection efficiency of the DUT (see Sec. 7.4.2).

In both cases, the applied procedures are verified via simulated datasets generated by the simulator module (see Sec. 6.2.3) before being applied to the recorded data. Finally, following a summary of the findings in Sec. 7.5, the chapter closes with an overview of the applied statistical methods, fitting procedures, and uncertainty estimations in Sec. A.5.

7.1. General Parameters for Simulation and Data Processing

In this section, the parameters for track simulations and pipelines for processing real and generated data are briefly summarized. Everything stated in this section applies to all of the following sections of this Chapter if not stated otherwise. In accordance to the Eq. 6.2 and Eq. 6.5 the following definition will be used in the following:

Definition 6. ***Track residual*** ε_{track}*: Distance between the measured position* q_m *and the reconstructed track intersection point* q_x *(see Eq. 6.2).*

Definition 7. ***Trajectory residual*** ε_{traj}*: Distance between the trajectory intersection point* q_{true} *and the reconstructed track intersection point* q_x *(see Eq. 6.5).*

Generation of simulated events Before evaluating the experimental data, artificial data sets are simulated to serve as a baseline for validating the tracking and alignment procedures. The assumed initial geometries of the two setups used for the simulations and the analysis are summarized in Tab. A.3 and Tab. A.4.
For all simulations performed on the local tracking system, the complete set of scattering points described in Sec. 6.2.3 was activated. Unless otherwise stated, a minimum of 3 hit sensor planes is required for track reconstruction. For the angular and momentum distributions, the characteristic atmospheric muon distributions described in Sec. 5.3.1 and Sec. 6.2.3 have been applied.
The beam was centered on the first sensor plane, which was set as the beam spot center μ_{beam}. The simulated ELSA electron beam was modeled with a momentum of $p_{e^-} = 2.9\,\mathrm{GeV/c}$ transverse beam widths of $\sigma_{beam,y} = 4\,\mathrm{mm}$ and a beam divergence of θ_{beam}=5 mrad in a reasonable approximation for the values determined on this basis, despite an asymmetric beam spot being observed in reality, as will be discussed in Sec. 7.4. Here, the protective covers were excluded as scatterers as they were not present during the measurement (see Sec. 7.4). This configuration was used for all subsequent simulated datasets of the ELSA particle beam.

General data processing The generated data from these geometries is processed by multiple steps, starting with defining a ROI in both geometry tables, which was applied for the clustering of the recorded data, as well as in the generation of simulated data. This was done to reduce the effect of multi-scattering caused by the PCB covering the excluded area (see Sec. 6.1). As a next step, the data was processed via the *corryvreckan* `MaskCreator` module, masking pixel exceeding frequencies of 1400 hits/event for bb regions of pixels exceeding 900 Hits/Event for tb regions. The amount of masked pixels per region can be found in Tab. A.3 and Tab. A.4. In the following, the events are passed to the *corryvreckan* `Clustering4D` module, which clusters the data (see Sec. 6.1) and produces the dataset used in the subsequent analysis.

Alignment For the alignment procedure, the uppermost layer (layer 0) is defined as the reference plane. After the pre-alignment, the track-based alignment is carried out in several stages, each using different χ^2_r cuts for track selection and different windows $\varepsilon_{\mathrm{max,DUT}}$ for associating clusters on the DUT. For reasons of efficiency and due to the observed improved stability of convergence, the alignment relies on the mean shift of the residuals (see

Sec. 6.2.4) as its convergence criterion. The specific paramters used for each stage are listed in Tab. A.6 for the local tracking system and in Tab. A.7 for the setup used at ELSA.

7.2. Validation of the Track Reconstruction Algorithm and Expected Performance

To evaluate the performance of the track-finding algorithm (cf. Sec. 6.2.2) and to estimate the achievable spatial resolution of the employed telescope systems (cf. Sec. 5.3) for different type of particles, simulations were performed using muons with different momenta as well the expected distribution of the atmospheric muon energy spectrum (cf. Sec. 6.2.3). In addition, an electron beam with momentum $p_{e^-} = 2.9\,\mathrm{GeV/c}$ was simulated. The track-finding algorithm was then applied to all generated events. As a figure of merit for the track reconstruction quality, the root mean square (**R**oot **M**ean **S**quare (RMS)) (see Eq.(A.8)) of the trajectory residuals $\varepsilon_{\mathrm{traj}}$ at all sensor intersections was determined for each dataset. For every configuration, a total of $N_{events} = 1 \cdot 10^5$ was generated. To account for the fact that the two HUs feature different pixel pitches, only tracks traversing the same HU in all layers were selected for the performance evaluation.

The peaks of the corresponding residual distributions were fitted with an inverse parabolic function (see Sec. A.4) to obtain an estimator of the maximum peak position. The results for the local tracking system are presented in Fig. 7.1. The data demonstrates that the distributions broaden with a lower muon momentum, while the maxima of the corresponding distributions shift towards larger residuals. For higher muon momenta, the distributions are centered close to the binary resolution (cf. Sec. 6.2.5.1) of the respective HU, whereas for low-energy muons, the centers of the distributions are shifted to residual values. Consequently, the distributions maxima for atmospheric muons lie above the respective binary resolutions σ_{bin}, with $x_{\mathrm{RMS,max,tb}} = (7.98 \pm 0.13)\,\mu\mathrm{m}$ and $x_{\mathrm{RMS,max,bb}} = (5.87 \pm 0.08)\,\mu\mathrm{m}$.

The observed difference between the tb and bb values of x_{RMS} exceeds what would be expected from the nominal difference in spatial resolution alone. This discrepancy can be attributed to the defective region 1 in layer 1 of the tb, which effectively removes one measurement point for tracks passing through that area. The resulting increase in the fraction of tracks reconstructed with only three rather than four clusters reduces the precision of track reconstruction.

It is further noteworthy that, for the simulated electron beam, the maxima of the residual distributions are also located above the binary resolution (cf. Sec. 6.2.5.1) of the HUs, with $x_{\mathrm{RMS,max,tb}} = (6.78 \pm 0.34)\,\mu\mathrm{m}$ and $x_{\mathrm{RMS,max,bb}} = (5.34 \pm 0.13)\,\mu\mathrm{m}$. This estimation from

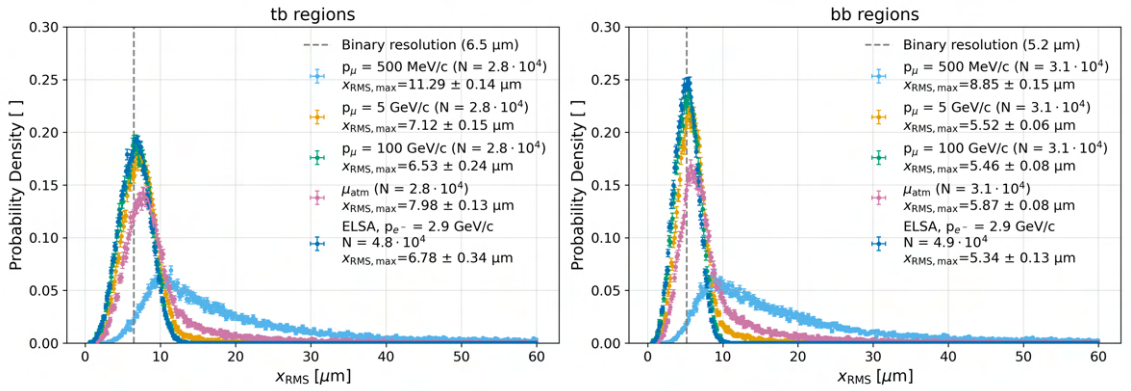


Figure 7.1.: Probability density (see Eq. A.11) of RMS of $|\varepsilon_{\text{traj}}|$ x_{RMS} for all layers hit along a reconstructed track for data simulated in the local tracking system. $x_{\text{RMS,max}}$ is approximated via an inverse parabola fit of the maximum data points.

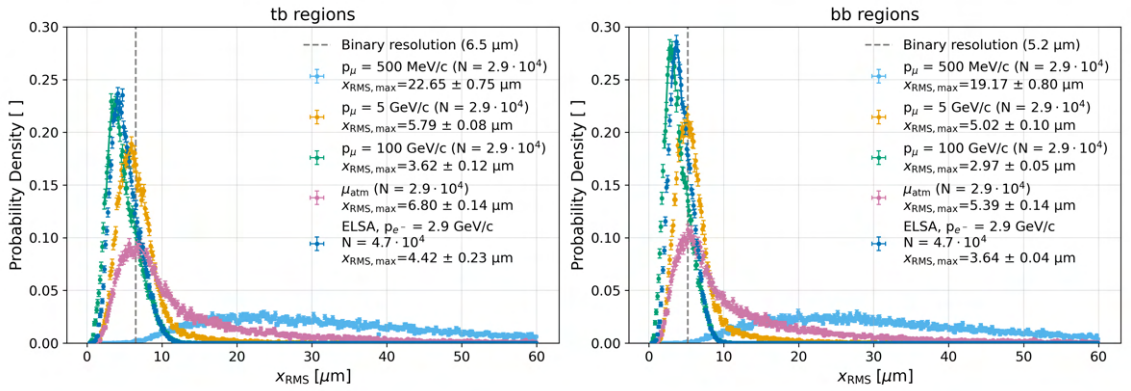


Figure 7.2.: Probability density (see Eq. A.11) of RMS of $|\varepsilon_{\text{traj}}|$ x_{RMS} for all layers hit along a reconstructed track for data simulated in the setup used at ELSA. $x_{\text{RMS,max}}$ is approximated via an inverse parabola fit of the maximum data points.

the simulated tracks indicates that, even when simulating controlled testbeam conditions, the average track reconstruction quality achievable with the present detector configuration and reconstruction algorithm does not surpass the intrinsic spatial resolution of a single sensor unit. This imposes significant constraints, and potentially fundamental limitations, on commonly employed sensor characterization techniques.

The simulation results obtained with the geometry of the telescope used for the test beam at ELSA are shown in Fig. 7.2. It is immediately apparent that, for low-energetic muons ($p_\mu = 500\,\text{MeV/c}$), the x_{RMS} distribution is broadened and the maximum is shifted to larger residuals compared to the distribution presented in Fig. 7.1. This behavior can

be attributed to the increased lever arm of the telescope: the distance between the first and the last layer of the ELSA test beam telescope is $l_{\mathrm{ELSA}} \approx 150\,\mathrm{mm}$, in contrast to $l_{\mathrm{local}} \approx 80.93\,\mathrm{mm}$ for the local tracking system. The longer lever arm enhances the effect of multiple scattering on the telescope's transverse deviations.

It is also noteworthy that, although the angular acceptance of the longer telescope and the intrinsic track-reconstruction precision are improved due to the larger number of sensor planes, the peaks of the x_{RMS} distributions obtained with atmospheric muons still lie above the binary resolution of the corresponding HU, with $x_{RMS,\mathrm{max},tb} = (6.80 \pm 0.14)\,\mu\mathrm{m}$ and $x_{RMS,\mathrm{max},bb} = (5.39 \pm 0.14)\,\mu\mathrm{m}$. In contrast, for the simulated ELSA beam, the majority of reconstructed tracks exhibit x_{RMS} values below the binary resolution (cf. Sec. 6.2.5.1) of the respective HU, with peaks at $x_{RMS,\mathrm{max},tb} = (4.42 \pm 0.23)\,\mu\mathrm{m}$ and $x_{RMS,\mathrm{max},bb} = (3.64 \pm 0.04)\,\mu\mathrm{m}$. The same qualitative behavior is observed for high-energy atmospheric muons.

Overall, these results demonstrate that the track-reconstruction algorithm can reproduce particle trajectories with satisfactory accuracy for simulated particles that undergo little multiple scattering. The observed shapes of the x_{RMS} distributions can be qualitatively understood as a consequence of the telescope geometry and the particle momentum. Lower particle momenta, which are associated with a higher probability of strong multiple scattering, lead to a broadening and an upward shift of the x_{RMS} distributions, whereas an increased number of points of measurement improves the track-reconstruction precision.

However, it must be considered that, for the local tracking system, an RMS deviation between the reconstructed track and the true trajectory exceeding the binary resolution of the corresponding HU imposes limitations on sensor-performance studies, such as spatial-resolution measurements. In such analyses, the achievable track-reconstruction resolution is further degraded because one sensor plane must be excluded from the track-reconstruction procedure to serve as the DUT. Further investigation of the achievable tracking resolution on the DUT will follow in Sec. 7.3.1.2 for the local tracking system and in Sec. 7.4.1.2 for the ELSA setup.

7.3. Local Tracking System

This chapter shows the evaluation of the framework developed in Ch. 6 and the results of its application to the data recorded by the local tracking system described in Sec. 6.2. The investigation is performed in two complementary sections. The first one is dedicated to validating the framework using simulated atmospheric muon datasets to verify the alignment procedure under controlled conditions, using datasets with a high number of reconstructible

tracks. Also, the track reconstruction resolution σ_{track} achievable on the DUT-layer will be determined. The second section 7.3.2 will apply the same alignment procedure to the atmospheric muon dataset obtained from a measurement with the local tracking system. Afterwards, it will compare the general properties of the reconstructed data to the simulated data, followed by attempting the determination of the DUT-layers detection efficiency ϵ and the spatial resolution $\sigma_{spatial}$.

7.3.1. Simulations

This section will first evaluate the accuracy of the alignment procedure introduced in Sec. 6.2.4 when applied to the local tracking system with simulated atmospheric muon datasets for one misaligned layer and a fully misaligned telescope in Sec. 7.3.1.1. Afterwards, the DUT-layer tracking resolution σ_{track} will be determined via simulated datasets.

7.3.1.1. Alignment

The alignment procedure is verified by artificially misaligning one or more telescope layers in the initial geometry (see Tab. A.3) by applying the transformations $\Delta R_{mis,layer}$ and $r_{0,mis,layer}$. This emulates the effect of a physical misalignment of the telescope and mimics the real geometry of the setup.
A simulation is then performed based on this modified geometry to generate the corresponding dataset. Since only the local position within a sensor is obtained in a real measurement, the local sensor position of each simulated cluster is retained and re-expressed in the global frame using the unperturbed initial geometry. This reproduces the situation in real data with a misaligned setup, where the true geometry is unknown, and the assumed geometry is used for reconstruction.
The introduced misalignment manifests itself in the track residuals as described in Sec. 6.2.4. The dataset prepared in this way is then processed by the alignment procedure, again starting from the original, unperturbed geometry.
The principal figures of merit are:

1. The deviation between the recovered alignment corrections, $\Delta R_{\text{align,layer}}$ and $r_{0,\text{align,layer}}$ (or equivalently the underlying parameter set $(x_0, y_0, z_0, \alpha, \beta, \gamma)$), and the true misalignment parameters
2. The discrepancy between the measured cluster positions r_m and the trajectory intersection positions r_{traj} resembled in the trajectory residual $\varepsilon_{\text{traj}}$
3. The degree of misalignment remaining in the track residuals $\varepsilon_{\text{track}}$ when plotted

against the track intersection point q_x or in the width and offset off the track residuals $\varepsilon_{\text{track}}$ distribution.

Point 3 represents a commonly employed figure of merit for the performance of an alignment procedure for a real dataset. It tests the offset and slope of the track residuals $\varepsilon_{\text{DUT},x/y}$ as a function of the corresponding track intersection coordinates on the u and v axes. For an ideally aligned planar sensor without residual offsets, these residuals would be distributed symmetrically around the zero line (or follow the spatial distribution of the incident particles) without a systematic dependence on position.
It should be noted that fluctuations in the achieved alignment precision are observed between different simulated datasets. This behavior can be attributed to the random component in the data generation process, but it also indicates that the expected performance of the alignment procedure cannot be fully characterized by the exemplary evaluations presented below.

Single Layer For the single-layer alignment study, only the second sensor (layer 1) of the initial telescope configuration was intentionally misaligned. For this part, no DUT was defined; consequently, the track-finding algorithm used all four telescope layers for track reconstruction. The individual stages of the alignment procedure are summarized in A.6.
For the alignment procedure, a total of $1 \cdot 10^5$ simulated muon events with a momentum of $p_\mu = 3\,\text{GeV/c}$ were generated, following the angular distribution described in Sec. 5.3.1. The incremental evolution of the cumulative alignment corrections is shown in Fig. 7.3. The results indicate that the pre-alignment step already recovers the in-plane translations in u and v to a good approximation, even though an additional shift in w and a tilt were applied. Beyond this stage, the residual discrepancies in all alignment parameters are rapidly reduced until the curves reach a plateau, at which point the convergence criterion is fulfilled. A notable remaining deviation is observed for the parameters α and w, with residual offsets of $\alpha_{\text{dif}} \approx 0.23\,\text{mrad}$ and $w_{\text{dif}} \approx 0.23\,\mu\text{m}$. In contrast, the remaining deviations of the other parameters lie clearly in the sub-micron or sub-mrad range, namely $u_{\text{dif}} \approx 0.014\,\mu\text{m}$, $v_{\text{dif}} \approx -0.016\,\mu\text{m}$, $\beta_{\text{dif}} \approx -0.011\,\text{mrad}$, and $\gamma_{\text{dif}} \approx 0.01\,\text{mrad}$. The results of track residual ε_{track} plotted against the track intersection q_x can be found in Fig. 7.4. Despite the small residual misalignment, a clear tendency towards close to zero offset and rotations can be derived from the applied linear fits of the plots described with values of $m_u = (-0.0055 \pm 0.0046)\,\mu\text{m/mm}$ and $m_v = (0.009 \pm 0.018)\,\mu\text{m/mm}$, and offsets of $u_0 = (0.011 \pm 0.033)\,\mu\text{m}$ and $v_0 = (-0.007 \pm 0.034)\,\mu\text{m}$ that contain the zero point within their range of uncertainty excpet for a small deviation of the slope in the u-dimension m_u.

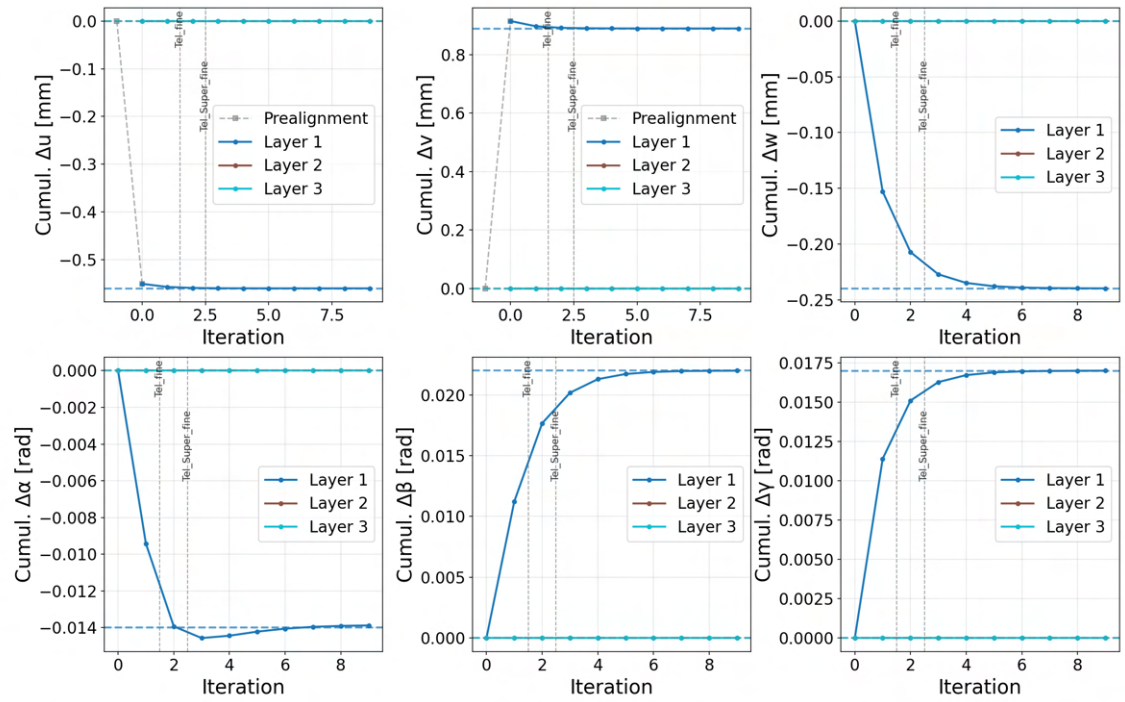


Figure 7.3.: Incremental evolution of the alignment parameters for the alignment of a single layer using $1 \cdot 10^5$ simulated muon events with $p_\mu = 3\,\mathrm{GeV/c}$. The horizontal dotted lines indicate the true misalignment parameters defining $\Delta R_{\mathrm{mis,layer}}$ and $r_{0,\mathrm{mis,layer}}$. The vertical grey dotted lines mark the boundaries between the individual alignment stages. Layer 0 serves as the reference layer for the alignment.

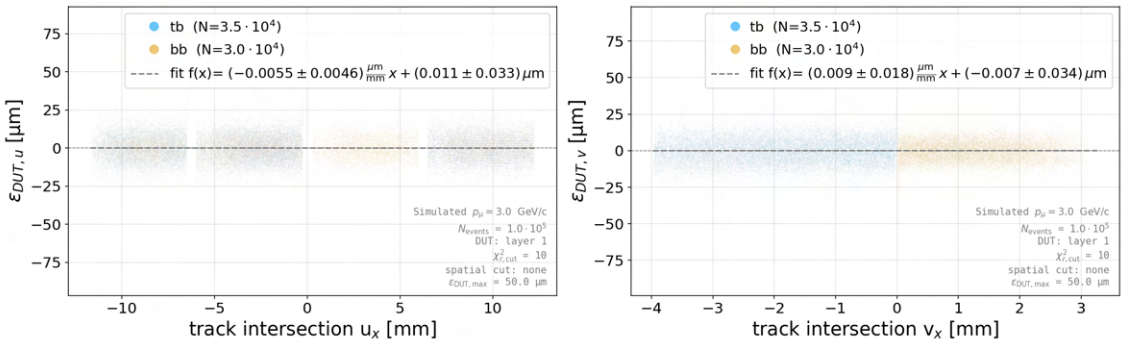


Figure 7.4.: DUT residual ε_{DUT} of track intersection q_m and simulated measured position q_x plotted against the point of track intersection q_m in the respective dimension after the alignment of a single layer. Obtained using $1 \cdot 10^5$ simulated muon events with $p_\mu = 3\,\mathrm{GeV/c}$.

Multiple Layers As the number of free parameters is substantially larger in a realistic alignment scenario, in which all layers may be misaligned, the resulting alignment procedure is considerably more prone to inaccuracies and deviations. As a test of this case, all three non-reference planes have been misaligned when generating the test data set. For the results shown in Fig. 7.5, $1 \cdot 10^5$ atmospheric muon events were simulated using the misaligned geometry. Sensor layer 1 was reselected as DUT, implying that the alignment of the reference layers and layer 1 is performed independently (see Sec. 6.2.4), and that the track-finding algorithm does not consider clusters from layer 1 (see Sec. 6.2.2). It can be

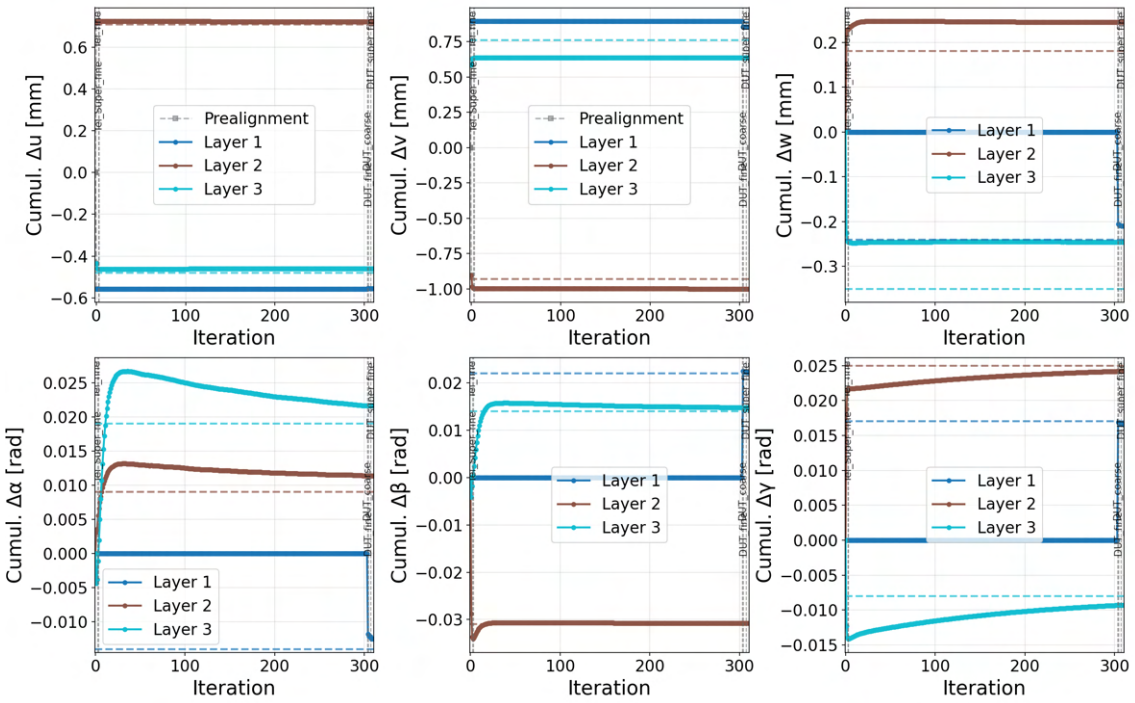


Figure 7.5.: Incremental evolution of the alignment parameters for the alignment of the local tracking system using $1 \cdot 10^5$ simulated atmospheric muon events. The horizontal dotted lines indicate the true misalignment parameters defining $\Delta R_{\text{mis,layer}}$ and $r_{0,\text{mis,layer}}$. The vertical grey dotted lines mark the boundaries between the individual alignment stages. Layer 0 serves as the reference layer for the alignment. Note that the DUT alignment can be observed on the edge within the last iterations.

clearly seen that, although the discrepancy between the alignment parameters decreases, the parameters do not converge to the initially imposed misalignment. Nevertheless, the procedure converges given the higher final stage convergence criteria presented in Tab. A.6 and terminates successfully.

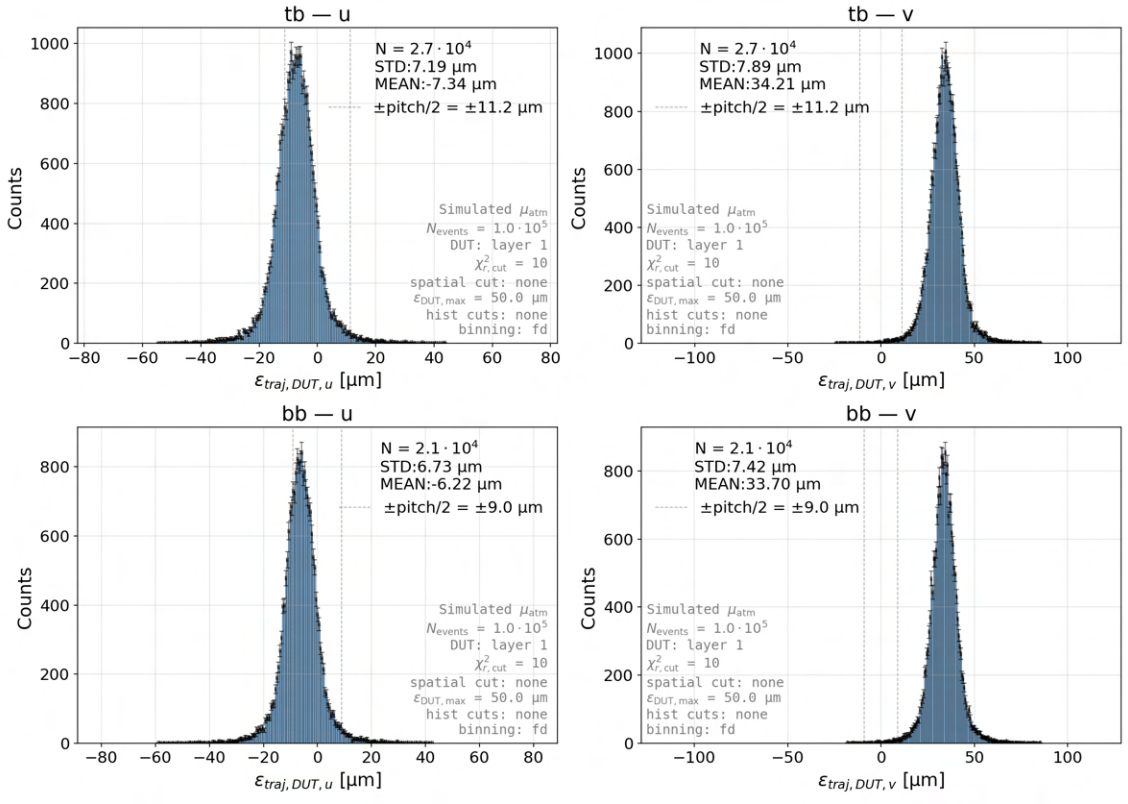


Figure 7.6.: Unbiased residuals $\varepsilon_{\mathrm{DUT,traj}}$ between the simulated intersection point within the layer and the reconstructed track in local detector coordinates for the two HUs after the alignment of all three non-reference planes, obtained using $1 \cdot 10^5$ simulated atmospheric muon events.

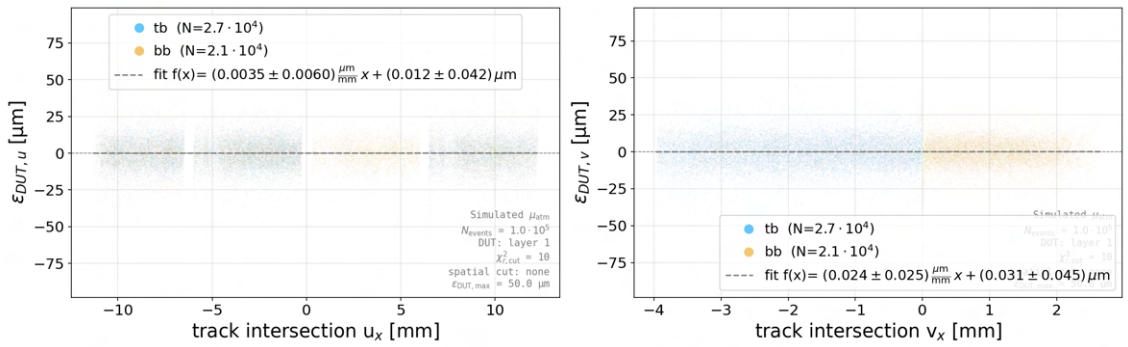


Figure 7.7.: DUT residual ε_{DUT} of track intersection q_m and simulated measured position q_x plotted against the point of track intersection q_m in the respective dimension for the alignment of the local tracking system using $1 \cdot 10^5$ simulated atmospheric muon events.

This behavior can be attributed to the fact that the solution of the global alignment system is not uniquely constrained by the available information (e.g., the reconstructed tracks). The impact of this residual inaccuracy is also visible in the trajectory residuals between the reconstructed track intersection and the simulated trajectory intersection on the DUT-layer, $\varepsilon_{\mathrm{DUT,traj}}$. The corresponding distributions are shown in Fig. 7.6. The residual distributions exhibit a non-zero mean, indicating a discrepancy between the reconstructed global impact position $q_{x,\mathrm{DUT}}$ and the true simulated track intersection $q_{\mathrm{traj,\ DUT}}$. The effect is observed to be systematically higher in v-regime, which possibly can be attributed to a smaller lever arm of the incident simulated muons, resulting from the reduced size of the sensor in that dimension, which limits the alignment procedures capability of recovering z- as well as rotational-misalignments.

As shown in Fig. 7.7, the measured distributions approach these criteria, yielding slopes of $m_u = (-0.0035 \pm 0.0060)\,\mu\mathrm{m/mm}$ and $m_v = (0.024 \pm 0.025)\,\mu\mathrm{m/mm}$, and offsets of $u_0 = (-0.012 \pm 0.042)\,\mu\mathrm{m}$ and $v_0 = (-0.031 \pm 0.045)\,\mu\mathrm{m}$, all of which are close to zero within uncertainties. This demonstrates that, although the originally imposed misalignment was not determined, a transformation that minimizes the track residuals $\varepsilon_{\mathrm{DUT}}$ to within a certain approximation was found, even though the initial misalignment was not correctly reconstructed.

7.3.1.2. DUT Tracking Resolution

As described in Sec. 6.2.5.1, the tracking resolution σ_{track} of the DUT sensor is determined by the deviation of the actual trajectory intersection point q_{true} and the reconstructed track intersection point q_x. To determine the tracking resolution σ_{track} itself, the width of the residuals distribution is measured for simulated data.
To estimate the tracking resolution on the local tracking system, atmospheric muon events have been generated, and the track-finding algorithm has been applied. As discussed, the number of available tracks is comparatively low, which requires careful cut selection. To determine these, a χ^2_r of $\chi^2_{r,cut} = 10$ and $\chi^2_{r,cut} = 2.5$ have been applied, both with no restrictions on the DUT-cluster association. For the resulting track, the trajectory residual $\varepsilon_{\mathrm{DUT,traj}}$ is collected. The resulting residual distributions can be found in Fig. 7.8 for the more coarse $\chi^2_{r,cut} = 10$. The distributions were fitted with a Gaussian distribution (see Sec. A.2). The resulting tracking resolution σ_{track} are $\sigma_{\mathrm{track,tb,u}} = (6.477 \pm 0.022)\,\mu\mathrm{m}$, $\sigma_{\mathrm{track,tb,v}} = (6.622 \pm 0.024)\,\mu\mathrm{m}$, $\sigma_{\mathrm{track,bb,u}} = (5.696 \pm 0.020)\,\mu\mathrm{m}$ and $\sigma_{\mathrm{track,bb,v}} = (5.860 \pm 0.022)\,\mu\mathrm{m}$ all which are unambiguously below the binary resolution of the respective HU. One of the main contributors to this effect is the low-energy muons (see Sec. 7.2) that are associated with higher tracking resolution due to multiple scattering. Hence the tracking

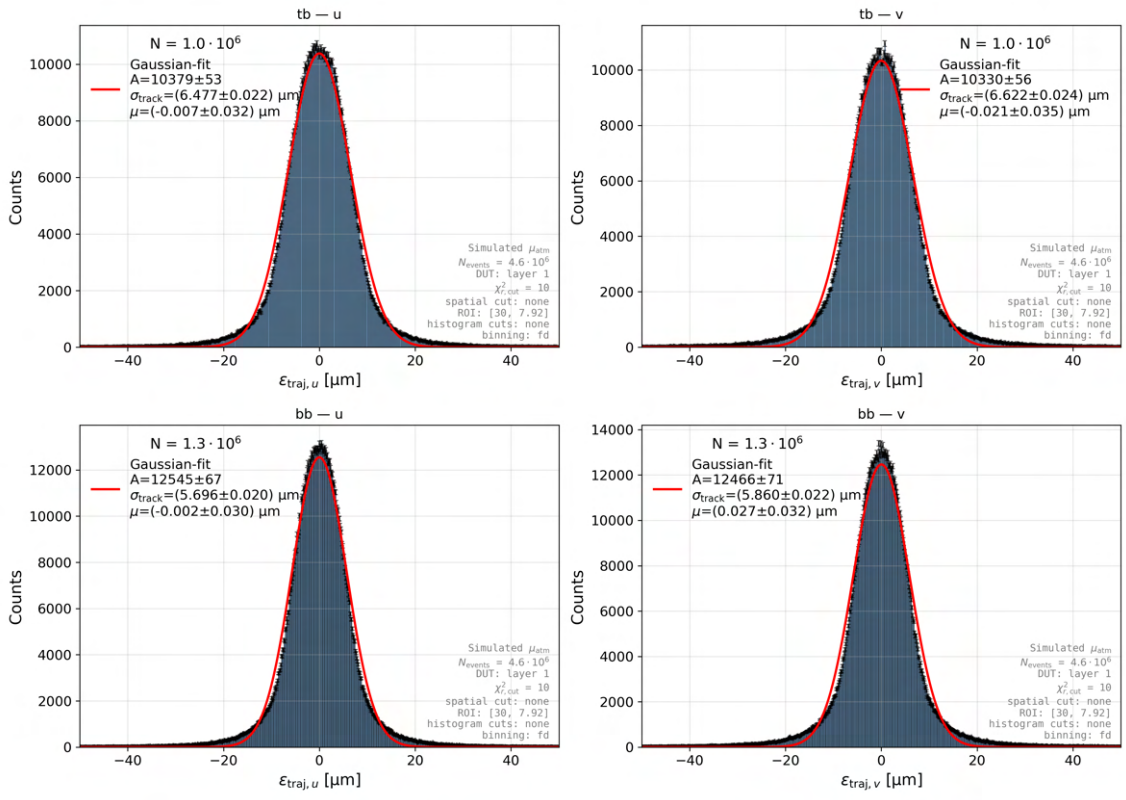


Figure 7.8.: Unbiased trajectory residuals $\varepsilon_{\mathrm{DUT,traj}}$ between the simulated intersection point within the layer and the reconstructed track in local detector coordinates for the two HUs. For the track reconstruction $\chi^2_{r,cut}$= 10 was set. To estimate the respective tracking resolution, a Gaussian fit was applied.

resolution increased by lowering the χ^2_r cut to 2.5. The resulting distributions of $\varepsilon_{\mathrm{DUT,traj}}$ under application of this cut can be found in Fig. 7.9. The determined tracking resolution σ_{track} is lowered to $\sigma_{\mathrm{track,tb,u}} = (5.845 \pm 0.022)\,\mu\mathrm{m}$, $\sigma_{\mathrm{track,tb,v}} = (5.971 \pm 0.020)\,\mu\mathrm{m}$, $\sigma_{\mathrm{track,bb,u}} = (5.088 \pm 0.016)\,\mu\mathrm{m}$ and $\sigma_{\mathrm{track,bb,v}} = (5.185 \pm 0.027)\,\mu\mathrm{m}$ all of which lie below the binary resolution of the respective HU. However, it must be noted that the applied cuts further reduce the available tracks, and even with this spatial cut, the achieved spatial resolution does not exceed that observed in other measurements; see Fig. 6.4.

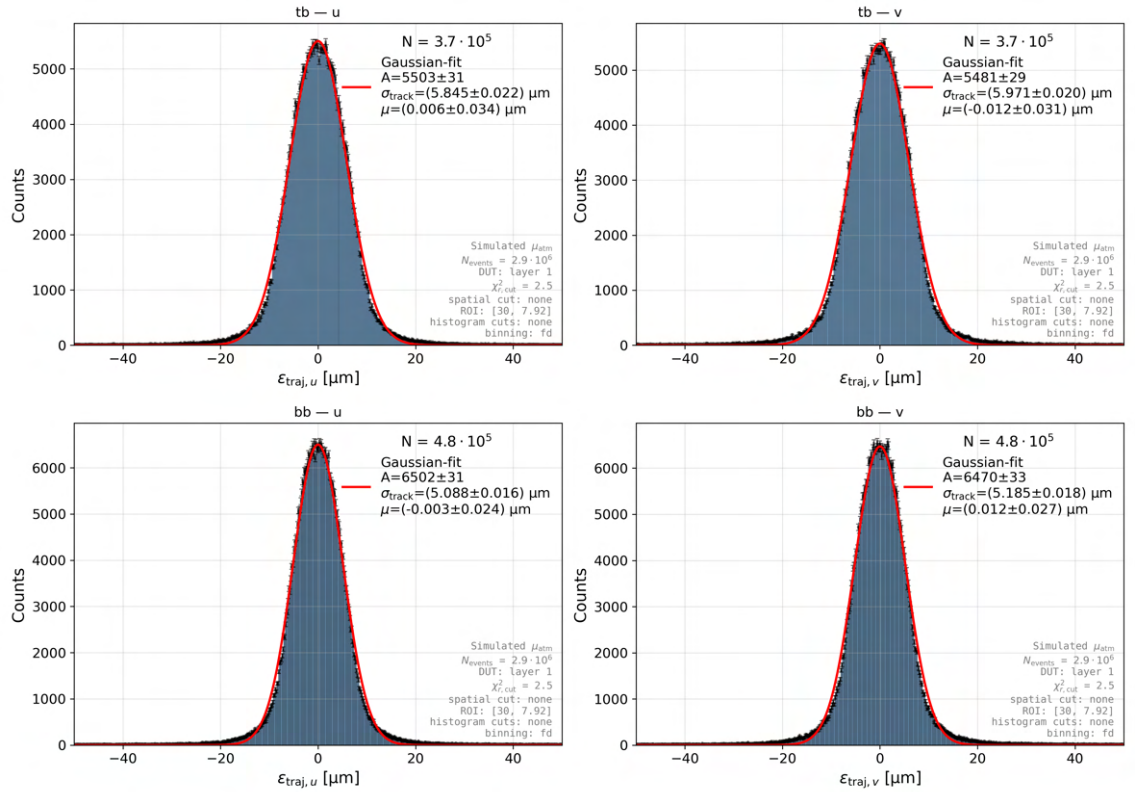


Figure 7.9.: Unbiased trajectory residuals $\varepsilon_{\mathrm{DUT,traj}}$ between the simulated intersection point within the layer and the reconstructed track in local detector coordinates for the two HUs. For the track reconstruction $\chi^2_{r,cut}$= 2.5 was set. To estimate the respective tracking resolution, a Gaussian fit was applied.

7.3.2. Data Analysis

For the collection of atmospheric muon events, the local tracking system described in Sec. 5.3 was operated following the Front-end settings set 2 (see Tab. 5.1) that have been proven best by previous adjustment runs and the THR- and FHR-scans (see Sec. 5.3.3). The VCASB value has been adjusted as high as possible without overshooting a FHR of $10^{-6}\,\frac{\text{hits}}{\text{pixel}\cdot\text{event}}$ to maintain a high detection efficiency while also keeping the FHR as low as possible. The respective value for each region can be found in Tab. A.5 and the corresponding FHR and THR values can be derived from the plots presented in Sec. D. Effectively, this results in a broad range of the region **Thr**esholds (THRs) ranging from 15 to 25 DAC (see Sec. 5.3.3 and Sec. D).

For the measurement of atmospheric muons both PMTs were tuned such that $f_{1,\mathrm{Sci}} = (90.2 \pm 4.7)\,\mathrm{mHz}$ (see Eq. (A.12)) is matched in good approximation. For the final measurement, the PMTs have been connected to the trigger logic board (see Sec. A.3) and operated in coincidental trigger mode.

7.3.2.1. Rates

To estimate the expected number of recorded events, a total of $N_{1,\mathrm{Sci}} = 2.1 \cdot 10^6$ atmospheric muons were simulated on the upper scintillator in order to determine the success rates of the individual selection stages, namely the requirement of a coincident hit on both scintillators and the probability of a particle traversing at least one sensor layer. The detailed calculations are given in Sec. A.3.
The telescope was operated for about 22 days ($t = 1\,907\,152.938\,\mathrm{s}$), during which $N_{\mathrm{trg}} = 3954$ triggers were recorded, corresponding to a trigger rate of $f_{\mathrm{trg}} = (2.073 \pm 0.033)\,\mathrm{mHz}$. Of these, $N_{\mathrm{acc}} = 1950$ events contain at least one cluster after masking, clustering, and cluster reading, corresponding to a trigger acceptance of $R_{\mathrm{trg}} = (49.32 \pm 0.80)\,\%$, in good agreement with the simulated value of $R_{\mathrm{trg,Sim}} = (51.361 \pm 0.087)\,\%$. The two differ by slightly more than their uncertainties, which may be attributed to a residual misalignment between the scintillators and the telescope. This overall agreement indicates that, once a coincidence trigger has been issued, the relative geometry of the sensor layers and the scintillators is well reproduced by the assumed setup geometry.
A far stronger deviation, however, is observed in the absolute rate of accepted events. In the simulation, a fraction $R_{\mathrm{Acc,Sim}} = (5.011 \pm 0.011)\,\%$ of the atmospheric muons traversing the first scintillator produces at least one hit layer. Together with the expected single-scintillator rate $f_{1,\mathrm{Sci}} = (90.2 \pm 4.7)\,\mathrm{mHz}$, this corresponds to an expected accepted-event rate of $f_{\mathrm{acc,exp}} = (4.50 \pm 0.23)\,\mathrm{mHz}$. The measured rate, $f_{\mathrm{min}} = (1.022 \pm 0.023)\,\mathrm{mHz}$, is lower by roughly a factor of four.
The origin of this deviation cannot be fully resolved, but it can be localized. Since the single-scintillator PMT rate was tuned to the expected value $f_{1,\mathrm{Sci}}$ and the two trigger acceptances R_{trg} and $R_{\mathrm{trg,Sim}}$ agree in approximation, neither the single-scintillator rate nor the trigger acceptance can account for a discrepancy of this magnitude. It should be noted, that R_{trg} does not rule out noise as a source of single-layer events. As shown in Sec. 7.3.2.3, the fraction of such events exceeds the simulated expectation. A definitive identification of the cause is therefore not possible, but the available results make it reasonable to localize it in the coincidence measurement. Candidate contributions include the relative misalignment, spacing, and effective overlap of the two scintillators, a possibly overly optimistic modeling of the coincidence acceptance in the simulation, and noise in the recorded data.

Disentangling these contributions is beyond the scope of this work.
It should nevertheless be emphasized that this deviation does not invalidate the analyses presented below: these are conditioned on successfully reconstructed tracks and are therefore independent of the absolute normalization. It does, however, reduce the number of well-reconstructable atmospheric muon tracks available.

7.3.2.2. Alignnment

For aligning the local tracking system using the recorded data, the same alignment stages as those used for the simulations have been applied. However, since the incremental shifts begin

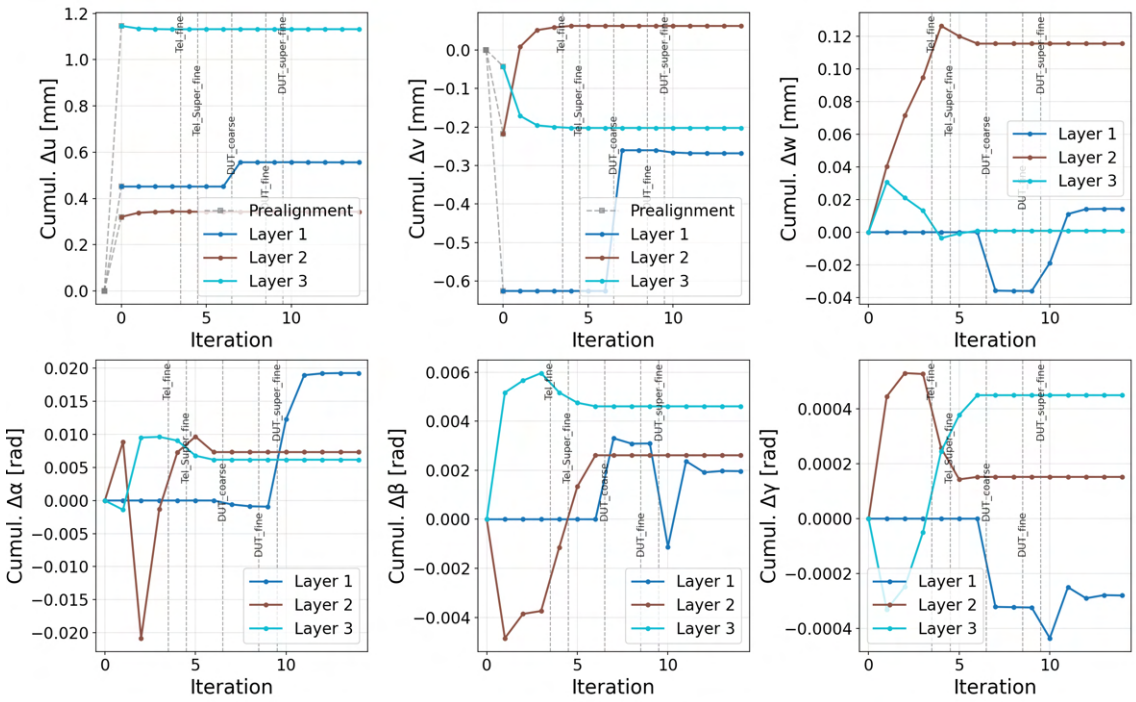


Figure 7.10.: Incremental evolution of the alignment parameters for the alignment of the local tracking system with the recorded events. The vertical grey dotted lines mark the boundaries between the individual alignment stages. Layer 0 serves as the reference layer for the alignment.

to converge towards angular corrections that are nonphysical for the given mechanical and operational conditions of the setup (see Fig. A.9) and simultaneously induce an increased rotational misalignment in the final residuals compared with the results presented here (see Fig. A.8), the convergence criteria have been lowered (see Tab. A.6 B) in the final stages of both the reference-plane and the DUT alignment. This modification interrupts the nonphysical angular correction drift once the mean shifts of the measured DUT cluster positions,

$\overline{\Delta u_x}$ and $\overline{\Delta v_x}$, fall below 0.01 µm. A plausible explanation for the pronounced drift observed at higher convergence thresholds is the combination of (i) an actual genuinely increased tilt of individual sensor layers, (ii) the limited number of tracks, which provides weak constraints for the alignment parameters, and (iii) residual noise present in the dataset. Nevertheless,

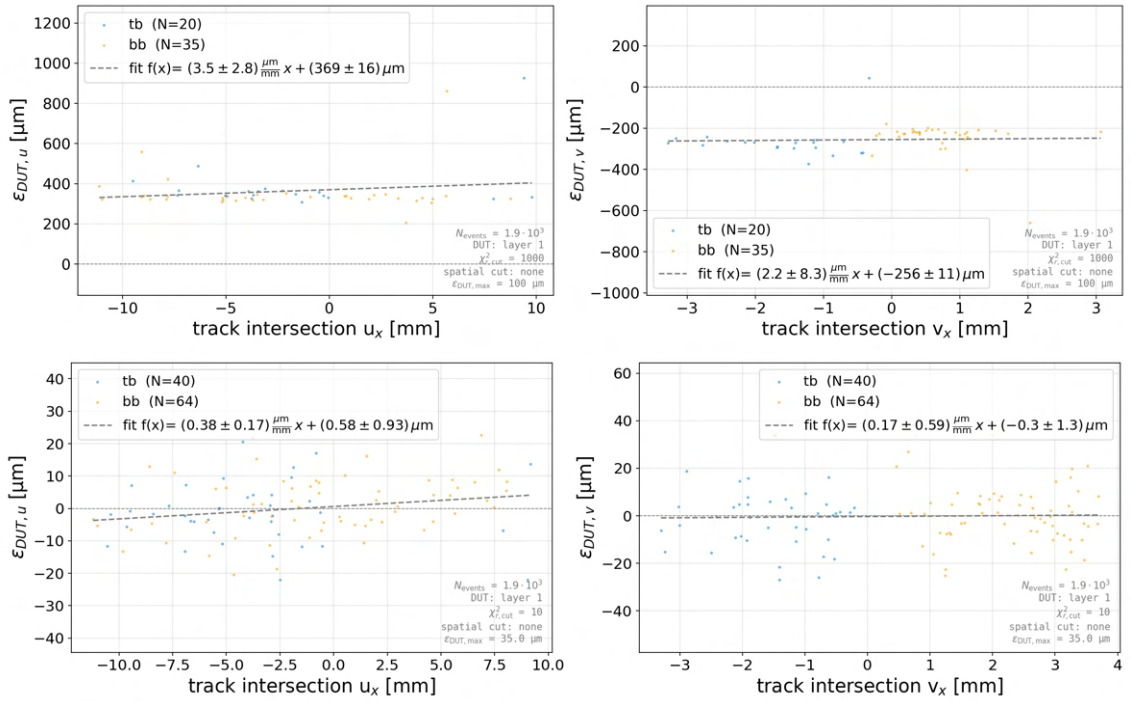


Figure 7.11.: DUT residual ε_{DUT} of track intersection q_m and measured position q_x plotted against the point of track intersection q_m in the respective dimension before (top) and after (bottom) the alignment of the atmospheric muon data. The residuals from the unaligned dataset were determined using the track reconstruction specifications of the first alignment stage. Note the change of the y-scale from top to bottom

it should be emphasized that this behavior does not occur in smaller exemplary simulated datasets with a comparable number of events ($N_{\text{events}} = 300$). Hence, the low number of available tracks alone cannot account for the observed effect. An illustrative example of the alignment procedure applied to such a small simulated dataset is provided in the appendix, where both a parameter evolution plot and a residuals-versus-track-intersection plot are shown in Fig. A.10 and Fig. A.11, respectively. To properly account for the influence of noise, and in order neither to artificially increase the measured detection efficiency nor to unduly narrow the distribution of the track residuals ε_{DUT}, the association window for DUT clusters is restricted to $\varepsilon_{\text{max,DUT}} = 35\,\text{µm}$ around the extrapolated track intersection point q_x on the corresponding sensor plane. This window is applied both in the final align-

ment stage and in the subsequent track-reconstruction procedure used to determine the residual distributions. The outcome of the iterative alignment procedure for the recorded data is shown in Fig. 7.10. Compared with the alignment based on simulated datasets (see Sec. 7.3.1.1), the alignment process is considerably less stable. Several parameters do not converge monotonically towards a well-defined value over all iterations; instead, they exhibit sign changes in successive iteration steps or even in the cumulative effect (e.g. cumul. $\Delta\alpha$ of layer 2). This behavior can be attributed to the changing subsets of tracks that satisfy the selection criteria of the track-reconstruction algorithm as the alignment updates proceed, which in turn alter the constraints available for the layer-alignment step. The results for the data and the corresponding alignment performance are shown in Fig. 7.11. For the estimation of the residuals, a selection cut of $\chi^2_{\mathrm{r,cut}} = 10$ was applied. As only 40 associated clusters in the tb HU region and 64 in the bb region fulfill this requirement, the subsequent analysis of the residuals is restricted to a comparison between the respective HUs and no to the different regions of the DUT. Although the linear fits applied to the dataset exhibit

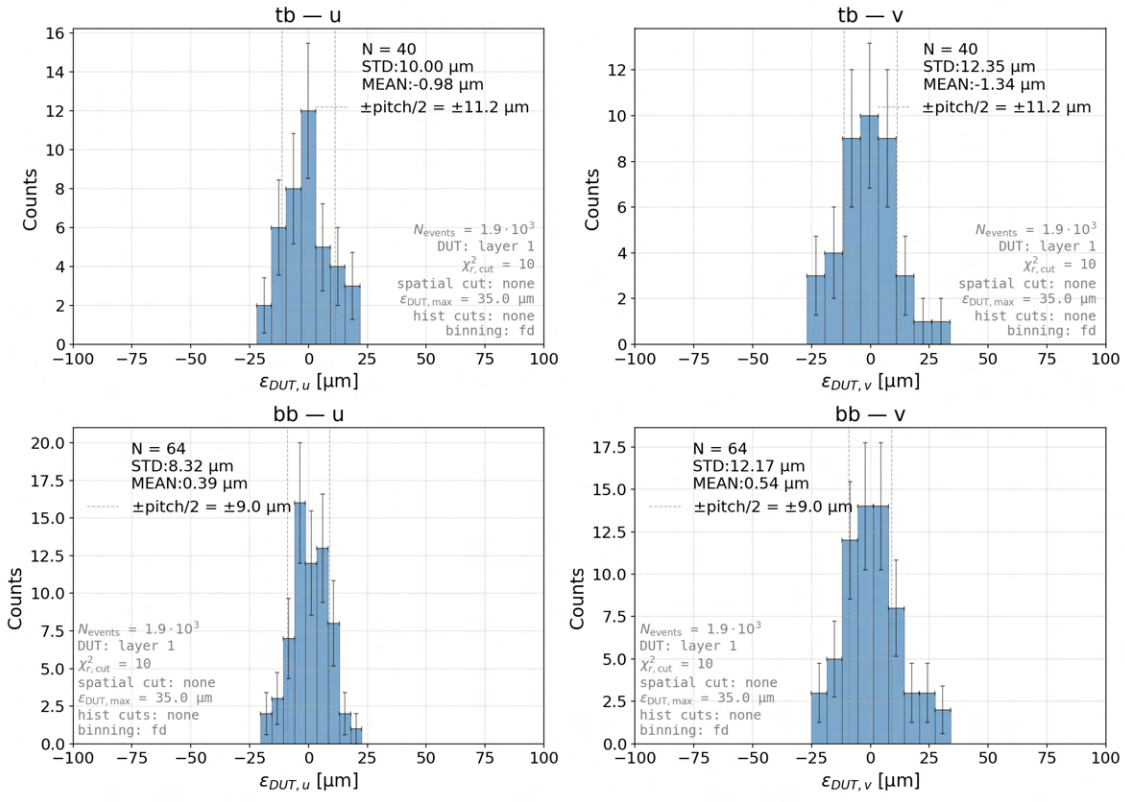


Figure 7.12.: Unbiased track residuals $\varepsilon_{\mathrm{DUT,track}}$ between the measured intersection point within the layer and the reconstructed track in local detector coordinates for the two HUs.

small slopes of $m_u = (0.38 \pm 0.17)\,\mu m/mm$ and $m_v = (0.17 \pm 0.59)\,\mu m/mm$, and offsets of $u_0 = (-0.58 \pm 0.93)\,\mu m$ and $v_0 = (-0.3 \pm 1.3)\,\mu m$, the large uncertainties associated with these fit parameters, together with the visible systematic deviations of the residuals, indicate that the alignment procedure does not fully compensate for the displacement and rotation of the sensor layers, especially considering the high uncertainties in the v-regime. This also reflects itself in the DUT track residual distributions $\varepsilon_{\mathrm{DUT}}$ are shown as histograms in Fig. 7.12. Here, the statistical standard deviations of the distributions in the v-direction, $\mathrm{STD}_{\mathrm{tb},v} = 12.35\,\mu m$ and $\mathrm{STD}_{\mathrm{bb},v} = 12.17\,\mu m$, are noticeably larger than the corresponding standard deviations in the u-direction, $\mathrm{STD}_{\mathrm{tb},u} = 10\,\mu m$ and $\mathrm{STD}_{\mathrm{bb},u} = 8.32\,\mu m$.

Although the determined alignment parameters do not fully recover the telescope's misalignment, a clear improvement over the initial state can be observed (see Fig. 7.11), and the estimated alignment parameters will be used in further analysis.

7.3.2.3. General Characteristics of the Measured Data

Before performing the DUT studies, a general overview of the measurement specifications will be provided. As a reference, a total of $N_{\mathrm{events}} = 1{\cdot}10^5$ atmospheric muon events have been generated and analyzed in the same way as the recorded data.
As shown in Fig. 7.13, the recorded data show a strong tendency towards events with only one cluster. These events appear in the simulated data to some extent, but at a significantly lower level. A possible explanation for this effect is the presence of noise in the data, as indicated by the non-vanishing number of events with more than four clusters.
The track-finding algorithm has been applied with a χ^2_r cut of $\chi^2_{r,cut}$=100 to capture a broad range of the fit-quality distribution, reconstructing a total of 676 potential atmospheric muon tracks. The resulting distribution shows a significant deviation from the simulation towards higher χ^2_r values. Possible contributors to this shift are the not fully compensated misalignment (see Sec. 7.3.1.1) as well as an underestimation of multiple scattering in the simulations. Also, it has to be noted that the simulations do not consider a non 100 % detection efficiency of each sensor.
Given the characteristic angular distribution of atmospheric muons (see Sec. 5.3.1), the distributions of zenith angle θ as well as azimuthal angle φ can be compared to the expected distributions.
The results can be found in Fig. 7.14. The simulated data shows a clear bias in the azimuth angle ϕ that can be described as an ellipse that is compressed in the y-regime. This is due to the smaller y-expansion of each sensor compared to the x-expansion, leading to a much lower angular acceptance for tracks tilted within the zy-plane and, in general, rotated into the y-direction. This effect can be observed in the data as well, where it appears to be

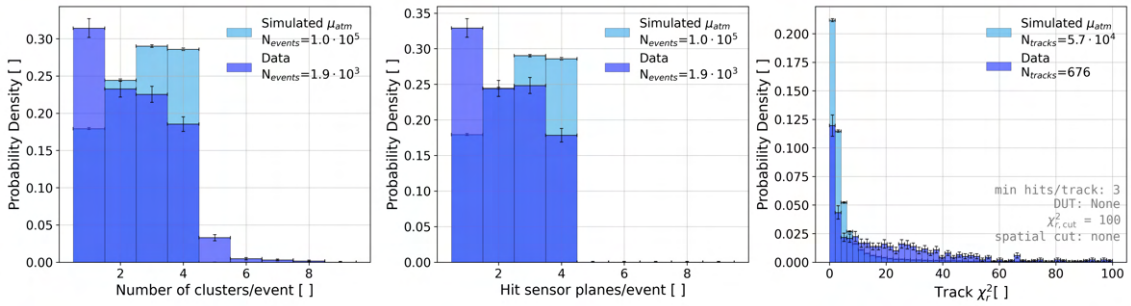


Figure 7.13.: General specifications of the measurement and simulated atmospheric muon data. From left to right: Probability density (see Eq. A.11) of Number of clusters/hits per event, Number of hit sensor planes/event, and the track χ^2_r.

even stronger. Presumably, this is due to a misalignment in the local tracking system in the y-direction, resulting in even smaller acceptance in that direction.
The distribution of the zenith angle θ of the simulated data shows a similarity to the characteristic distribution function of atmospheric muons (see Sec. 5.3.1) that is cut off at the geometrically accepted maximum of the setup. However, the recorded data deviates strongly from the expected distribution, showing a tendency towards higher angles. There are two apparent explanations for this shift: the first is a relative disposition of the two scintillators used for coincidental triggering. The second one is a non-zero rotation in the atmospheric muon flux, indicating that the setup's z-axis deviates from the true maximum of the atmospheric muon azimuthal angle distribution. Both would also explain the tendency for the zenith angle distributions to show higher acceptance in the negative x direction.

7.3.2.4. Tracking Sensor Characterization

The track-based DUT-characterization aims to determine the detection efficiency ϵ and the spatial resolution σ_{spa} of the sensor (see Sec. 5.3.3), which are key parameters in sensor characterization. The results from the February 2025 ITS3 testbeam campaign at ELSA presented in Fig. 6.4 and Fig. 6.5 will serve as a qualitative benchmark. In the comparison of these results and the values obtained in the following, the comparability is, however, limited due to deviations between sensors and the difference in the particle source (p_{e^-} = 2.9 GeV/c ELSA beam and atmospheric muons).
Besides this aspect, the setup at hand, in combination with the limited number of well-reconstructable tracks, poses multiple challenges for precision measurements, as was already examined in Sec. 7.2, Sec. 7.3.1.2 and Sec. 7.3.2.2. A tentative attempt is, however, made in the following.

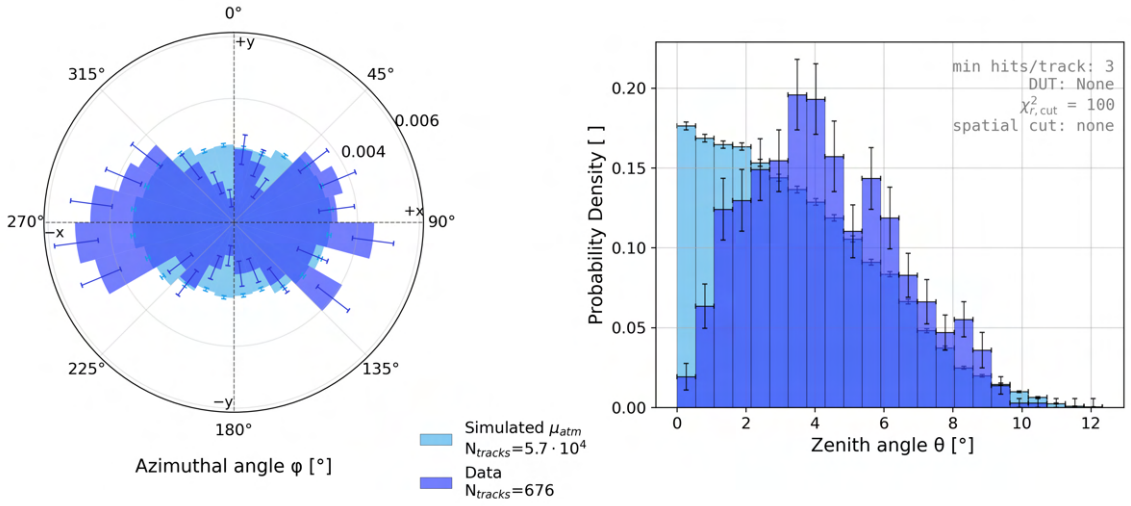


Figure 7.14.: Probability density (see Eq. A.11) of Azimuthal angle φ and zenith angle θ for tracks reconstructed from the recorded data and a simulation of atmospheric muons.

Spatial resolution In accordance with Sec. 7.9, a χ^2_r cut of 2.5 is applied to the data for the estimation of the residual width. This rigor is required to reduce the effect of multiplt scattering and to account for the contribution to tracking-resolution imprecision in the estimation of the spatial resolution σ_{spa}. Given the comparably high threshold, the charge sharing of the detained DUT clusters is rather strong (comp. Fig. 6.4) with values of (1.217 ± 0.029) pixels of the tb regions and (1.265 ± 0.022) pixels for bb. The resulting residuals are shown in Fig. 7.15. Due to the low amount of tracks, a Gaussian fit has been omitted, and the calculation of the spatial resolution (Eq. (6.16)) is performed via the statistical standard deviations of the respective distributions. σ_{track} is still derived from the respective Gaussian-fit standard deviation derived in Sec. 7.3.1.2.

For the width of the track residuals $\varepsilon_{DUT,track}$, the obtained values are $s_{tb,u,res}$=(8.143 ± 1.223) µm, $s_{tb,v,res}$=(9.452 ± 1.425) µm, $s_{bb,u,res}$=(6.428 ± 0.791) µm and $s_{bb,v,res}$=(9.410 ± 1.158) µm. Applying Eq. (6.16) the resulting spatial resolution of the tb is $\sigma_{spatial,tb}$=(6.50 ± 1.27) µm which falls directly onto the respective binary resolution $\sigma_{bin,tb} = 6.5$ µm and above the expected values for comparably higher thresholds taken from Fig, 6.4. The bb spatial resolution not only falls above the expected value but also above the binary resolution $\sigma_{bin,bb} = 5.2$ µm with a spatial resolution of $\sigma_{spatial,bb} = (5.89 \pm 0.95)$ µm. However, the uncertainties of the value are comparably high, and all reference values fall into the interval of uncertainty.

It can be concluded that a precision measurement of the spatial resolution σ_{spa} was not possible using the available data recorded with this setup. The deviation of the obtained

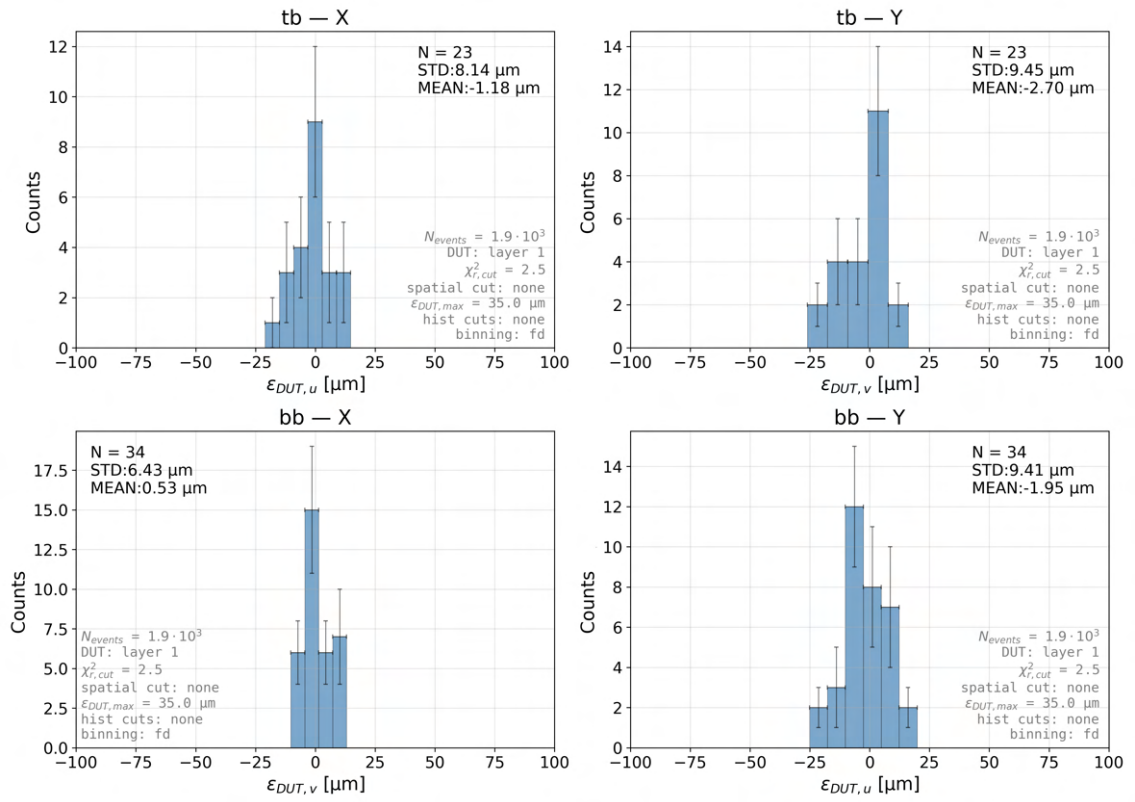


Figure 7.15.: Unbiased track residuals $\varepsilon_{\mathrm{DUT,track}}$ between the measured intersection point within the layer and the reconstructed track in local detector coordinates for the two HUs under application of $\chi^2_{r,cut} = 2.5$.

values from the expected results, as well as the high uncertainties, can be attributed to the low amount of well reconstructable tracks available and the high value of σ_{track} that becomes dominant in Eq. (6.16). In combination with the high uncertainty of σ_{res}, this results in a high degree of uncertainty of the spatial resolution (see Eq. (A.21)). Also, residual imprecisions in the alignment are not fully removed from the track residual $\varepsilon_{DUT,track}$ distributions examined (see Sec. 7.3.2.2),which is possibly widening the track residual distribution.

Detection efficiency For the detection efficiency, the same tracks and associated DUT clusters have been analyzed. A total of 25 tracks crossing the tb HU and 40 tracks crossing the bb HU have been reconstructed, resulting in detection efficiencies of $\epsilon_{tb} = 92.00^{+7.02}_{-18.03}$ % for the tb regions and $\epsilon_{bb} = 85.00^{+9.29}_{-14.84}$ % for the bb regions. Given the large uncertainties, both values lie within the reference regime of Fig. 6.5; however, the low number of well-reconstructable tracks results in very high uncertainties, making a precise determination of

the detection efficiency impossible. Setting the maximum DUT residual to a coarser value of $\varepsilon_{\mathrm{max,DUT}} = 100\,\mu\mathrm{m}$, which is the commonly applied value, and the $\chi 2_r$ cut to the higher value of 10, yields $\epsilon_{tb} = 97.73^{+2.22}_{-9.75}\,\%$, which lies within the reference regime for higher thresholds, and $\epsilon_{bb} = 92.86^{+4.48}_{-7.76}\,\%$, which, considering the still comparably high uncertainties, also matches the reference regime. Given the greater number of reconstructable tracks, the uncertainty with the coarser cut is lower, and the determined values are closer to the expected efficiencies. Nevertheless, the uncertainty remains large. It can be concluded that the detection efficiency ϵ can be determined with higher precision than the spatial resolution σ_{spa}. This difference in precision is expected, as the efficiency is far less sensitive to measurement imprecision: its uncertainty depends mainly on the number of well-reconstructable tracks. Overall, all determined values should nevertheless be viewed with caution, given the low number of well-reconstructable tracks, the overall low tracking resolution (see Sec. 7.2), and the residual misalignment (see Sec. 7.3.2.2) of the present setup.
In summary, an analysis of the DUT characteristics was possible to an extent that reproduces the nominal expectation values, such as the binary resolution and the detection efficiency measured in other experiments, although a precise determination of these parameters was not achievable given the high uncertainties.

7.4. ELSA Setup

The objective of this section is the application of the framework developed in Ch. 6 to data that has been recorded in the February 2025 ITS3 testbeam campaign at ELSA to further investigate the performance of the framework. The objective is to test the procedure using a higher amount of reconstructable tracks to overcome the limitations of the atmospheric muon measurement that has been limiting a DUT characterization of the local tracking system (see Sec. 7.3.2.4). Since the goal is to validate the framework rather than to characterize the sensor, only a single threshold performance scan that was obtained by varying the setting of VCASB of one region is analyzed.
Analog to the procedure for the local tracking system in Sec. 7.3.2, this section will start with a simulation test of the alignment and the determination of the tracking resolution σ_{track} in Sec. 7.4.1. Afterwards, the setup is aligned based on the recorded data and the transferability of determined alignment parameters between datasets is investigated in Sec. 7.4.2.1. The resulting alignment is then used to perform the threshold performance scan of bb region 0, determining the spatial resolution $\sigma_{spatial}$ and the detection efficiency ϵ in Sec. 7.4.2.2.

7.4.1. Simulation

This section will first evaluate the accuracy of the alignment procedure introduced in Sec. 7.3.1.1 when applied to the setup used at the February 2025 ITS3 testbeam campaign at ELSA with simulated electron beam datasets. Afterwards, the DUT-layer tracking resolution σ_{track} will be determined via simulated datasets.

7.4.1.1. Alignment

The Alignment procedure of the ELSA setup is tested in the same way as described in Sec. 7.3.1.1 but with the respective geometry and a simulated $p_{e^-} = 2.9\,\mathrm{GeV/c}$ ELSA beam. It shows the same non-zero center of the trajectory residual distributions $\varepsilon_{\mathrm{DUT,traj}}$ (see Fig. A.12) as already occurred in the alignment of the local tracking system (see Sec. 7.3.2.2) resulting from the convergence towards alignment parameters that unequal the actually applied misalignment as can be seen in Fig. 7.16. This supports the assumption raised in Sec. 7.3.1.1 that the solutions are ambiguous, as the limitations by tracking resolution are subsequently higher compared to the local tracking system (see Sec. 7.2) and do not mitigate the problem. Although this confirmation must be viewed under the restriction that the number of free parameters has been increased while maintaining the same number of reconstructible tracks in the analysis. Again, the residual rotational and translations offset was minimized (see Fig. A.13) given slopes of $m_u = (0.0071 \pm 0.0041)\,\mu\mathrm{m/mm}$ and $m_v = (0.032 \pm 0.014)\,\mu\mathrm{m/mm}$, and offsets of $u_0 = (0.075 \pm 0.026)\,\mu\mathrm{m}$ and $v_0 = (-0.087 \pm 0.027)\,\mu\mathrm{m}$ in the track residual $\varepsilon_{DUT,track}$ against track intersection r_x plot.

7.4.1.2. DUT Tracking Resolution

The track residual is estimated by generating a dataset using the standard ELSA beam simulation parameters. To filter for well-reconstructed tracks, a χ^2_r cut of $\chi^2_{r,cut} = 2.5$ is used. The resulting distribution is shown in Fig. 7.17. From the gaussian-fits resolutions of $\sigma_{track,bb,reg0} = (2.981 \pm 0.015)\,\mu\mathrm{m}$ and $\sigma_{track,bb,reg0} = (2.973 \pm 0.017)\,\mu\mathrm{m}$ result. Although the Gaussian fit does not describe the distribution perfectly, the distribution's width is still determined to a good approximation, as evidenced by the comparably low uncertainties of these standard deviations.
It can be summarized that the tracking resolution is significantly smaller than the respective binary resolution, so that a measurement of the spatial resolution $\sigma_{spatial}$ is possible to a significantly higher degree of precision compared to the local tracking system (see Sec. 7.3.1.2).

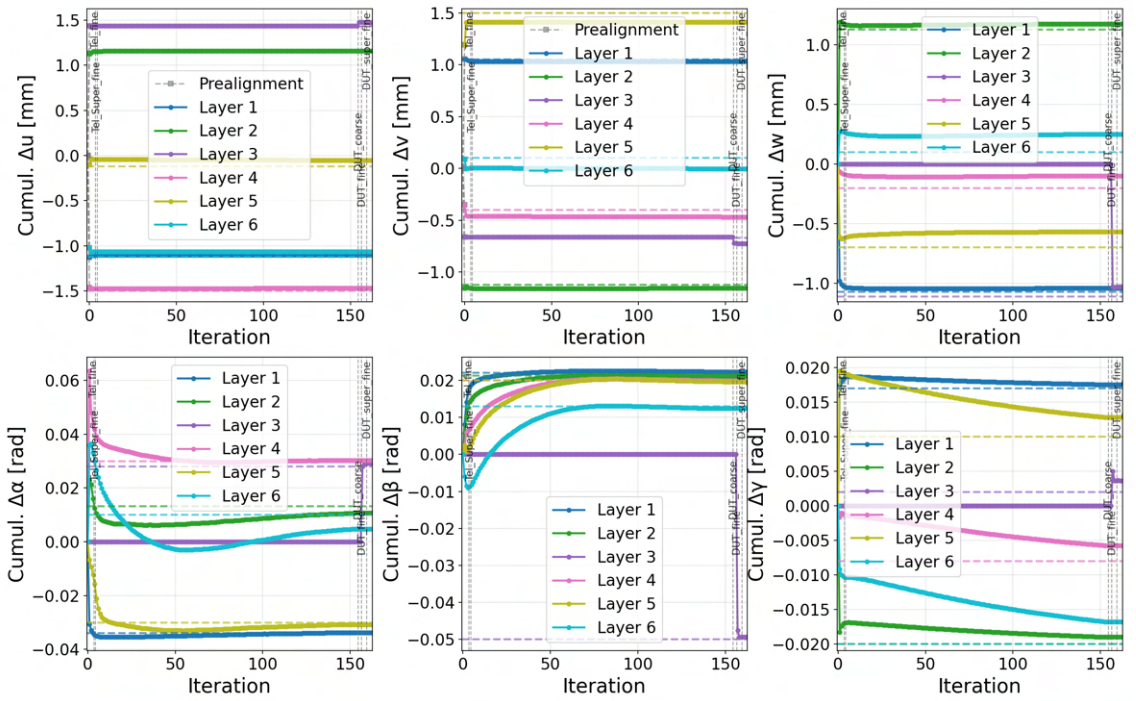


Figure 7.16.: Incremental evolution of the alignment parameters for the alignment of the local tracking system using $1 \cdot 10^5$ simulated ELSA events. The horizontal dotted lines indicate the true misalignment parameters defining $\Delta R_{\text{mis,layer}}$ and $r_{0,\text{mis,layer}}$. The vertical grey dotted lines mark the boundaries between the individual alignment stages. Layer 0 serves as the reference layer for the alignment. Note that the DUT alignment can be observed on the edge within the last iterations.

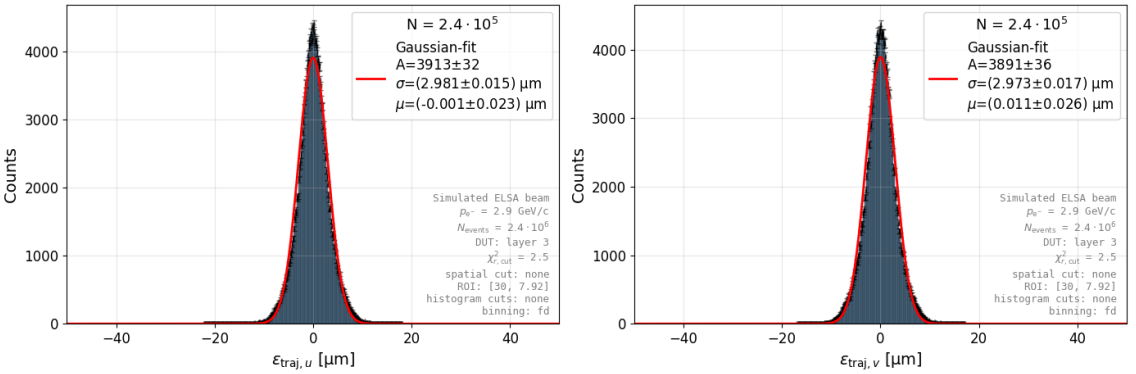


Figure 7.17.: Unbiased trajectory residuals $\varepsilon_{\text{DUT,traj}}$ between the simulated intersection point within the layer and the reconstructed track in local detector coordinates for the two HUs. For the track reconstruction $\chi^2_{r,cut}$= 2.5 was set. To estimate the respective tracking resolution, a Gaussian fit was applied.

7.4.2. Data Analysis

During the test beam at ELSA, multiple parameters were tested. As the objective of the following analysis is not sensor characterization but the validation of the framework implemented in this work, only a single-parameter scan of a single region is analyzed. For this, a VCASB variation scan with a supplied back bias of $V_{PSUB} = -1.2V$ was selected; hence, the thresholds tested are much lower than those used in the local tracking system. The reference layers, as well as the remaining regions of the DUT, were operated in the standard settings listed in Tab. 5.1. The nominal beam momentum recorded for this measurement was $p_{e^-} = 2.9\,\mathrm{GeV/c}$. A visualization of the cluster positions resulting from the data set

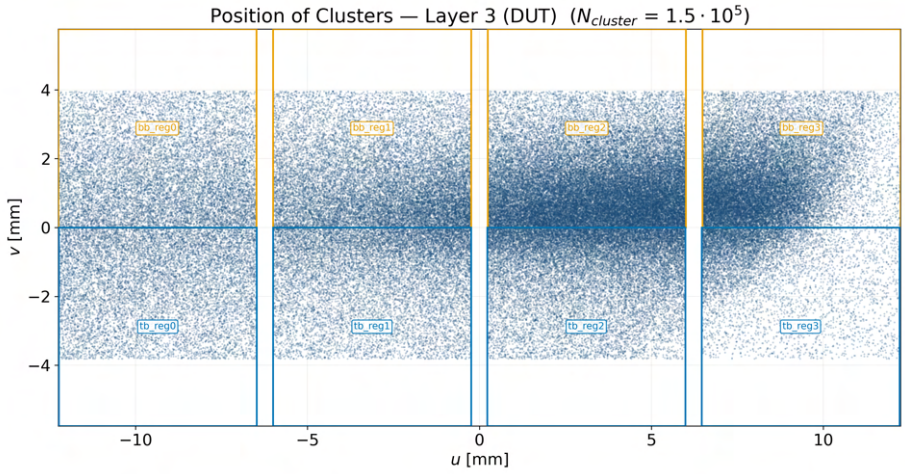


Figure 7.18.: Cluster positions resulting from the dataset used for the alignment procedure in local coordinates. The cut-offs result from the set ROI

used for alignment is shown in Fig. 7.18. As can be seen, the beam does not cover all regions homogeneously, with maximum intensity in the bb regions 2 and 3. Nevertheless, the bb region 0 is covered to a degree sufficient for the quantitative analysis at hand. The deviation of actual beam shape from the gaussian shape that is assumed for the simulation of the ELSA beam (see Sec. 6.2.3) can be neglected for the aspects investigated in the above, as the alignment depends on the inhomogeneous coverage of the sensor more than the asymmetry (see Eq. 6.9) which is covered by the beam width selected (see Sec. 7.1) and the measured tracking resolution does not depend on the beam shape, except for the angular deviation which remained small.

7.4.2.1. Alignment

The Alignment for the data analysis of the data recorded at ELSA converges properly following the convergence criteria from Tab. A.7. The drift towards higher angles that required a reduction of the convergence threshold in the alignment of the local tracking system (see Sec. 7.3.2.2) did not occur in the final stages of the incremental parameter evolution, as can be seen in Fig. 7.19. Nevertheless, the reduced convergence threshold of

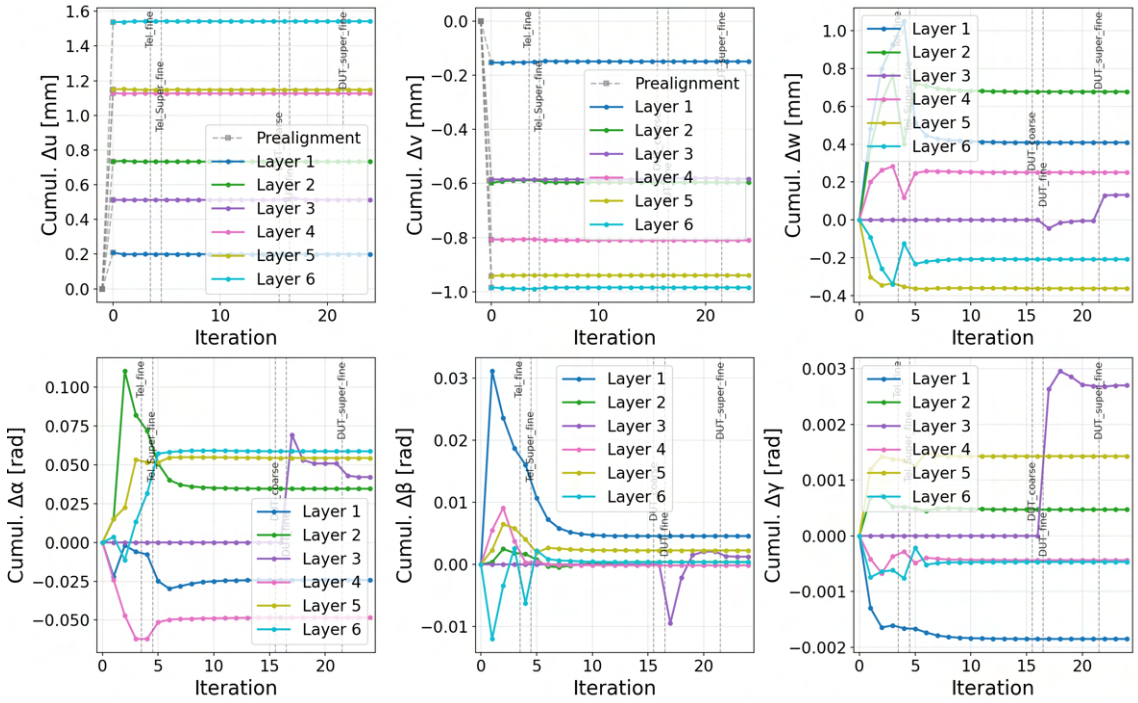


Figure 7.19.: Incremental evolution of the alignment parameters for the alignment with data obtained at ELSA. The vertical grey dotted lines mark the boundaries between the individual alignment stages. Layer 0 serves as the reference layer for the alignment.

the mean shift of track residuals $\varepsilon_{\text{track}}$ of 0.01 µm was maintained for reasons of efficiency, as a minimization of the effective rotational and translational misalignment in the track residuals $\varepsilon_{\text{track}}$ was achieved to a satisfactory level. This is quantified by the given slopes of $m_u = (-0.0150 \pm 0.0033)$ µm/mm and $m_v = (0.018 \pm 0.012)$ µm/mm, and offsets of $u_0 = (0.026 \pm 0.020)$ µm and $v_0 = (-0.006 \pm 0.021)$ µm in the track residual $\varepsilon_{DUT,track}$ against track intersection q_x plot (see Fig.7.20), which are a significant improvement of the initial parameters. On closer inspection, the respective initial plot shows an anomalous kink in the center of the v-regime, which can likely be attributed to a rotational misalignment, as it is successfully eliminated in the final aligned dataset. However, a visible gap remains in

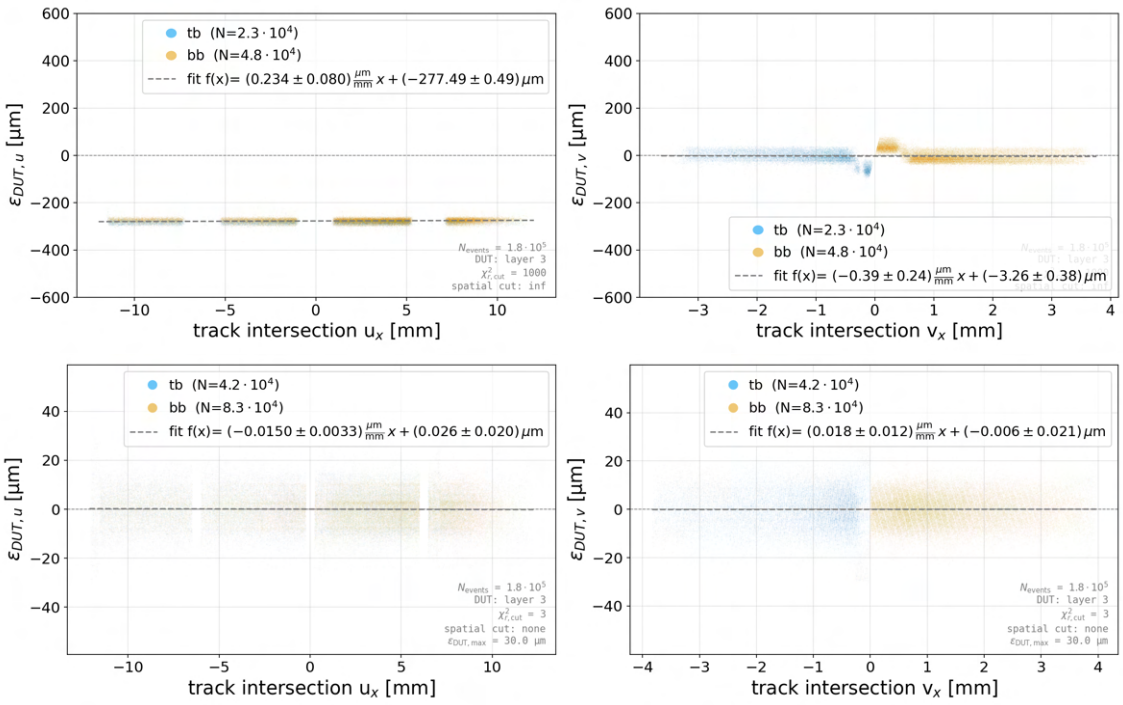


Figure 7.20.: DUT residual ε_{DUT} of track intersection q_m and measured position q_x plotted against the point of track intersection q_m in the respective dimension before (top) and after (bottom) the alignment of the data obtained at ELSA. The residuals from the unaligned dataset were determined using the track reconstruction specifications of the first alignment stage.

the distribution that can be attributed to the higher amount of clusters on the inner edge of the bb HU, as this is where the beam-spot center is positioned (see Fig. 7.18).
As the overall goal of this section is to provide a representative study of the threshold dependence of the DUT bb region 0 characteristics, the transferability of the alignment parameters is important. As a reference, the residuals distribution in bb region 1 will be depicted in the upper part of Fig. 7.21. To ensure comparability, region 1 was selected rather than region 0, as the respective front-end settings were set to default values for all measurements. The resulting distribution of the dataset used for the alignment has a mean of $\mu_u = (-0.03 \pm 0.13)$ µm and $\mu_v = (-0.02 \pm 0.11)$ and a width of $\sigma_{res,u} = (5.926 \pm 0.083)$ µm and $\sigma_{res,v} = (5.954 \pm 0.070)$ µm. An exemplary track residual $\varepsilon_{\text{track}}$ distribution from a different dataset after the application of the determined alignment correction parameters can be found in the lower part of Fig. 7.21.The distributions remain centered with a mean of $\mu_u = (-0.09 \pm 0.18)$ µm and $\mu_v = (0.14 \pm 0.16)$ µm. Also, the width of the respective Gaussian fit remains minimized and similar in the u and the v-plane with standard deviations of $\sigma_{res,u} = (5.86 \pm 0.11)$ µm and $\sigma_{res,v} = (5.900 \pm 0.095)$ µm. This is an important figure of

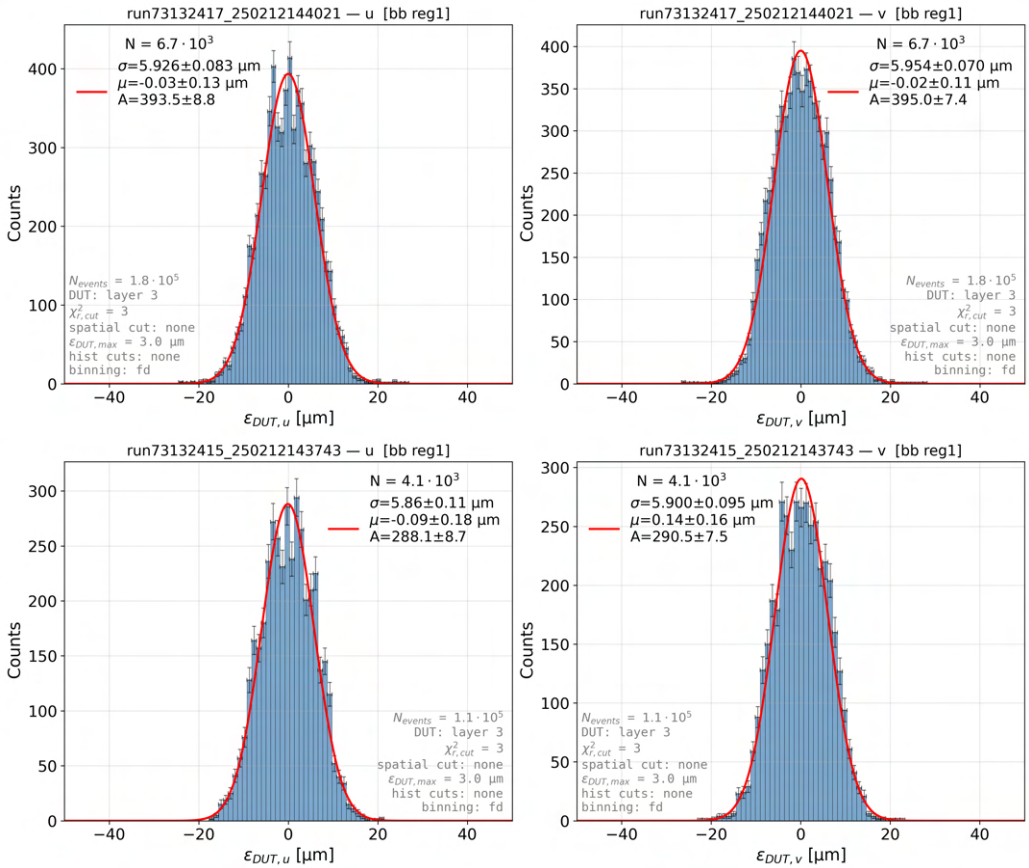


Figure 7.21.: Unbiased track residuals $\varepsilon_{\mathrm{DUT,track}}$ between the measured intersection point within the layer and the reconstructed track in local detector coordinates for the two HUs under application of $\chi^2_{r,cut} = 2.5$. The upper figure shows the residuals for the data used for the alignment, the lower figure shows the residuals of a different dataset under the application of the alignment parameters obtained from the above dataset

merit for the alignment algorithm and further supports the assumption that the solution it is finding is ambiguous. Although the alignment minimizes the residual distributions to a satisfactory level, residual misalignment is still evident in the distributions. Nevertheless, it is assumed that the width of the residuals distribution σ_{res} can be derived from the aligned data in good approximation. To achieve a better result, a first step would probably be to lower the convergence criterion. However, this would go beyond the scope of this thesis and is therefore a matter for further investigation.

7.4.2.2. Tracking Sensor Characterization

For the characterization measurement of bb region 0, a χ^2_r cut of $\chi^2_{r,cut} = 2.5$ has been applied to filter for tracks that are well reconstructed. A majority of tracks fall below this cut, as shown in Fig. 7.22. For the DUT cluster association, the maximum residual is set to

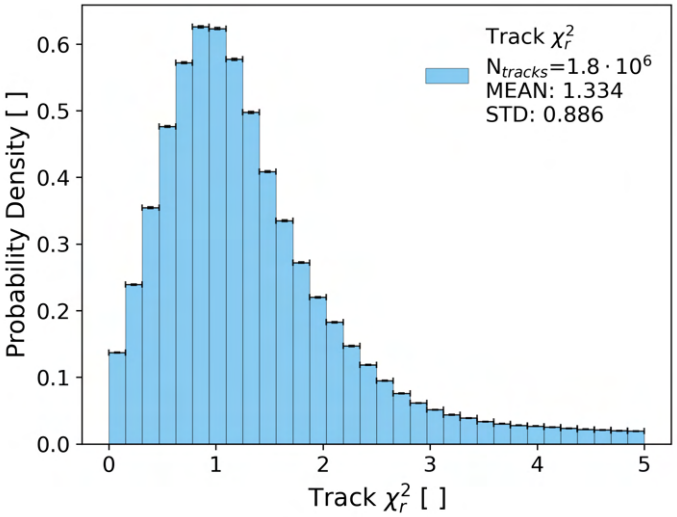


Figure 7.22.: Probability density (see Eq. A.11) of track quality χ^2_r distribution over all datasets obtained with a spatial cut of $\chi^2_{r,cut} = 5$

$\varepsilon_{DUT,max} = 30\,\mu m$, which is lower than used in Fig. 6.4. The lower cut is selected to reduce clusters that are more than one pixel width away from the predicted track intersection.

Spatial resolution As the distributions follow a Gaussian distribution in good approximation (see, for example, Fig. A.14) the residuals width σ_{res} is resolved via a gaussian fit. Respectively, the tracking resolution is assumed to be the Gaussian-fit standard deviation determined in Sec. 7.4.1.2. The spatial resolution is then derived using Eq.(6.16) for all available datasets. To determine the respective threshold, the VCASB setting for the bb region 0 of the dataset is compared with the threshold scan data for the corresponding VCASB setting of this region. The resulting value is set as the threshold of the respective run. In addition to spatial resolution, the average cluster size in pixels is also derived for each dataset using the average size of the associated DUT cluster. The results can be found in Fig. 7.23. As can be seen, the results clearly follow the characteristic trend of spatial resolution rising with the lower threshold, and the thereby increased average cluster size is evident in the data. With a best values of $\sigma_{spa,bb,reg0} = (4.570 \pm 0.061)\,\mu m$ for a threshold of 11 DAC (VCASB = 116) and a highest value of $\sigma_{spa,bb,reg0} = (5.026 \pm 0.077)\,\mu m$ for a

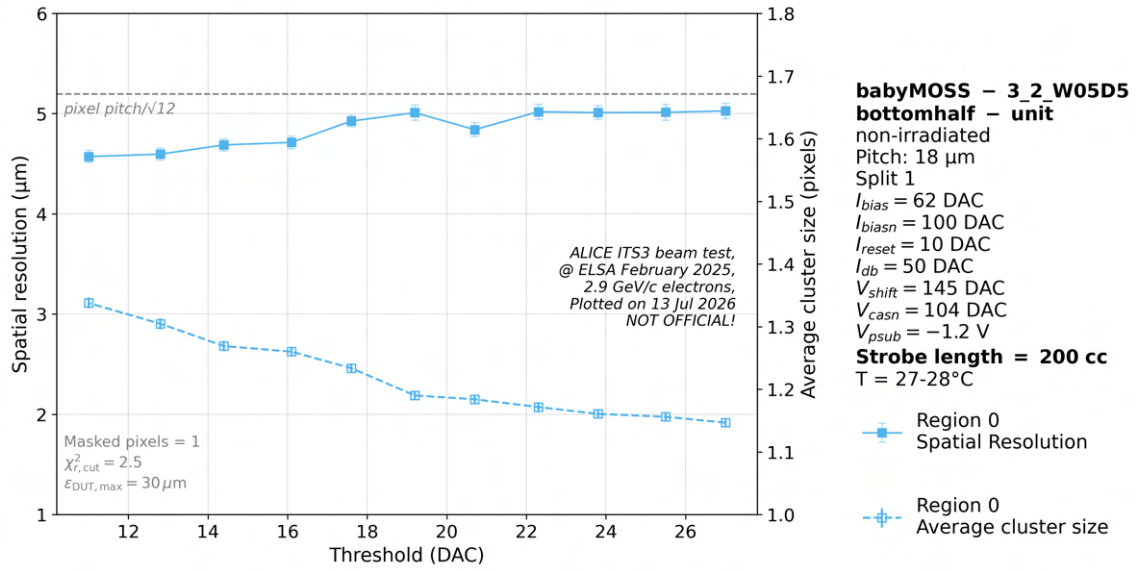


Figure 7.23.: Spatial resolution and average cluster size for babyMOSS 3_2_W05D5 bb region 0 obtained from the data recorded within the February 2025 ITS3 test-beam campaign at ELSA via the local framework. This is not an official ITS3 result!

threshold of 28.5 DAC (VCASB = 83). Also, the spatial resolution $\sigma_{spatial}$ clearly falls below the binary resolution, which, taken together with the reduced determined uncertainty, indicates that the determination of the spatial resolution was possible to a sub-binary degree. However, the values clearly deviate from the reference in Fig. 6.4 by an estimated 5% beyond the uncertainties. Resultingly, it has to be concluded that a certain degree of systematic uncertainties must underlie the measurement. This can be attributed to a variety of possible error sources, such as the simplified straight-line tracking model (see Sec. 6.2.2) and reduced accuracy of the alignment model (see Sec. 7.4.2.1). Also, general parameter settings like a difference in the χ^2_r cut or a less restrictive frequency cut in the masking of noisy pixels are possible contributors, although the characteristics of the set of tracks used for the analysis do not seem to differ strongly, as the systematic differences do not appear to the same extent in the development of the average cluster size distributions.

Detection efficiency The results from the detection efficiency estimation can be found in Fig. 7.24. Again, the characteristic development in relation to the threshold can be observed from the data, with a best value of $\epsilon_{bb,reg0} = 95.67^{+0.56}_{-0.62}\%$ for a threshold of 11 DAC (VCASB = 116) and $\epsilon_{bb,reg0} = 99.71^{+0.13}_{-0.2}\%$ for a threshold of 28.5 DAC (VCASB = 83). Again, a deviation from the reference can be observed, which, however, is smaller than the deviation in spatial resolution and, besides, the given systematic error source is explained by the

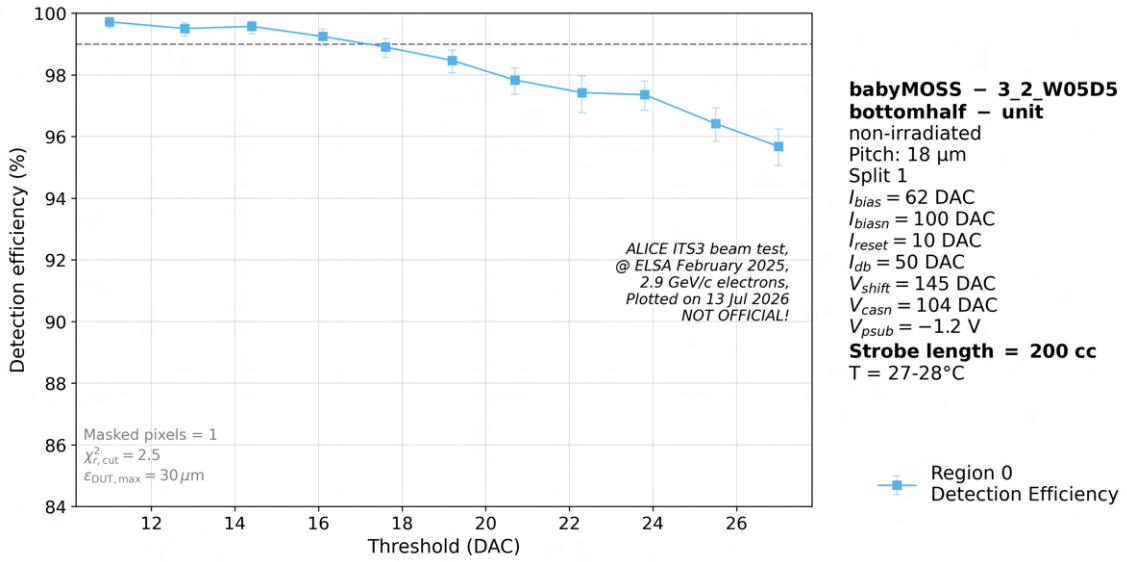


Figure 7.24.: Detection efficiency ϵ and average cluster size for babyMOSS 3_2_W05D5 bb region 0 obtained from the data recorded within the February 2025 ITS3 testbeam campaign at ELSA via the local framework. This is not an official ITS3 result!

tighter DUT association cut $\varepsilon_{DUT,max}$, which will lower the detection efficiency. However, this effect seems to be almost negligible given the width of the track residual distribution (see, for example, Fig. A.14), and the main contributor will again be the deficits of the used developed overall analysis procedure.

7.5. Summary

This section summarizes the results and findings from the previous analysis. First, the measurement of muons is summarized in Sec. 7.5.1, and afterwards the results for Python-based framework are collected in 7.5.2.

7.5.1. Measurement of Atmospheric Muons with the Local Tracking System

The setup developed within Sec. 5.3 operated successfully with a coincidental triggering system. A measurement and track reconstruction over multiple sensor regions of possible atmospheric muon candidates was performed successfully. Also, the measured and analyzed tracks were validated to an extent via the simulation of atmospheric muons within the same setup geometry, via the measured track angle distribution, which coincides to a certain degree (see Sec. 7.3.2.3), indicating that atmospheric muon events have been measured and the trajectory was successfully reconstructed.
On the downside, the event rates expected for the setup were dismissed by a factor of about four (see Sec. A.3). This indicates problems with the overall alignment of the setup and possibly the trigger mechanism, as the deviation relates to the rate of events with at least one cluster. This suspicion needs to be investigated further, as it is not entirely clear how noise and an overly optimistic simulation of the trigger system affect this limitation.
Owed to the low amount of measured tracks (see Sec. A.3), the setups geometry together with the amount of expected multiple scattering (see Sec. 7.2 and Sec. 7.3.1.2) and a residual misalignment (see Sec. 7.3.2.2) a precision analysis of the DUT characteristic (i.e. the spatial resolution σ_{spa} and detection efficiency ϵ) was not successful, as all determined values are marked by considerable uncertainty as was shown in Sec. 7.3.2.4.
All in all, it can be concluded that the local tracking system was operated and the trajectories of atmospheric muons have been measured and reconstructed successfully. A precise DUT analysis, however, was not possible under the given circumstances.

7.5.2. Validation of the Python-based Framework

The Python-based framework was evaluated in three primary ways.

1. A qualitative review of the interplay of the simulator described in Sec.6.2.3 and the track finding algorithm (see Sec. 6.2.2) performed via the evaluation of track residual RMS in Sec. 7.2
2. An investigation on the applicability and precision of the alignment algorithm developed in Sec. 6.2.4 via simulation in Sec. 7.3.1.1 and Sec. 7.4.1.1 as well as a test of the

transferability of determined alignment parameters between datasets in Sec. 7.4.2.1

3. A qualitative analysis of the complete reconstruction and analysis chain presented in Ch. 6 performed on a threshold scan recorded during the February 2025 ITS3 testbeam campaign at ELSA in Sec. 7.4.2.2.

The interplay investigated in Sec. 7.2 behaves in the way expected, as the track reconstruction quality falls for lower particle momenta and rises with the setup used at ELSA as it contains more points of measurement. Also, it was an indicator for the difficulties involved in precise measurement discussed in Sec. 7.3.2.4.
The alignment works to very high precision for a single misaligned layer in a four-layer setup and a high amount of events of particles with a fixed high energy as described in Sec. 7.3.1.1. For a fully misaligned telescope, however, the algorithm does not correctly determine the applied misalignment for either the local tracking system or the ELSA setup (see Sec. 7.4.1.1). However, in both cases, the remaining misalignment in the track residual distributions was significantly reduced. Also, the transferability of the alignment parameters between datasets was proven in Sec. 7.4.2.1. All in all, this indicates that, although the correct initial misalignment was not determined, a non-unique solution that eliminates the misalignment effects, as reflected in the track residual distributions, can be determined. Nevertheless, a certain degree of misalignment remains, and possible errors, such as angle divergence, were not fully compensated. It should also be noted that full convergence was not achieved, as the convergence criterion, based solely on changes in residuals, is of a rather practical nature and does not guarantee convergence of all parameters.
The analysis of the DUT characteristic presented in Sec. 7.4.2.2 indicates that the full reconstruction and analysis pipeline can be successfully applied to data taken at a testbeam and allows a sub-binary analysis of the spatial resolution σ_{spa} and an examination of the detection efficiency ϵ to a certain degree. However, this analysis provides only a qualitative benchmark, in which deviations from the reference values are identified (see Fig. 6.4 and Fig. 6.5). This can largely be attributed to the weaknesses of the developed pipeline identified above (i.e., the imprecisions in the alignment and track reconstruction), as well as possible imprecisions in the simulation used to determine σ_{track}. Also, differences in the overall applied cuts and event selection are a possible contributor.

8. Conclusion

This work focused on the operation and testing of the babyMOSS prototype sensor in a local experimental setup at the University of Münster, alongside the development of an accessible software framework enabling the measurement and reconstruction of atmospheric muon trajectories.

During the course of this thesis, contributions were made to several testbeam campaigns of the ITS3 project at various research institutions, with the objective of characterizing the babyMOSS sensor. The characterization of the babyMOSS sensor is now at an advanced stage, and the project has entered the evaluation phase for the next prototype of the MOSAIX chip. In parallel, preparations are underway for the final installation of the ITS3 panel during LS3.

Based on the experience gained in the aforementioned testbeam campaigns, thea local measurement setup was designed and implemented. This local tracking system represents a reduced and vertically stacked variant of a conventional testbeam telescope (see Sec. 5.1.1 and Sec. 5.3) as used during the attended testbeam campaigns. It employs four tracking layers and a coincidence-based trigger system utilizing two scintillator detectors.

All babyMOSS sensors used in the local tracking system were characterized for two distinct principal configurations of the front-end electronics in order to determine an optimal working point (see Sec. 5.3.3). Subsequently, a 22-day measurement campaign of atmospheric muons was conducted.

To analyze and reconstruct the acquired data, while ensuring broad usability for future local projects, a *Python*-based analysis framework was developed. This framework supplements those components of the standard *Corryvreckan* workflow that are not well suited to the specific requirements of the local tracking system (see Ch. 6). The developed framework includes a track-finding algorithm, an alignment procedure, and a tool for generating simulated datasets for the validation and performance assessment of both the recorded data and the software itself.

A detailed analysis of the collected data and the developed framework was conducted and is presented in Ch. 7. It can be concluded that the measurement of potential atmospheric muon candidates, as well as the reconstruction of their trajectories, was successfully achieved using the local tracking system. However, a comprehensive and high-precision characteri-

zation of the DUT could not be performed. This limitation arises from the broad energy spectrum and the current geometry of the setup (see Sec. 7.2), which, in combination with the low number of reconstructable tracks, leads to substantial uncertainties in the analysis (see Sec. 7.3.1.2). In addition, the overall rate of events recorded and reconstructed with at least one cluster is lower by a factor of four than the expected value, which necessitates further investigation.

In addition to the analysis of atmospheric muon data, a qualitative validation of the developed software framework was conducted in Ch. 7. The interaction between the simulation framework and the track-finding algorithm reproduces the expected phenomenology (see Sec. 7.2). The alignment procedure was validated using events generated with the developed simulator. It was demonstrated that, although the alignment procedure does not recover the exact global misalignment configuration implemented in the simulations, it does converge to a solution that partially compensates the impact of the misalignment on the residuals (see Sec. 7.3.1.1, Sec. 7.3.2.2, Sec. 7.4.1.1, Sec. 7.4.2.1). This observation suggests that the alignment problem does not admit a unique solution, but that the derived alignment constants nonetheless provide an effective mitigation of the residual offsets. This interpretation is further supported by the fact that the obtained alignment parameters are transferable between different datasets, where they consistently reduce the residual distortions, as shown in Sec. 7.4.2.1.

To further evaluate the performance and robustness of the software framework, the complete reconstruction and analysis chain (see Fig. 6.1) was applied to a parameter scan acquired during the February 2025 ITS3 test beam campaign at ELSA. The results indicate that, while sub-binary spatial resolution can be achieved, the measurements are affected by several potential systematic uncertainties. The most prominent among these are residual misalignments and the use of a simplified straight-line track model.

In summary, both the local experimental setup and the developed analysis framework fulfill the initial qualitative requirements; however, further refinement of both is required to enable a quantitatively precise characterization of the sensor performance. In particular, the impact of low event rates must be investigated in more detail to exclude additional sources of error and increase the number of reconstructable tracks.

9. Outlook

This section provides a concise yet comprehensive perspective on the prospective developments of the local experimental setup and the ALICE silicon pixel tracking systems.

9.1. Local Tracking System

A major remaining limitation of the local tracking system described in Ch. 5 is the low track-reconstruction performance quantified in Sec. 7.2 and Sec. 7.3.1.2. This deficiency can be attributed to the simplified track model see Sec. 6.2.2, as well as to the broad energy spectrum of the atmospheric muons used as particle source and the consequently enhanced degree of multiple scattering. In addition to the restricted tracking resolution, the setup exhibited a counting rate below the expected value, which may be attributable to a residual misalignment of the telescope.
Since the limitations arising from the use of atmospheric muons are intrinsic and cannot be mitigated without changing the particle source, the remaining options are to reduce multiple scattering by minimizing the material budget x/X_0 (see Eq. 3.4) traversed by the particles and to further improve the alignment.
One possible approach to reducing the local material budget x/X_0 of the setup is the removal of the protective covers from the babyMOSS, as they constitute the dominant contribution to the material budget traversed by the particles. A dedicated simulation, performed and analyzed analogously to the procedure described in Sec. 7.3.1.2 but with the scattering contributions from the covers disabled, indicates that the tracking resolution can be improved from $\sigma_{\text{track,tb}} = (5.908 \pm 0.021)\,\mu\text{m}$ in the tb regions and $\sigma_{\text{track,tb}} = (5.136 \pm 0.017)\,\mu\text{m}$ in the bb regions with covers, to $\sigma_{\text{track,tb}} = (5.033 \pm 0.015)\,\mu\text{m}$ in the tb regions and $\sigma_{\text{track,tb}} = (4.340 \pm 0.011)\,\mu\text{m}$ in the bb regions without covers.

Although these resolutions do not reach the precision achieved with a conventional babyMOSS telescope operated at ELSA (see Sec. 7.4.1.2), they remain smaller than the corresponding binary resolutions of $\sigma_{\text{bin,tb}} = 6.5\,\mu\text{m}$ and $\sigma_{\text{bin,bb}} = 5.2\,\mu\text{m}$ to a significant degree. However, operating the system without protective covers necessitates an alternative solution to mitigate the impact of debris and ambient light.

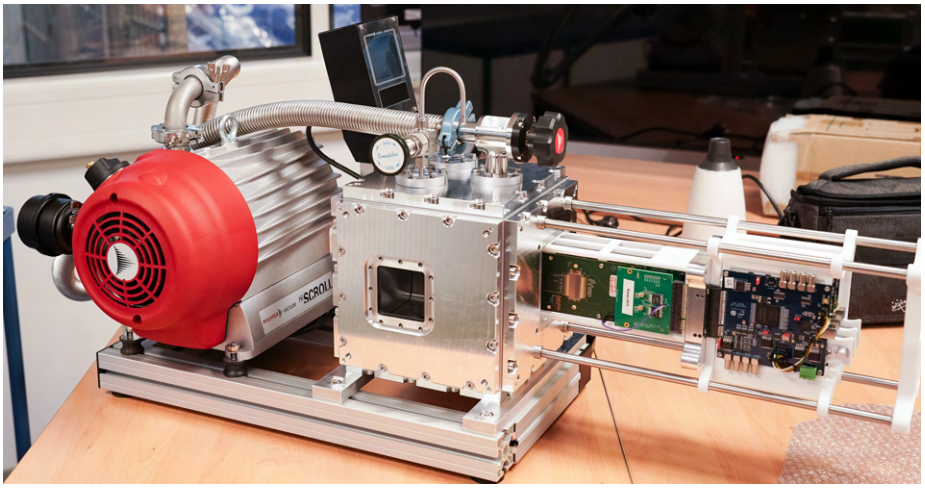


Figure 9.1.: Photograph of the vacuum chamber developed by Daniel Bonaventura taken at a testbeam campaign at DESYII in February 2026. Note that the vacuum chamber can be rotated from the shown horizontal configuration to vertical one.

A suitable alternative is the vacuum chamber shown in Fig. 9.1. This chamber was developed by Daniel Bonaventura at the University of Münster and has already been successfully deployed during a test beam campaign at the **D**eutsches **E**lektronen-**S**ynchrotron (DESY) II test beam facility in February 2026. The chamber accommodates carriers for three layers of babyMOSS carrier cards, which can be inserted into a rotatable vacuum vessel operating at pressures on the order of several 10×10^{-2} mbar. To ensure that traversing particles experience minimal perturbation, the chamber is equipped with two entrance windows (Kapton, 0.025 mm, and aluminum, 0.075 µm) placed at the respective positions. Sensor powering and operation can be performed externally via an attached DAQ board. In addition, the chamber includes mounts for the scintillator detectors used in the local tracking system, located above each entrance window.

Since vacuum operation is not strictly required for all use cases, a second variant of the chamber without a vacuum pump was constructed for non-testbeam applications, such as laboratory courses. Simulations of the local tracking system with three instead of four tracking layers indicate that, even with only three layers, the achieved tracking resolutions still significantly surpass the binary resolution and remain comparable to those obtained with the full local tracking system (see Sec. 7.3.1.2). In particular, tracking resolutions of (5.177 ± 0.013) µm are obtained for tb regions, and $\sigma_{track,tb} = (4.418 \pm 0.010)$ µm for bb regions.

Beyond the improved tracking performance, the chamber provides a substantially more rigid mechanical support for both the scintillator detectors and the babyMOSS system than the current local tracking system (see Sec. 5.3). This enhanced mechanical stability is

expected to reduce relative misalignments, potentially increasing the fraction of successfully reconstructable events. However, it must be noted that the misalignment in the initial setup cannot account for the observed discrepancy between the expected and measured event rates. One possible solution to this problem could be to bypass the coincidence-based trigger by implementing a continuous trigger, as is done, for instance, for the measurement of atmospheric muons in [38].
Considering these evaluated aspects, the presented setup offers promising prospects for more precise and higher-throughput measurements of atmospheric muons. A more detailed investigation of its operation is planned for future studies.

9.2. ALICE3

From a broader perspective that extends beyond the immediate scope of this work, the progress in the development and integration of MAPS within the ALICE project is not limited to the ITS upgrade during the **L**ong-**S**hutdown (LS)3 shutdown. Instead, a comprehensive upgrade of the entire ALICE apparatus to the future ALICE3 detector is planned as part of the high-luminosity Runs 5 and 6 of the LHC. Commissioning of ALICE3 is planned for LS4 of the LHC, which is currently scheduled for 2034–2035.

The primary technical objectives of this upgrade are to improve several key detector performance parameters and enable more precise and differential measurements of various aspects of QCD. These include, in particular, more detailed studies of the QGP, a deeper understanding of thermalization mechanisms, measurements of the temperature via thermal electromagnetic radiation, and the characterization of critical behavior in the vicinity of the cross-over transition between hadronic matter and the QGP [39]. The corresponding detector advancements are mainly characterized by an improved pointing resolution over a wide pseudorapidity[1] range of -4 $< \eta <$ 4, a reduced material budget in the innermost detector layers, as well as enhanced **P**article **ID**entification (PID) capabilities [39].

A schematic representation of the preliminary ALICE3 layout from the scoping document [39] is shown in Fig. 9.2. The detector concept foresees a TOF system for electron and hadron identification, complemented by a **R**ing-**I**maging **CH**erenkov Detector (RICH), an **E**lectromagnetic **Cal**orimeter (ECal), a **M**uon **I**dentifier **D**etector (MID), and a **F**orward **C**onversion **T**racker (FCT) silicon tracker.

[1] Large pseudorapidities correspond to trajectories of particles that propagate at shallow angles with respect to the beam axis.

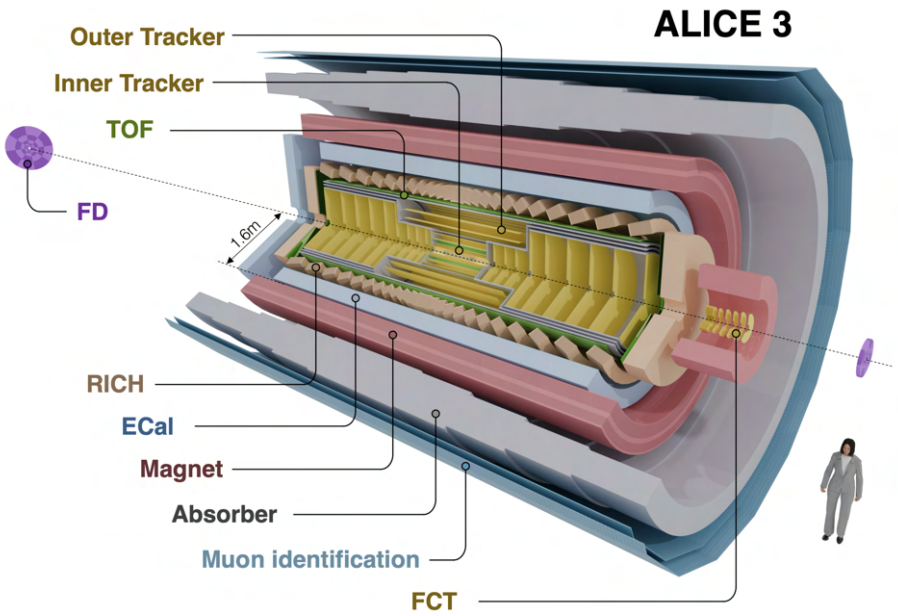


Figure 9.2.: Schematic illustration of the ALICE3 detector concept, taken from [39].

A central component of the experiment will be the reconstruction of charged-particle trajectories using a tracking system based on silicon pixel sensors arranged in barrel layers and forward disks, with a maximum material budget of $x/X_0 \approx 1\%$ per layer [40]. This tracker can be subdivided into the **I**nner **T**racker (IT), which includes a retractable **V**ertex Detector (VD) positioned inside the beam pipe and aiming at a material budget of $x/X_0 \approx 0.1\%$ per layer, and the **M**iddle **L**ayerss (MLs), which surrounds the VD and the **O**uter **T**racker (OT). The latter will employ a total active area of $50.4\,\mathrm{m}^2$ of MAPS sensors [39]. In combination with a superconducting solenoidal magnet providing a magnetic field of $B = 2\,\mathrm{T}$, the tracking system is designed to achieve a transverse momentum resolution of $\sigma(p_\mathrm{T})/p_\mathrm{T} \approx 1\%$ at $|\eta| = 4$. A joint development effort, denoted **AL**ICE3 **M**onolithic **I**ntegrated t**R**acking **A**sic (ALMIRA), has recently been initiated to provide a common design framework for the IT and OT.

Bibliography

[1] S. Acharya and (ALICE Collaboration), „Alice upgrades during the lhc long shutdown 2“, Journal of Instrumentation **19**, P05062 (2024).

[2] L. Evans and P. Bryant, „Lhc machine“, Journal of Instrumentation **3**, S08001 (2008).

[3] L. Rossi, P. Fischer, T. Rohe, and N. Wermes, *Pixel detectors: from fundamentals to applications* (Springer-Verlag Berlin Heidelberg, 2006).

[4] H. Kolanoski and N. Wermes, *Teilchendetektoren: grundlagen und anwendungen* (Springer-Verlag Berlin Heidelberg, 2016).

[5] W. Poonsawat, C. Kobdaj, M. Sitta, and Y. Yan, *Material budget calculation of the new inner tracking system, alice*, 2017.

[6] A. c. The, *Technical Design report for the ALICE Inner Tracking System 3 - ITS3 ; A bent wafer-scale monolithic pixel detector*, tech. rep., Co-project Manager: Magnus Mager, magnus.mager@cern.chds (CERN, Geneva, 2024).

[7] A. Isakov and (ALICE Collaboration), „Alice its2: overview and performance“, Journal of Instrumentation **20**, C07026 (2025).

[8] O. Abdelrahman and (ALICE Collaboration), *Characterisation of the first wafer-scale prototype for the ALICE ITS3 upgrade: the monolithic stitched sensor (MOSS)*, tech. rep., Updated authors list. Improved wording (2025).

[9] H. Kolanoski and N. Wermes, *Particle detectors: fundamentals and applications* (Oxford University Press, 2020).

[10] S. N. et al. [Particle Data Group], „Review of particle physics“, Phys. Rev. D **110**, 10.1103/PhysRevD.110.030001 (2024).

[11] H. Spieler, *Semiconductor detector systems* (CLARENDON PRESS . OXFORD, 2005).

[12] V. Leitao and (ALICE Collaboration), „Development of a stitched monolithic pixel sensor prototype (moss chip) towards the its3 upgrade of the alice inner tracking system“, Journal of Instrumentation **18**, C01044 (2023).

[13] S. Emiliani, A. Kaiser, F. Piro, G. Ripamonti, W. Snoeys, and A. Villani, „Design, simulation and characterization of the alice its3 moss analog front-end“, Journal of Instrumentation **21**, C01011 (2026).

[14] F. Piro, G. A. Rinella, A. Andronic, M. Antonelli, M. Aresti, R. Baccomi, P. Becht, S. Beolè, J. Braach, M. D. Buckland, E. Buschmann, P. Camerini, F. Carnesecchi, L. Cecconi, E. Charbon, G. Contin, D. Dannheim, J. de Melo, W. Deng, A. di Mauro, et al., „A compact front-end circuit for a monolithic sensor in a 65-nm cmos imaging technology“, IEEE Transactions on Nuclear Science **70**, 2191 (2023).

[15] A. Rachev, „Commissioning of a babyMOSS beam telescope at the ELSA E3 beamline and sensor assembly for the ALICE3 experimen“, MA thesis (Carried out at the Helmholtz Institute for Radiation, Nuclear Physics submitted to the Faculty of Mathematics, and Natural Sciences of the Rheinische Friedrich-Wilhelms-Universität Bonn, July 2025).

[16] L. Terlizzi and (ALICE Collaboration), „Characterization of moss for the alice its3 for the lhc run 4“, Journal of Instrumentation **20**, C06041 (2025).

[17] H. Jansen, S. Spannagel, J. Behr, A. Bulgheroni, G. Claus, E. Corrin, D. Cussans, J. Dreyling-Eschweiler, D. Eckstein, T. Eichhorn, M. Goffe, I. M. Gregor, D. Haas, C. Muhl, H. Perrey, R. Peschke, P. Roloff, I. Rubinskiy, and M. Winter, „Performance of the eudet-type beam telescopes“, EPJ Techniques and Instrumentation **3**, `10.1140/epjti/s40485-016-0033-2` (2016).

[18] ALICE ITS3 WP3 Collaboration, *Alice its3 wp3 trigger repository*, (2026) `https://gitlab.cern.ch/alice-its3-wp3/trigger` (visited on 06/22/2026).

[19] E. D. Team and Y. Liu, *Eudaq data acquisition framework*, Accessed: 2026-03-18, 2026.

[20] E. D. Team and Y. Liu, *Eudaq2 user manual*, EUDET, AIDA (2017).

[21] W. Hillert, „The bonn electron stretcher accelerator elsa: past and future“, The European Physical Journal A - Hadrons and Nuclei **28**, 139 (2006).

[22] ELSA Group, University of Bonn, *Elsa – electron stretcher accelerator*, (2026) `https://www-elsa.physik.uni-bonn.de/elsahome.html` (visited on 06/17/2026).

[23] A. Rachev, „Commissioning of a babymoss beam telescope at the elsa e3 beam line and sensor assembly for the alice3 experiment“, Master's Thesis (Rheinische Friedrich-Wilhelms-Universität Bonn, Bonn, Germany, 2025).

[24] M. F. Baade, „Performance study of the babymoss pixel sensor in a test beam at elsa“, Bachelor's Thesis (Institut für Kernphysik, Universität Münster, Münster, Germany, 2026).

[25] I. Panasenko, *Personal communication*, 2026.

[26] C. Grupen, *Astroparticle physics*, 2nd ed., Undergraduate Texts in Physics, 136 b/w illustrations, 207 colour illustrations (Springer Cham, Cham, 2020), pp. XVII, 609.

[27] P. Shukla and S. Sankrith, „Energy and angular distributions of atmospheric muons at the earth“, International Journal of Modern Physics A **33**, 1850175 (2018).

[28] J Kröger, S. Spannagel1, and M Williams, *User manual for the corryvreckan test beam data reconstruction framework, version 1.0*, CERN, University of Heidelberg, Uniervsity of Glasgow (2019).

[29] Anthropic, *Claude Opus*, `https://www.anthropic.com/claude`, Large language model, 2025,2026.

[30] Anthropic, *Claude Sonnet*, `https://www.anthropic.com/claude`, Large language model, 2025,2026.

[31] OpenAI, *Chatgpt*, `https://chat.openai.com/`, Large language model. Accessed: 2026-06-26, 2026.

[32] GitHub, *Github copilot*, `https://github.com/features/copilot`, Accessed: 2026-06-26, 2026.

[33] B. Ulukutlu, *Analysis software for the krakow22 test beam*, Accessed: 2026-03-20, 2022.

[34] V. Karimaki, A. Heikkinen, T. Lampen, and T. Linden, *Sensor alignment by tracks*, 2003.

[35] NumPy Developers, *Numpy.linalg.lstsq*, (2026) `https://numpy.org/doc/stable/reference/generated/numpy.linalg.lstsq.html`.

[36] NumPy Developers, *Numpy.linalg.solve*, (2026) `https://numpy.org/doc/stable/reference/generated/numpy.linalg.solve.html`.

[37] M. Mager, *Telescope tracking and resolution optimizer*, (2026) `https://mmager.web.cern.ch/telescope/tracking.html` (visited on 06/19/2026).

[38] Zaksaite, Julija, *Characterization of ITS3 sensor prototypes using particle telescopes with beam and cosmics*, eng, Student Paper, 2026.

[39] A Dainese and A Di Mauro, *Scoping document for the ALICE 3 detector*, tech. rep. (CERN, Geneva, 2025).

[40] A. Collaboration, *Letter of intent for alice 3: a next-generation heavy-ion experiment at the lhc*, 2022.

[41] M. Erdmann, T. Hebbeker, and A. Schmidt, *Statistische methoden in der experimentalphysik*, German, 1., Physik (Pearson Studium, 2019), p. 224.

[42] NumPy Developers, *Numpy.std*, (2026) https://numpy.org/doc/stable/reference/generated/numpy.std.html (visited on 06/17/2026).

[43] NumPy Developers, *Numpy.histogram_bin_edges*, (2026) https://numpy.org/doc/stable/reference/generated/numpy.histogram_bin_edges.html (visited on 06/17/2026).

[44] SciPy Developers, *Orthogonal distance regression (scipy.odr)*, (2026) https://docs.scipy.org/doc/scipy/reference/odr.html (visited on 06/17/2026).

[45] ROOT Team, *Tefficiency class reference*, (2026) https://root.cern.ch/doc/v638/classTEfficiency.html (visited on 06/17/2026).

[46] SciPy Developers, *Scipy.stats.beta*, (2026) https://docs.scipy.org/doc/scipy/reference/generated/scipy.stats.beta.html (visited on 06/17/2026).

[47] ALICE ITS3, *Moss user manual*, (2024) https://gitlab.cern.ch/groups/alice-its3-wp3/moss-testing/-/wikis/Moss%20user%20manual (visited on 01/30/2025).

[48] Writefull, *Writefull: ai writing assistance for academic writing*, https://www.writefull.com, 2025,2026.

[49] DeepL SE, *Deepl translator*, https://www.deepl.com, 2025,2026.

Appendix

A. Uncertainties and Statistical Methods

This chapter will introduce and specify the calculations, statistical methods, and derive the uncertainties of the quantities estimated in the previous analysis.
It will first introduce general terms and quantities in Sec. A.1 as well as the statistical methodology in Sec. A.2. After this, it will focus on deriving the uncertainties of the determined event rates in Sec. A.3, of the estimation of the RMS in Sec. A.4, and the spatial resolution and detection efficiency in Sec. A.5.

A.1. General Uncertainties and Statistical quantities

In this section, general quantities for handling measurement uncertainties and statistical errors are introduced. The explanations primarily follow the introduction provided in Chapters 1 and 3 of [41] For a single measurement of a quantity $f = f(x_1, x_2, \ldots, x_n)$ that depends on variables x_i with the independent uncertainties Δx_i, the uncertainty of the respective result Δf following Gaussian error propagation is given by

$$\Delta f = \sqrt{\sum_{i=1}^{n} \left(\frac{\partial f}{\partial x_i}\right)^2 (\Delta x_i)^2}. \tag{A.1}$$

If the quantity $f = f(x_1, x_2, \ldots, x_n)$ depends on variables x_i with (in general) correlated uncertainties, the more general form including covariances $\mathrm{cov}(x_i, x_j)$ is

$$\Delta f = \sqrt{\sum_{i=1}^{n} \left(\frac{\partial f}{\partial x_i}\right)^2 (\Delta x_i)^2 + 2 \sum_{i<j} \frac{\partial f}{\partial x_i} \frac{\partial f}{\partial x_j} \mathrm{cov}(x_i, x_j)}. \tag{A.2}$$

For multiple measurements, the spread of the data is estimated in different ways, depending on the amount of data and its statistical behavior. If the amount of data is large and a

Normal distribution

$$f(x) = A \exp\left(-\frac{1}{2}\left(\frac{x-\mu}{\sigma}\right)^2\right). \tag{A.3}$$

can be assumed, the amplitude A, mean μ and standard deviation σ are obtained from fitting with Eq. (A.3). A parabola is used for the peak estimation in non-Gaussian distributions

$$g(x) = a\,x^2 + b\,x + c \tag{A.4}$$

where the function's maximum is given by

$$x_0 = -\frac{b}{2a}, a < 0. \tag{A.5}$$

For a smaller sample of N values x_i, the statistical mean $\bar{x}$ and the statistical standard deviation s are defined as

$$\bar{x} = \frac{1}{N}\sum_{i=1}^{N} x_i, \quad s = \sqrt{\frac{1}{N}\sum_{i=1}^{N}(x_i - \bar{x})^2}, \tag{A.6}$$

where the calculation of these values is performed via the *mean()* and *std()* functions from the *numpy* library [42]. It should be noted that the definition of s given above differs from the definition in [41], where a prefactor of $\frac{1}{N-1}$ is used instead of $\frac{1}{N}$. For very small sample sizes, this *numpy* definition introduces a bias of the true standard deviation. Wherever $\bar{x}$ and s are used as the width estimator for further calculations (instead of a Gaussian fit), the uncertainties are derived via

$$\Delta\bar{x} = \frac{s}{\sqrt{N}}, \quad \Delta s = \frac{s}{\sqrt{2\,(N-1)}}. \tag{A.7}$$

The **R**oot **M**ean **S**quare (RMS) of the same sample is defined as

$$\mathrm{RMS} = \sqrt{\frac{1}{N}\sum_{i=1}^{N} x_i^2}. \tag{A.8}$$

For Poisson counting statistics, the uncertainty of N independent counts is given by

$$\sigma_N = \sqrt{N}. \tag{A.9}$$

For binomial quantities, the uncertainty is given by

$$\sigma_p = \sqrt{\frac{p(1-p)}{n}} \tag{A.10}$$

where n is the number of measurements and p is the measured fraction.

A.2. Histograms and Gaussian Fits

Many parts of the analysis in this thesis rely on histograms for multiple generated or measured tracks and their reconstruction. In this section, the handling of uncertainties for these is explained.
When binning any value to create a histogram, the content N of each bin is a Poisson-distributed count, the uncertainty is taken as the asymmetric central $68.27\,\%$ (1σ) interval of a Poisson distribution with mean N, which for large counts ($N \gtrsim 100$) reduces to the symmetric $\sqrt{N}$.
The binning width was set using the Freedman-Diaconis-Estimator implemented in the *histogram_bin_edges()* function from the *numpy* library if no manual binning was chosen. This estimator sets the bin-width h to

$$h = \frac{2IQR}{n^{1/3}}$$

where n is the number of entries, and IQR is the interquartile range [43].
Depending on the amount of data used for these histograms, the resulting distributions are either parameterized by the statistical standard deviation (see Eq. (A.6)) or fitted by a single Gaussian (Eq. (A.3)). The model is fitted to the binned data via the *odr()*-function from the *scipy* library [44] taking both the uncertainty of the number of entries for each bin described above as well as the bin-width uncertainty, which is estimated as $\Delta x_{bin} = \frac{h}{2}$. The uncertainty of each parameter is then obtained directly from the output of the fitting function. For histograms where the y-scale is given as probability density, the bin height calculation was performed such that

$$sum_j \rho_j h = 1 \tag{A.11}$$

via *histogram()* function from the *numpy* library, where the probability density is therefore given by $\rho_j = N_j/(N_{\text{tot}}\,\Delta x_j)$. Here, N_j is the number of entries in the bin, h its width, and N_{tot} the total number of entries.

A.3. Trigger Rates

This section discusses the uncertainties associated with triggering and event rates, both in the experimental setup and in the simulated events. The expectancy value of the scintillator

trigger rate $f_{1,\mathrm{Sci}}$ was derived via

$$\begin{aligned} f_{1,\mathrm{Sci}} &= \iint_{\text{upper hemisphere}} A_{\mathrm{scint,eff}} \cdot I \,\mathrm{d}\Omega \\ &= \iint A_{\mathrm{scint}} \cos\theta \cdot I_0 \cos^2\theta \,\mathrm{d}\Omega \\ &= A_{\mathrm{scint}}\, I_0 \int_0^{2\pi}\int_0^{\pi/2} \cos^3\theta \,\sin\theta \,\mathrm{d}\theta \,\mathrm{d}\varphi \\ &= A_{\mathrm{scint}}\, I_0 \,\frac{\pi}{2} \\ &= \frac{\pi}{2} \cdot (33 \pm 1)\,\mathrm{mm} \cdot (24 \pm 1)\,\mathrm{mm} \cdot (72.5 \pm 0.2)/(\mathrm{m}^2\,\mathrm{s}\,\mathrm{sr}) \\ &= (90.2 \pm 4.7)\,\mathrm{mHz} \end{aligned} \tag{A.12}$$

where $A_{\mathrm{scint,eff}}$ is the effective surface of the scintillator and $I_{\mu,\mathrm{atm}}$ the is the expected overall flux. Both follow from the spherical integral over the upper hemisphere of the atmospheric-muon angular distribution function given by Eq. (5.2) with $I_0 = (72.5 \pm 0.2)/(\mathrm{m}^2\,\mathrm{s}\,\mathrm{sr})$ [27]. . The uncertainty of the rate on a single scintillator $f_{1,\mathrm{Sci}}$ is derived from Eq.(A.12) via gaussian error propagation (see Eq.(A.1)) and is therefore determined as

$$\sigma_A = \sqrt{(b\,\sigma_a)^2 + (a\,\sigma_b)^2} \tag{A.13}$$

$$\sigma_{f_{1,\mathrm{Sci}}} = \tfrac{\pi}{2}\sqrt{(A\,\sigma_{I_0})^2 + (I_0\,\sigma_A)^2} \tag{A.14}$$

where the uncertainty of I_0 is derived from [27] and the uncertainty of the measurement of the scintillators' edge lengths a and b is estimated to be 1 mm each. The simulated acceptances are derived from N_{Sim} independent atmospheric-muon simulation runs of $N_{\mathrm{events}} = 1 \cdot 10^4$ accepted events each (at least one hit layer required for acceptance). Simulation and measurements are evaluated with the same three acceptance criteria, each defined as the ratio of two event counts. These counts are the number of upper-scintillator hits $N_{1,\mathrm{Sci}}$, the subset that additionally hit the second scintillator (equivalently, a scheduled trigger in the measurement) N_{Sci}, and the subset that, on top of that, produced at least one layer hit (a cluster in the recorded data) N_{acc}:

1. **Sci**: The probability that an upper-scintillator hit also triggers the second scintillator,

$$R_{\mathrm{Sci(,Sim)}} = \frac{N_{\mathrm{Sci(,Sim)}}}{N_{1,\mathrm{Sci(,Sim)}}};$$

2. **Trg**: The fraction of triggered events that contain at least one layer hit (cluster), i.e.,

the trigger acceptance,

$$R_{\mathrm{Trg(,Sim)}} = \frac{N_{\mathrm{Acc(,Sim)}}}{N_{\mathrm{Sci(,Sim)}}};$$

3. **Acc**: The overall acceptance, i.e., the fraction of all upper-scintillator hits that become accepted events (e.g., contain at least one cluster and hit both scintillators),

$$R_{\mathrm{Acc(,Sim)}} = \frac{N_{\mathrm{Acc(,Sim)}}}{N_{1,\mathrm{Sci(,Sim)}}} = R_{\mathrm{Sci(,Sim)}}\, R_{\mathrm{Trg(,Sim)}}.$$

For the simulated acceptances, the statistical standard error of the mean (Eq. (A.7)) is used, under the assumption that it dominates the uncertainty of the mean. The uncertainties are therefore given by

$$\sigma_{R_{\mathrm{Sci,Sim}}} = \frac{s_{R_{\mathrm{Sci,Sim}}}}{\sqrt{N_{\mathrm{Sim}}}}, \qquad \sigma_{R_{\mathrm{Trg,Sim}}} = \frac{s_{R_{\mathrm{Trg,Sim}}}}{\sqrt{N_{\mathrm{Sim}}}}, \qquad \sigma_{R_{\mathrm{Acc,Sim}}} = \frac{s_{R_{\mathrm{Acc,Sim}}}}{\sqrt{N_{\mathrm{Sim}}}}. \tag{A.15}$$

The measured trigger rate f_{trg} and the accepted-event (minimum-hit) rate f_{min} of events with at least one hit layer, are counting rates of the form $f = N/t$. The recorded events are randomly distributed in time, so the uncertainty is assumed to follow Poisson statistics (see Eq.(A.9) while the uncertainty of the time of measurement t is assumed to be negligible. The rate uncertainty, therefore, reduces to $\sqrt{N}/t$ which results in

$$f_{\mathrm{Trg}} = \frac{N_{\mathrm{Trg}}}{t}, \qquad \sigma_{f_{\mathrm{Trg}}} = \frac{\sqrt{N_{\mathrm{Trg}}}}{t} \tag{A.16}$$

$$f_{\mathrm{min}} = \frac{N_{\mathrm{acc}}}{t}, \qquad \sigma_{f_{\mathrm{min}}} = \frac{\sqrt{N_{\mathrm{acc}}}}{t} \tag{A.17}$$

The trigger acceptance R_{Trg} is the fraction of the N_{Trg} triggers that yield at least one cluster (N_{Acc}); its uncertainty is the binomial uncertainty derived from Eq. (A.10):

$$R_{\mathrm{Trg}} = \frac{N_{\mathrm{acc}}}{N_{\mathrm{Trg}}}, \qquad \sigma_{R_{\mathrm{Trg}}} = \sqrt{\frac{R_{\mathrm{Trg}}\,(1 - R_{\mathrm{Trg}})}{N_{\mathrm{Trg}}}}. \tag{A.18}$$

The rate of events with a minimum of one hit layer is a simple product of the overall expected rate on a single scintillator $f_{1,\mathrm{Sci}}$ and the fraction of total scintillator hits resulting in a trigger and at least one hit layer $R_{\mathrm{abs,Sim}}$. The uncertainty can be derived from Eq.(A.1) to

$$f_{\mathrm{Acc,exp}} = R_{\mathrm{Acc,Sim}}\, f_{1,\mathrm{Sci}}, \qquad \sigma_{f_{\mathrm{Acc,exp}}} = \sqrt{(R_{\mathrm{Acc,Sim}}\, \sigma_{f_{1,\mathrm{Sci}}})^2 + (f_{1,\mathrm{Sci}}\, \sigma_{R_{\mathrm{Acc,Sim}}})^2} \tag{A.19}$$

A.4. Peak Determination

For the peak estimation of the RMS trajectory residuals $\varepsilon_{\mathrm{traj}}$, the peak is estimated via a parabola fit (see Eq. (A.4)) that is performed to a custom set number of bins, manually adjusted to the width of the peak. The uncertainties of the data points are estimated as described in Sec. A.2. The fit is performed via the *odr()*-function from the *scipy* library [44]. The peak position x_0 (see Eq.(A.5)) depends on the two correlated fit parameters a and b. Therefore, the uncertainty of is derived via Eq.(A.2)

$$\sigma_{x_0} = \sqrt{\left(\frac{\partial x_0}{\partial a}\right)^2 \sigma_a^2 + \left(\frac{\partial x_0}{\partial b}\right)^2 \sigma_b^2 + 2\,\frac{\partial x_0}{\partial a}\,\frac{\partial x_0}{\partial b}\,\mathrm{cov}(a,b)}, \qquad \frac{\partial x_0}{\partial a} = \frac{b}{2a^2}, \quad \frac{\partial x_0}{\partial b} = -\frac{1}{2a} \tag{A.20}$$

where the parameter uncertainties as well as $\mathrm{cov}(a,b)$ are directly determined from the covariance matrix returned from the *odr()*-function ($\sigma_i^2 = \mathrm{cov}(i,i), i = a,b$).

A.5. Spatial Resolution and Detection Efficiency

This section derives the uncertainty calculations for the spatial resolution σ_{spa} and the detection efficiency ϵ used in the analysis.

Spatial resolution The spatial resolution is determined via Eq.(6.16). Applying Eq. (A.1) results in

$$\Delta\sigma_{\mathrm{spa},i} = \frac{1}{\sigma_{\mathrm{spa},i}} \sqrt{\left(\sigma_{\mathrm{res},i}\,\Delta\sigma_{\mathrm{res},i}\right)^2 + \left(\sigma_{\mathrm{track},i}\,\Delta\sigma_{\mathrm{track},i}\right)^2} \tag{A.21}$$

where $\Delta\sigma_{\mathrm{res},i}$ and results from the respective uncertainty returned from the gaussian-fit (see Sec. A.2) except for the calculation of the spatial resolution σ_{spa} of the local tracking system where the statistical standard deviation $s_{\mathrm{res},i}$ (see Eq. (A.6)) was used as an estimator of the track residuals distributions width, here the respective uncertainty $\Delta s_{\mathrm{res},i}$ was estimated via Eq. (A.7). The uncertainty $\Delta\sigma_{\mathrm{track},i}$ is determined from the Gaussian-fit uncertainty, neglecting the uncertainty of the applied statistical method, given the large number of events used for the estimation. As the sensor performs a two-dimensional measurement in the u and v dimension the uncertainty of the final spatial resolution σ_{spa} combines to

$$\sigma_{\mathrm{spa}} = \frac{\sigma_{\mathrm{spa},u} + \sigma_{\mathrm{spa},v}}{2}. \tag{A.22}$$

accordingly the uncertainty of σ_{spa} is given by

$$\Delta\sigma_{\mathrm{spa}} = \frac{1}{2}\sqrt{\left(\Delta\sigma_{\mathrm{spa},u}\right)^2 + \left(\Delta\sigma_{\mathrm{spa},v}\right)^2}. \tag{A.23}$$

Detection efficiency Since k and n are counts from a binomial process, the efficiency is estimated as $\varepsilon = k/n$. The conventional binomial standard error becomes unreliable for efficiencies close to $\varepsilon = 0$ or $\varepsilon = 1$. Therefore, the uncertainty of the efficiency is determined using the Clopper-Pearson confidence interval, as implemented in the `TEfficiency::ClopperPearson()` method of the ROOT framework [45]. The interval boundaries are obtained from the inverse of the regularized incomplete beta function. In this work, the corresponding beta quantiles are evaluated using the `scipy.stats.beta.ppf()` function [46]. For a confidence level of $1 - \alpha = 95\%$ ($\alpha = 0.05$), the lower and upper confidence limits are given by

$$\varepsilon_{\text{low}} = B^{-1}\Big(\frac{\alpha}{2};\, k,\, n-k+1\Big)\,, \qquad \varepsilon_{\text{up}} = B^{-1}\Big(1-\frac{\alpha}{2};\, k+1,\, n-k\Big)\,, \tag{A.24}$$

where $B^{-1}(p; a, b)$ denotes the p-quantile of a Beta distribution with shape parameters a and b. The quantities ε_{low} and ε_{up} represent the lower and upper boundaries of the Clopper–Pearson confidence interval, respectively, and accordingly, the uncertainties of the efficiency ϵ.

B. Parameters

Table A.1.: Variations of the MOSS analogues front-end. Taken from [47]

	region 0	**region 1**	**region 2**	**region 3**
Top	Standard	Larger input transistor (M1)	Larger discriminator input transistor (M11)	Larger common-source transistor (M2)
Bottom	Standard	Standard	Standard	Slightly different layout

Table A.2.: Parameters of Eq. (5.1) obtained from [27]

	I_0 (m^{-2} s^{-1} sr^{-1})	n	E_0 (GeV)	$1/\epsilon$ $(\mathrm{GeV})^{-1}$	χ^2/ndf	**Data Reference**
μ at 0° sea level ($E > 0.5$ GeV)	72.5 ±0.2	3.06 ±0.03	3.87 ±0.07	1/854 (fixed)	60.8/23	Durham, UK (54.76° N, 1.57° W)

C. Geometries

Individual sensor configuration parameters for the local setup (Tab. A.3) and ELSA setup (Tab. A.4) employed for the analysis within the *Corryvreckan* framework and for the instantiation of the sensor in the local analysis framework. Positions are specified in Cartesian coordinates (x, y, z). The 180° orientation flip in the tb regions is only considered in the *Corryvreckan* framework, to reflect that the pixel addresses in the are inverted in the uv-plane in relation to the bb regions. In addition to the individual initial configuration file parameters, the pixels masked by the `[MaskCreator]` and used in the analysis are also listed. SCI denotes the respective scintillators. The sensor position uncertainty was neglected, as an alignment procedure was performed before performing a precision analysis

Table A.3.: Individual sensor configuration parameters for the local setup employed for the analysis within the *Corryvreckan* framework and for the instantiation of the sensor in the local analysis framework. Positions, Orientation, Masked Pixels, and ROI are listed for all regions.

ID	**x** (μm)	**y** (μm)	**z** (mm)	**Orientation** (deg)	**Masked Pixels**	**ROI** (col × row)
bb_reg0_0	5406.5	9881.125	0.00	(0, 0, 0)	2	[0−320] × [0−220]
bb_reg0_1	5406.5	9881.125	−22.50	(0, 0, 0)	1	[0−320] × [0−220]
bb_reg0_2	5406.5	9881.125	−47.38	(0, 0, 0)	0	[0−320] × [0−220]
bb_reg0_3	5406.5	9881.125	−80.93	(0, 0, 0)	2	[0−320] × [0−220]
bb_reg1_0	11652.5	9881.125	0.00	(0, 0, 0)	1	[0−320] × [0−220]
bb_reg1_1	11652.5	9881.125	−22.50	(0, 0, 0)	3	[0−320] × [0−220]
bb_reg1_2	11652.5	9881.125	−47.38	(0, 0, 0)	4	[0−320] × [0−220]
bb_reg1_3	11652.5	9881.125	−80.93	(0, 0, 0)	1	[0−320] × [0−220]
bb_reg2_0	17898.5	9881.125	0.00	(0, 0, 0)	3	[0−320] × [0−220]
bb_reg2_1	17898.5	9881.125	−22.50	(0, 0, 0)	0	[0−320] × [0−220]
bb_reg2_2	17898.5	9881.125	−47.38	(0, 0, 0)	2	[0−320] × [0−220]
bb_reg2_3	17898.5	9881.125	−80.93	(0, 0, 0)	1	[0−320] × [0−220]
bb_reg3_0	24144.5	9881.125	0.00	(0, 0, 0)	2	[0−320] × [0−220]
bb_reg3_1	24144.5	9881.125	−22.50	(0, 0, 0)	1	[0−320] × [0−220]
bb_reg3_2	24144.5	9881.125	−47.38	(0, 0, 0)	2	[0−320] × [0−220]
bb_reg3_3	24144.5	9881.125	−80.93	(0, 0, 0)	3	[0−320] × [0−220]
tb_reg0_0	5418.45	4121.125	0.00	(180, 0, 0)	1	[0−256] × [0−170]
tb_reg0_1	5418.45	4121.125	−22.50	(180, 0, 0)	2	[0−256] × [0−170]
tb_reg0_2	5418.45	4121.125	−47.38	(180, 0, 0)	3	[0−256] × [0−170]
tb_reg0_3	5418.45	4121.125	−80.93	(180, 0, 0)	1	[0−256] × [0−170]
tb_reg1_0	11650.95	4121.125	0.00	(180, 0, 0)	0	[0−256] × [0−170]

Table A.3.: Individual sensor configuration parameters for the local setup (Continued)

ID	x (μm)	y (μm)	z (mm)	Orientation (deg)	Masked Pixels	ROI (col × row
tb_reg1_1	11650.95	4121.125	−22.50	(180, 0, 0)	0	[0−256] × [0−
tb_reg1_2	11650.95	4121.125	−47.38	(180, 0, 0)	0	[0−256] × [0−
tb_reg1_3	11650.95	4121.125	−80.93	(180, 0, 0)	0	[0−256] × [0−
tb_reg2_0	17883.45	4121.125	0.00	(180, 0, 0)	1	[0−256] × [0−
tb_reg2_2	17883.45	4121.125	−47.38	(180, 0, 0)	0	[0−256] × [0−
tb_reg2_3	17883.45	4121.125	−80.93	(180, 0, 0)	0	[0−256] × [0−
tb_reg3_0	24115.95	4121.125	0.00	(180, 0, 0)	0	[0−256] × [0−
tb_reg3_1	24115.95	4121.125	−22.50	(180, 0, 0)	0	[0−256] × [0−
tb_reg3_2	24115.95	4121.125	−47.38	(180, 0, 0)	0	[0−256] × [0−
tb_reg3_3	24115.95	4121.125	−80.93	(180, 0, 0)	0	[0−256] × [0−
SCI0	14.7755	7	−122.185	(0,0,0)	–	–
SCI1	14.7755	7	49.345	(0,0,0)	–	–

Table A.4.: Individual sensor configuration parameters for the setup used at ELSA employed for the analysis within the *Corryvreckan* framework and for the instantiation of the sensor in the local analysis framework. Positions, Orientation, Masked Pixels, and ROI are listed for all regions.

ID	x (μm)	y (μm)	z (mm)	Orientation (deg)	Masked Pixels	ROI (col × row)
bb_reg0_0	5406.5	9881.125	0.00	(0, 0, 0)	1	[0−320] × [0−2
bb_reg0_1	5406.5	9881.125	−25.00	(0, 0, 0)	4	[0−320] × [0−2
bb_reg0_2	5406.5	9881.125	−50.00	(0, 0, 0)	1	[0−320] × [0−2
bb_reg0_3	5406.5	9881.125	−75.00	(0, 0, 0)	1	[0−320] × [0−2
bb_reg0_4	5406.5	9881.125	−100.00	(0, 0, 0)	2	[0−320] × [0−2
bb_reg0_5	5406.5	9881.125	−125.00	(0, 0, 0)	2	[0−320] × [0−2
bb_reg0_6	5406.5	9881.125	−150.00	(0, 0, 0)	0	[0−320] × [0−2
bb_reg1_0	11652.5	9881.125	0.00	(0, 0, 0)	0	[0−320] × [0−2
bb_reg1_1	11652.5	9881.125	−25.00	(0, 0, 0)	1	[0−320] × [0−2
bb_reg1_2	11652.5	9881.125	−50.00	(0, 0, 0)	0	[0−320] × [0−2
bb_reg1_3	11652.5	9881.125	−75.00	(0, 0, 0)	0	[0−320] × [0−2
bb_reg1_4	11652.5	9881.125	−100.00	(0, 0, 0)	2	[0−320] × [0−2
bb_reg1_5	11652.5	9881.125	−125.00	(0, 0, 0)	1	[0−320] × [0−2
bb_reg1_6	11652.5	9881.125	−150.00	(0, 0, 0)	1	[0−320] × [0−2
bb_reg2_0	17898.5	9881.125	0.00	(0, 0, 0)	1	[0−320] × [0−2
bb_reg2_1	17898.5	9881.125	−25.00	(0, 0, 0)	1	[0−320] × [0−2

Table A.4.: Individual sensor configuration parameters for the setup used at ELSA (Continued)

ID	**x** (μm)	**y** (μm)	**z** (mm)	**Orientation** (deg)	**Masked Pixels**	**ROI** (col × row)
bb_reg2_2	17898.5	9881.125	−50.00	(0, 0, 0)	0	[0−320] × [0−220]
bb_reg2_3	17898.5	9881.125	−75.00	(0, 0, 0)	0	[0−320] × [0−220]
bb_reg2_4	17898.5	9881.125	−100.00	(0, 0, 0)	1	[0−320] × [0−220]
bb_reg2_5	17898.5	9881.125	−125.00	(0, 0, 0)	1	[0−320] × [0−220]
bb_reg2_6	17898.5	9881.125	−150.00	(0, 0, 0)	1	[0−320] × [0−220]
bb_reg3_0	24144.5	9881.125	0.00	(0, 0, 0)	2	[0−320] × [0−220]
bb_reg3_1	24144.5	9881.125	−25.00	(0, 0, 0)	3	[0−320] × [0−220]
bb_reg3_2	24144.5	9881.125	−50.00	(0, 0, 0)	0	[0−320] × [0−220]
bb_reg3_3	24144.5	9881.125	−75.00	(0, 0, 0)	0	[0−320] × [0−220]
bb_reg3_4	24144.5	9881.125	−100.00	(0, 0, 0)	2	[0−320] × [0−220]
bb_reg3_5	24144.5	9881.125	−125.00	(0, 0, 0)	0	[0−320] × [0−220]
bb_reg3_6	24144.5	9881.125	−150.00	(0, 0, 0)	2	[0−320] × [0−220]
tb_reg0_0	5418.45	4121.125	0.00	(180, 0, 0)	1	[0−256] × [0−170]
tb_reg0_1	5418.45	4121.125	−25.00	(180, 0, 0)	1	[0−256] × [0−170]
tb_reg0_2	5418.45	4121.125	−50.00	(180, 0, 0)	0	[0−256] × [0−170]
tb_reg0_3	5418.45	4121.125	−75.00	(180, 0, 0)	0	[0−256] × [0−170]
tb_reg0_4	5418.45	4121.125	−100.00	(180, 0, 0)	0	[0−256] × [0−170]
tb_reg0_5	5418.45	4121.125	−125.00	(180, 0, 0)	0	[0−256] × [0−170]
tb_reg0_6	5418.45	4121.125	−150.00	(180, 0, 0)	0	[0−256] × [0−170]
tb_reg1_0	11650.95	4121.125	0.00	(180, 0, 0)	1	[0−256] × [0−170]
tb_reg1_1	11650.95	4121.125	−25.00	(180, 0, 0)	1	[0−256] × [0−170]
tb_reg1_2	11650.95	4121.125	−50.00	(180, 0, 0)	0	[0−256] × [0−170]
tb_reg1_3	11650.95	4121.125	−75.00	(180, 0, 0)	0	[0−256] × [0−170]
tb_reg1_4	11650.95	4121.125	−100.00	(180, 0, 0)	0	[0−256] × [0−170]
tb_reg1_5	11650.95	4121.125	−125.00	(180, 0, 0)	0	[0−256] × [0−170]
tb_reg1_6	11650.95	4121.125	−150.00	(180, 0, 0)	0	[0−256] × [0−170]
tb_reg2_0	17883.45	4121.125	0.00	(180, 0, 0)	1	[0−256] × [0−170]
tb_reg2_1	17883.45	4121.125	−25.00	(180, 0, 0)	2	[0−256] × [0−170]
tb_reg2_2	17883.45	4121.125	−50.00	(180, 0, 0)	0	[0−256] × [0−170]
tb_reg2_3	17883.45	4121.125	−75.00	(180, 0, 0)	0	[0−256] × [0−170]
tb_reg2_4	17883.45	4121.125	−100.00	(180, 0, 0)	0	[0−256] × [0−170]
tb_reg2_5	17883.45	4121.125	−125.00	(180, 0, 0)	0	[0−256] × [0−170]
tb_reg2_6	17883.45	4121.125	−150.00	(180, 0, 0)	1	[0−256] × [0−170]
tb_reg3_0	24115.95	4121.125	0.00	(180, 0, 0)	1	[0−256] × [0−170]
tb_reg3_1	24115.95	4121.125	−25.00	(180, 0, 0)	11	[0−256] × [0−170]
tb_reg3_2	24115.95	4121.125	−50.00	(180, 0, 0)	2	[0−256] × [0−170]

Table A.4.: Individual sensor configuration parameters for the setup used at ELSA (Continued)

ID	**x** (μm)	**y** (μm)	**z** (mm)	**Orientation** (deg)	**Masked Pixels**	**ROI** (col × row)
`tb_reg3_3`	24115.95	4121.125	−75.00	(180, 0, 0)	0	[0−256] × [0−1
`tb_reg3_4`	24115.95	4121.125	−100.00	(180, 0, 0)	2	[0−256] × [0−1
`tb_reg3_5`	24115.95	4121.125	−125.00	(180, 0, 0)	1	[0−256] × [0−1
`tb_reg3_6`	24115.95	4121.125	−150.00	(180, 0, 0)	2	[0−256] × [0−1
SCI0	14.7755	7	−175.00	(0,0,0)	–	–
SCI1	14.7755	7	50.00	(0,0,0)	–	–

D. Sensor Characterization

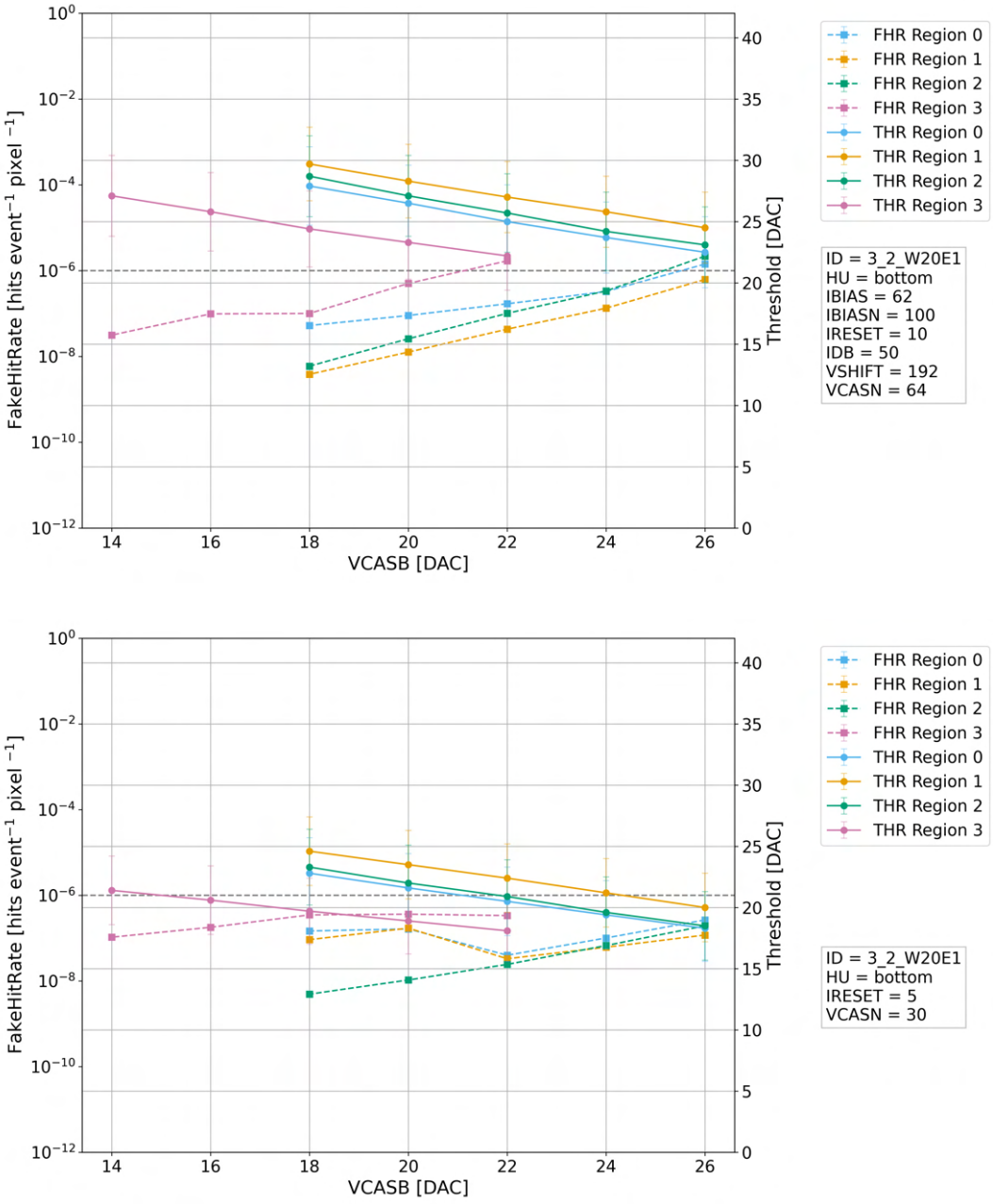


Figure A.1.: Results of THR and FHR scans of the four bb regions of the babyMOSS-3_2_W20E1 sensor, for two sets of fundamental transistor settings (see tab. 5.1 and varying VCASB at room temperature.

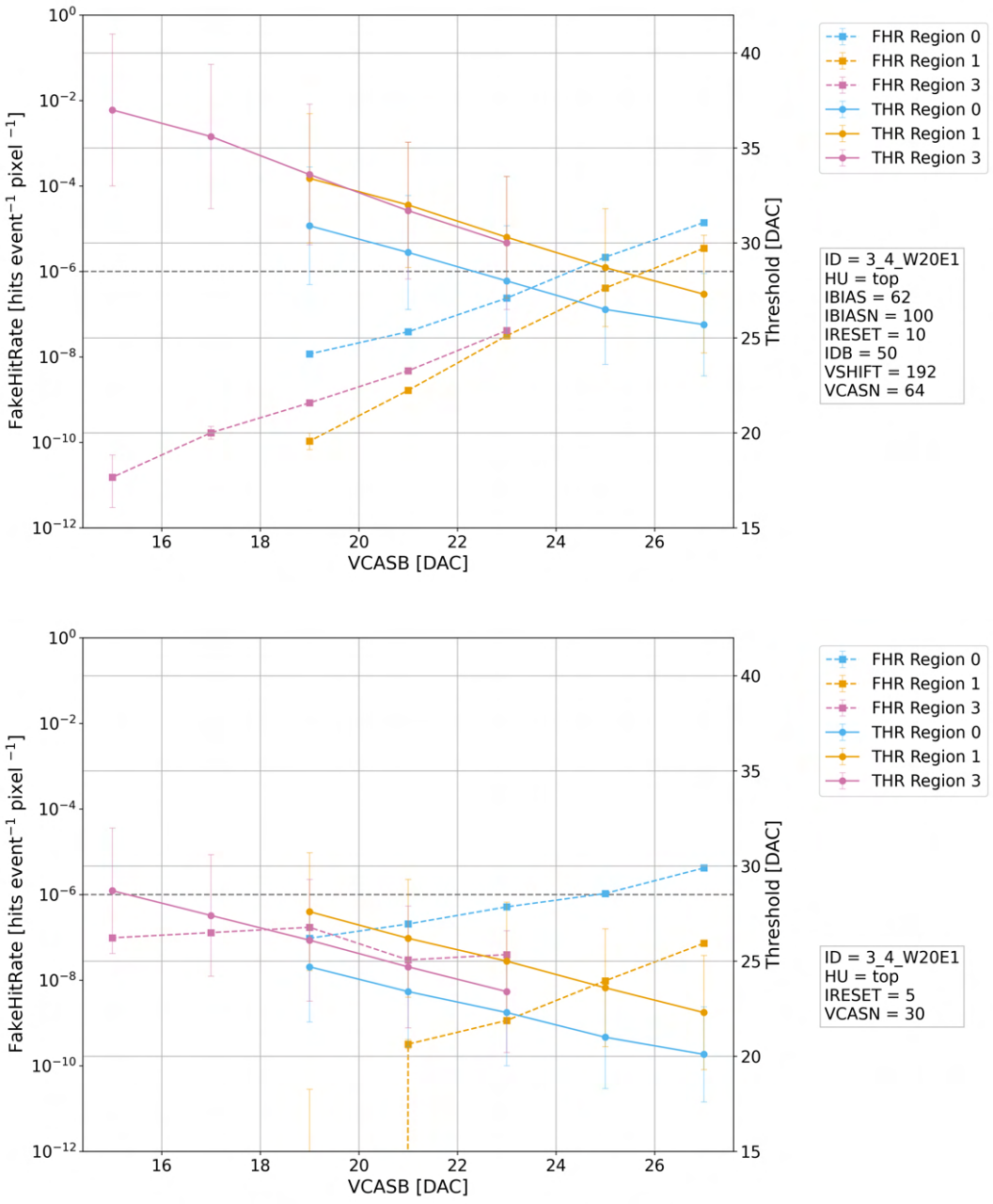


Figure A.2.: Results of THR and FHR scans of the four tb regions of the babyMOSS-3_4_W20E1 sensor, for two sets of fundamental transistor settings (see tab. 5.1 and varying VCASB at room temperature.

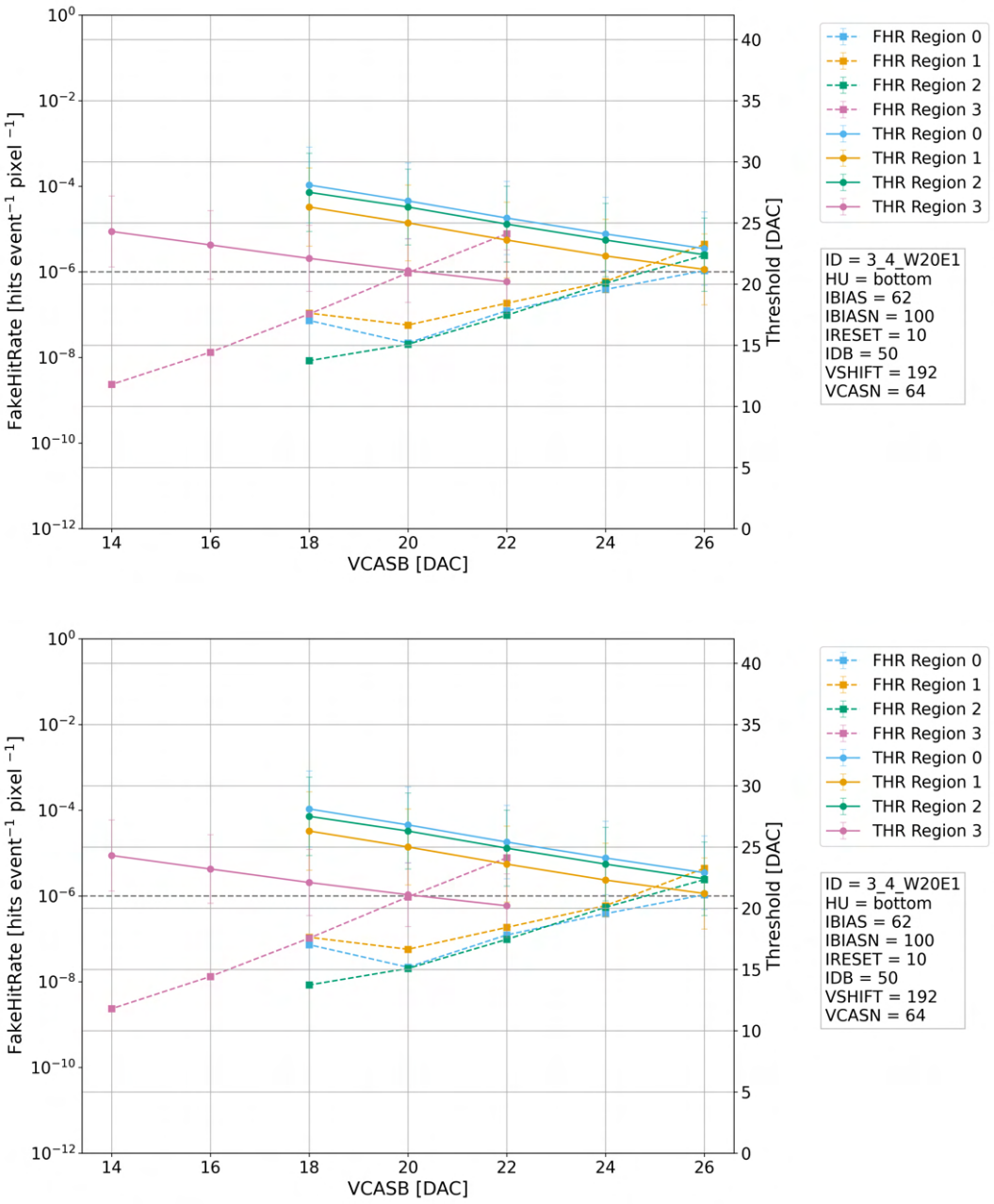


Figure A.3.: Results of THR and FHR scans of the four bb regions of the babyMOSS-3_4_W20E1 sensor, for two sets of fundamental transistor settings (see tab. 5.1 and varying VCASB at room temperature.

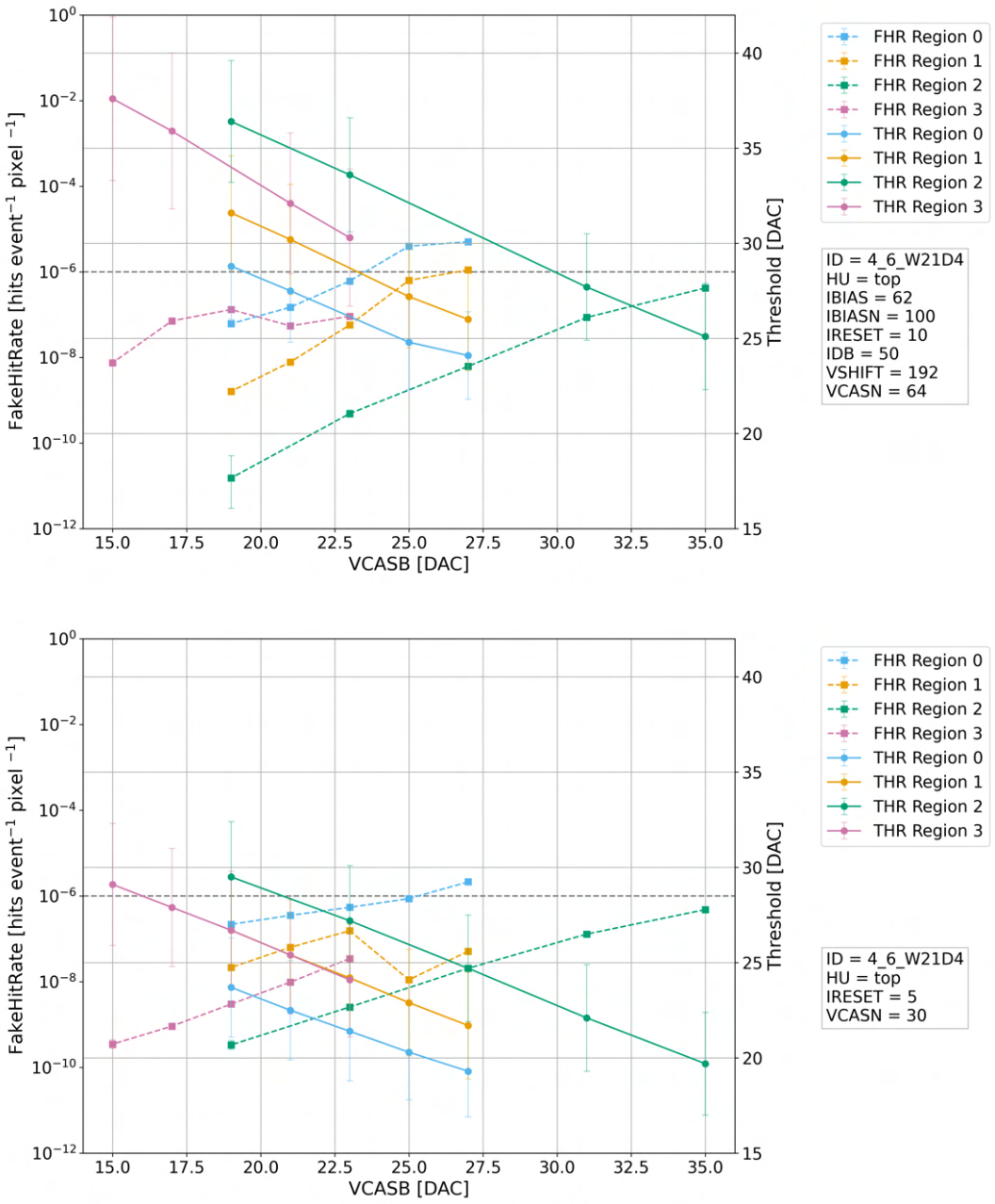


Figure A.4.: Results of THR and FHR scans of the four tb regions of the babyMOSS-4_6_W20E1 sensor, for two sets of fundamental transistor settings (see tab. 5.1 and varying VCASB at room temperature.

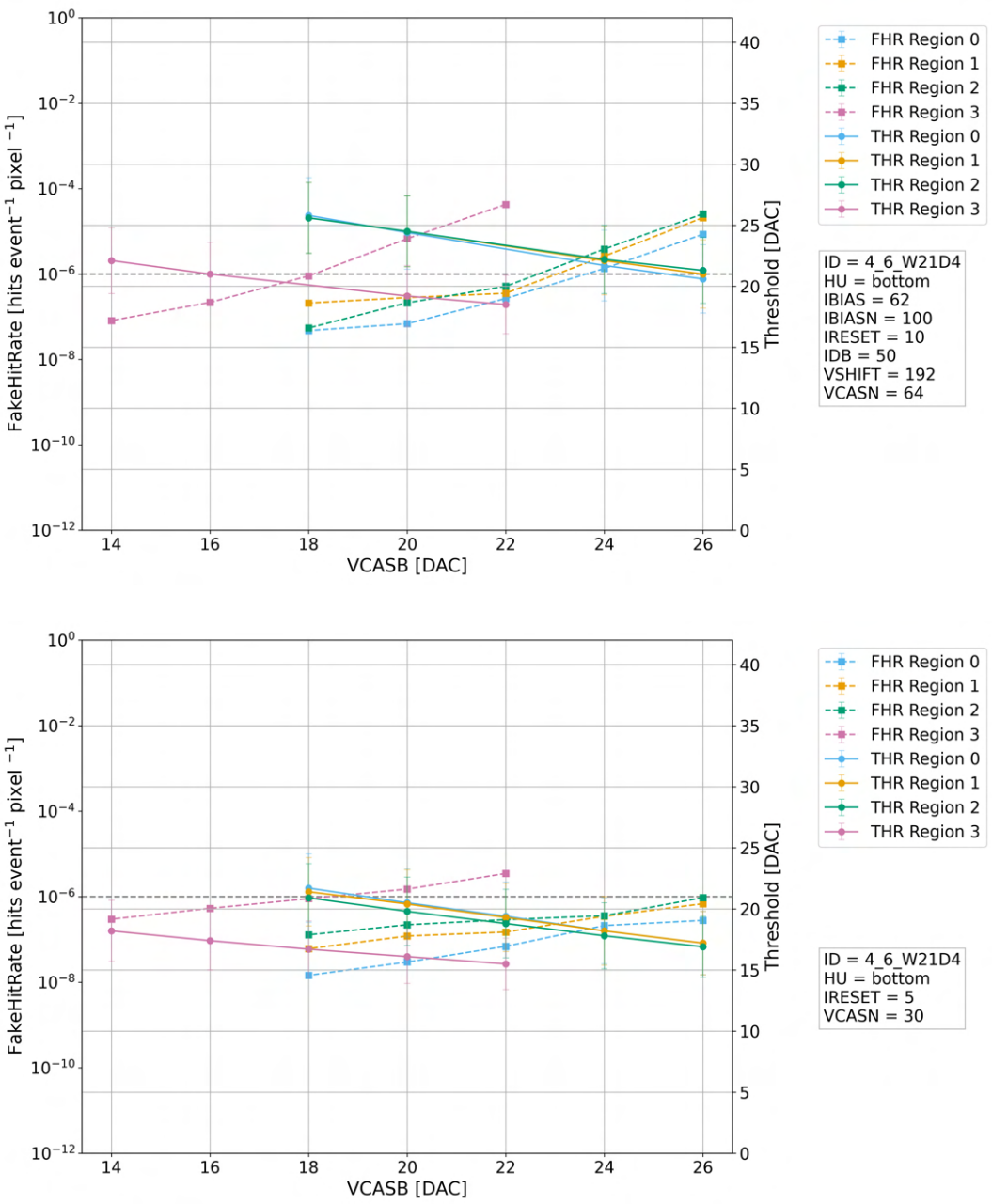


Figure A.5.: Results of THR and FHR scans of the four bb regions of the babyMOSS-4_6_W20E1 sensor, for two sets of fundamental transistor settings (see tab. 5.1 and varying VCASB at room temperature.

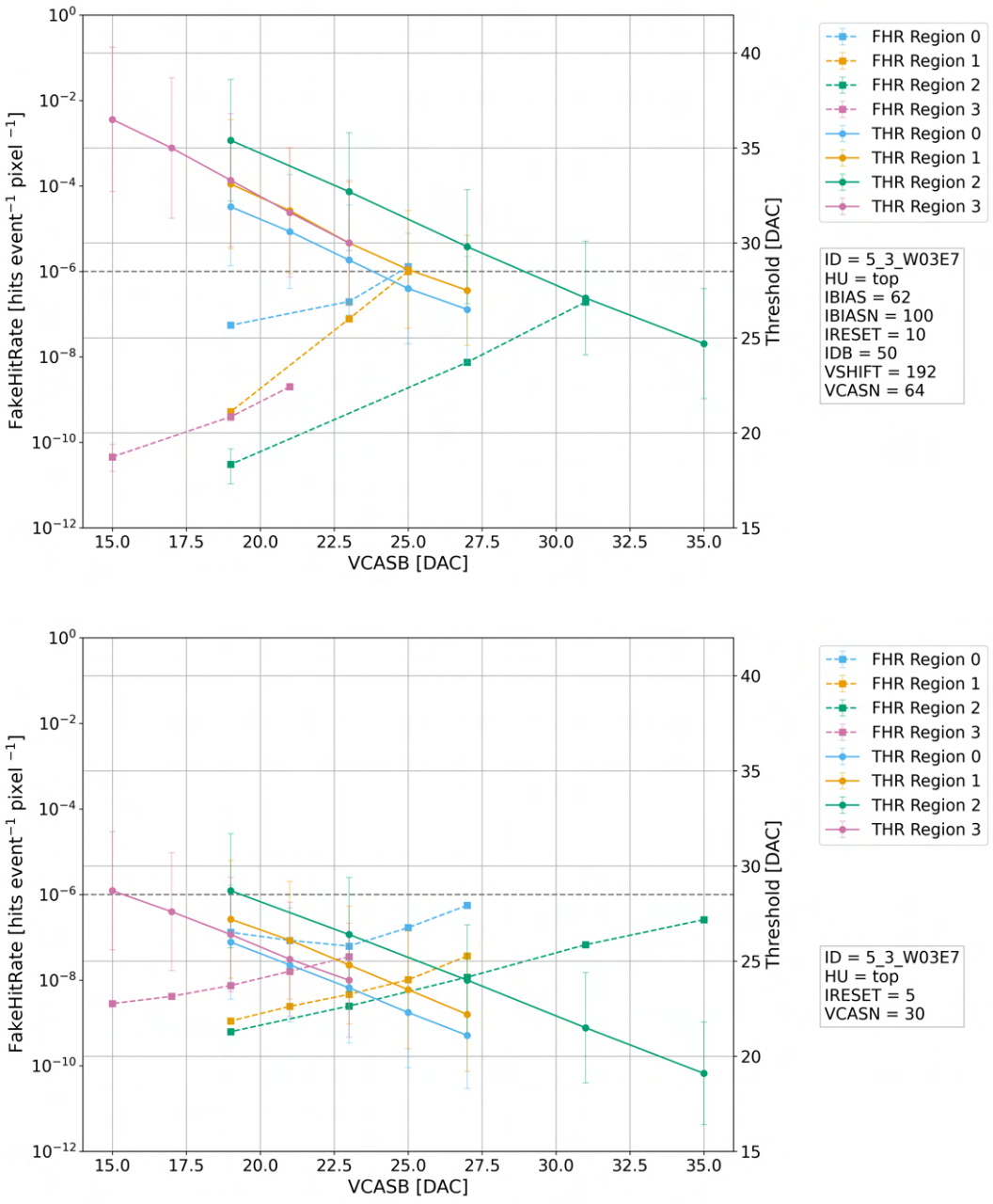


Figure A.6.: Results of THR and FHR scans of the four tb regions of the babyMOSS-5_3_W03E7 sensor, for two sets of fundamental transistor settings (see tab. 5.1 and varying VCASB at room temperature.

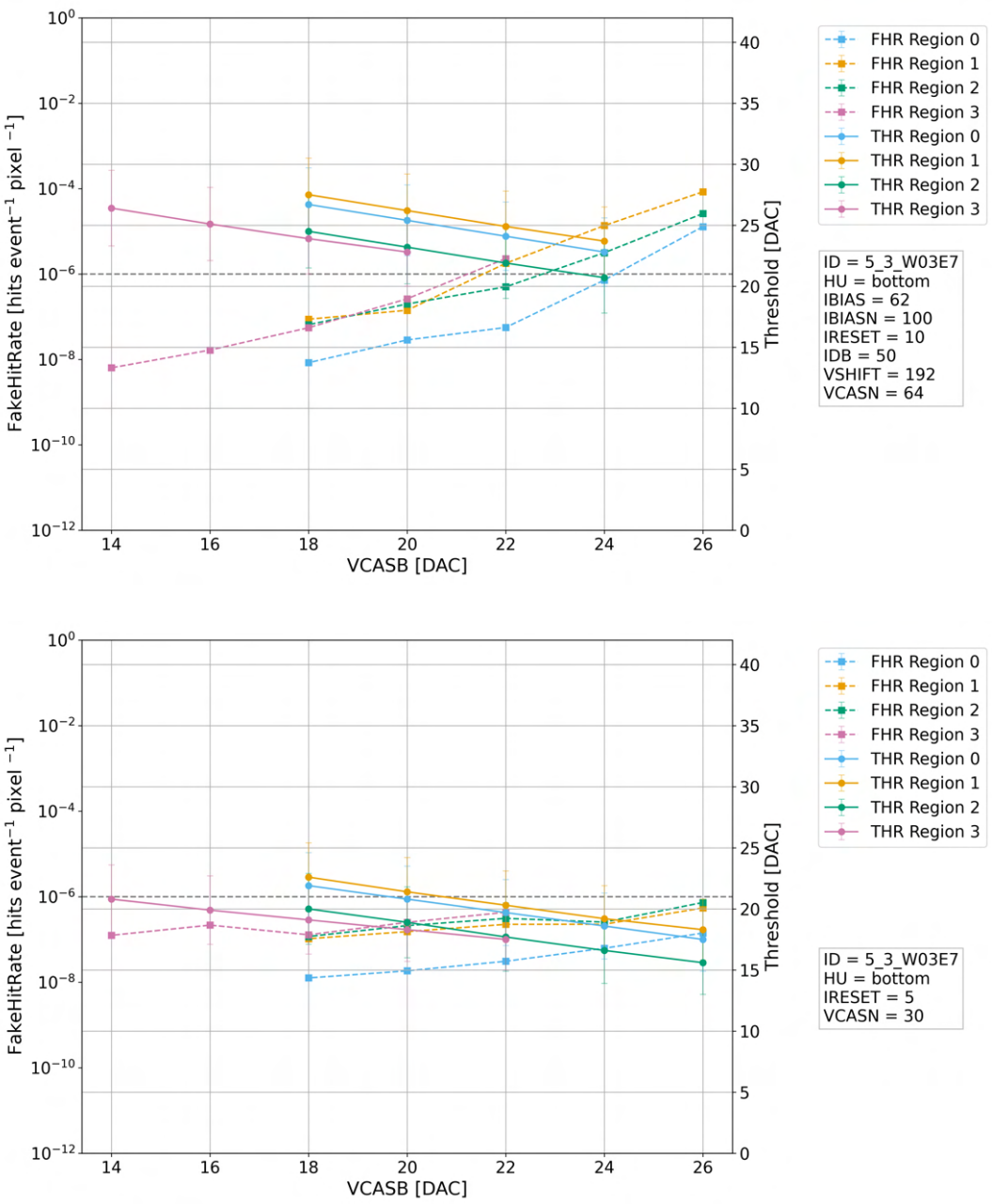


Figure A.7.: Results of THR and FHR scans of the four bb regions of the babyMOSS-5_3_W03E7 sensor, for two sets of fundamental transistor settings (see tab. 5.1 and varying VCASB at room temperature.

Table A.5.: VCASB settings for all four babyMOSS layers of the local setup

Sensor (DAQ board)	Region	tb VCASB	bb VCASB
Raiser 5_3 (W03E7) DAQ-0009012D0D901639	0	26	26
	1	26	26
	2	35	26
	3	26	22
Raiser 3_4 (W20E1) DAQ-0009012D0D8E0822	0	24	26
	1	27	26
	2	–	26
	3	23	22
Raiser 4_6 (W21D4) DAQ-0009012D0D902439	0	25	26
	1	27	26
	2	35	26
	3	23	18
Raiser 3_2 (W20E1) DAQ-0009012D0D902339	0	27	26
	1	27	26
	2	35	26
	3	23	22

E. Alignment

E.1. Local Setup

Table A.6.: Alignment stages for the local setup

Stage	DUT Align.	Max Iter.	Conv. Thr. (A/B)	χ^2_r Cut	Spatial Cut	max. DUT Residual (A/B)	Min hit layers
TelCoarse	No	100	10^{-2}	2000	1.00	–	3
TelFine	No	150	$5 \cdot 10^{-3}$	100	0.30	–	3
TelSuperFine	No	500	$10^{-6}/5 \cdot 10^{-4}$	10	0.05	–	3
DUTCoarse	Yes	50	10^{-2}	50	1.00	1.00	3
DUTFine	Yes	100	10^{-5}	50	0.10	0.50	3
DUTSuperFine	Yes	100	$10^{-6}/10^{-5}$	10	0.05	0.05/0.035	3

Common parameters for all stages: Reference layer 0 and DUT layer 1.

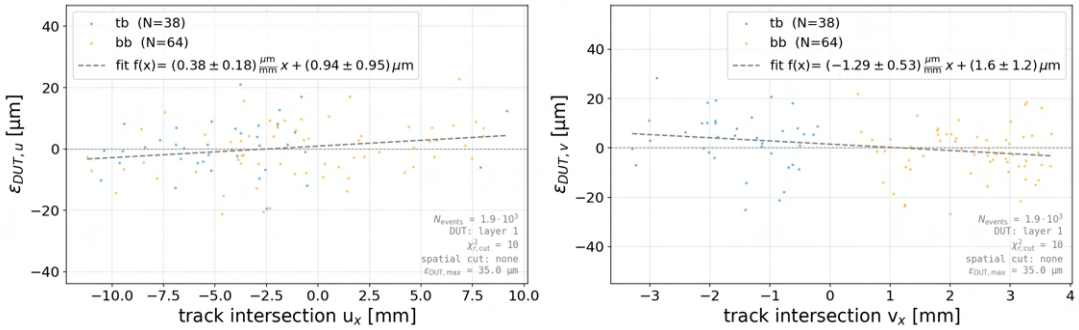


Figure A.8.: DUT residual ε_{DUT} of track intersection q_m and measured position q_x plotted against the point of track intersection q_m in the respective dimension for the measurement of atmospheric muons using the local setup. For the data recorded with the local setup, obtained with Tab.A.6(A)

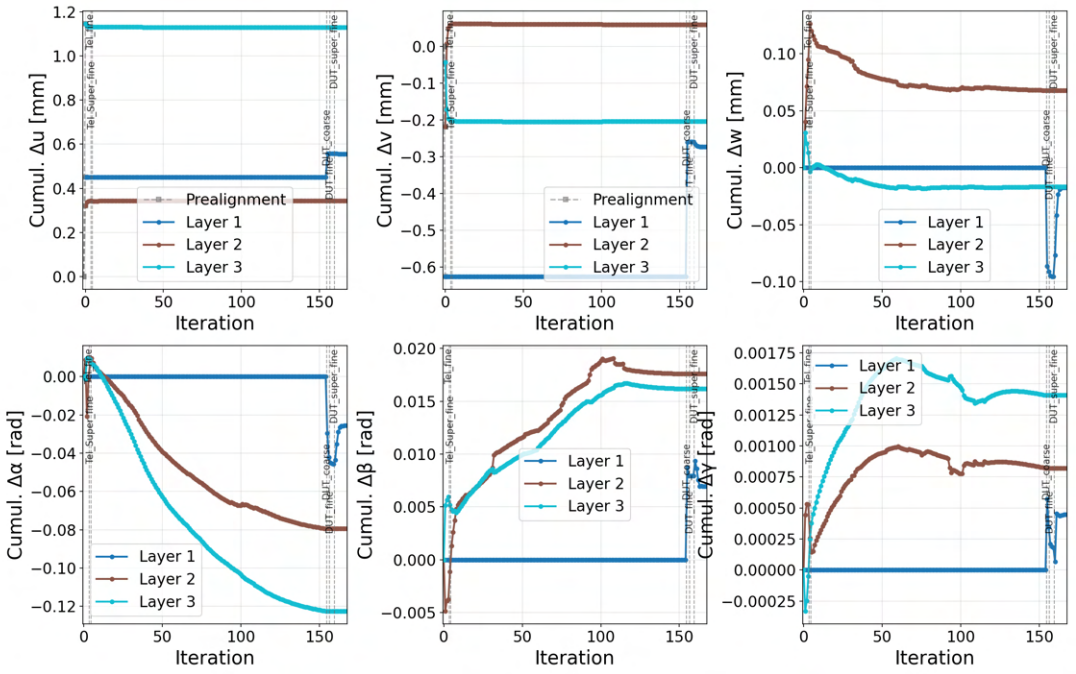


Figure A.9.: Incremental evolution of the alignment parameters for the alignment of the local setup using atmospheric muons. The horizontal dotted lines indicate the true misalignment parameters defining $\Delta R_{\text{mis,layer}}$ and $r_{0,\text{mis,layer}}$. The vertical grey dotted lines mark the boundaries between the individual alignment stages. Layer 0 serves as the reference layer for the alignment. For the data recorded with the local setup, obtained with Tab.A.6(A)

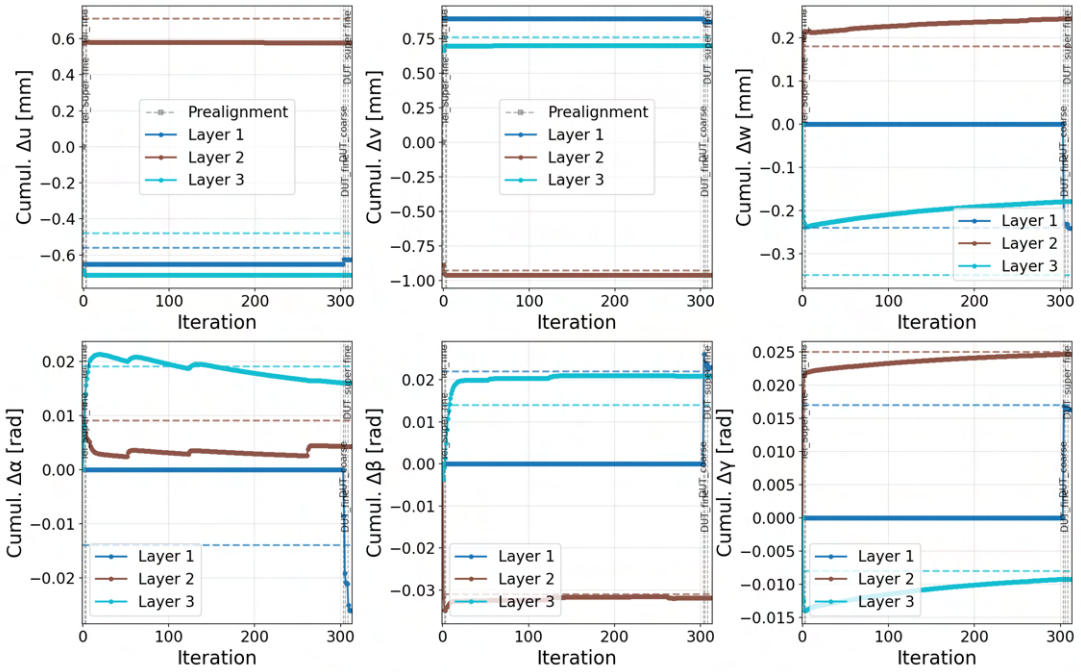


Figure A.10.: Incremental evolution of the alignment parameters for the alignment of the local setup using 300 simulated atmospheric muon events. The horizontal dotted lines indicate the true misalignment parameters defining $\Delta R_{\text{mis,layer}}$ and $r_{0,\text{mis,layer}}$. The vertical grey dotted lines mark the boundaries between the individual alignment stages.

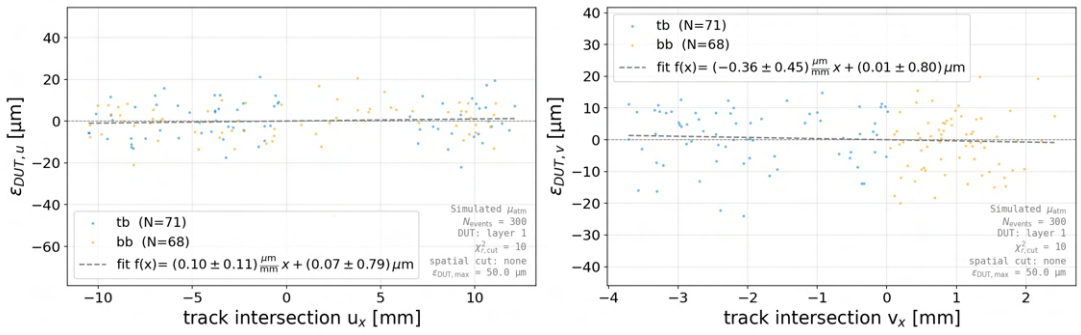


Figure A.11.: DUT residual ε_{DUT} of track intersection q_m and measured position q_x plotted against the point of track intersection q_m in the respective dimension for the alignment of the local setup using 300 simulated atmospheric muon events, obtained with Tab.A.6(A)

E.2. ELSA

Table A.7.: Alignment stages for the setup used at ELSA

Stage	DUT Align.	Max Iter.	Conv. Thr.	χ^2_r Cut	Spatial Cut	max. DUT Residual	Min hit layers
TelCoarse	No	100	10^{-2}	1000	1.00	–	6
TelFine	No	150	$5 \cdot 10^{-3}$	50	0.10	–	6
TelSuperFine	No	150	10^{-5}	3	0.05	–	6
DUTCoarse	Yes	50	10^{-2}	50	1.00	1.00	6
DUTFine	Yes	100	10^{-4}	25	0.10	0.10	6
DUTSuperFine	Yes	100	10^{-5}	3	0.025	0.03	6

Common parameters for all stages: Reference layer 0 and DUT layer 3.

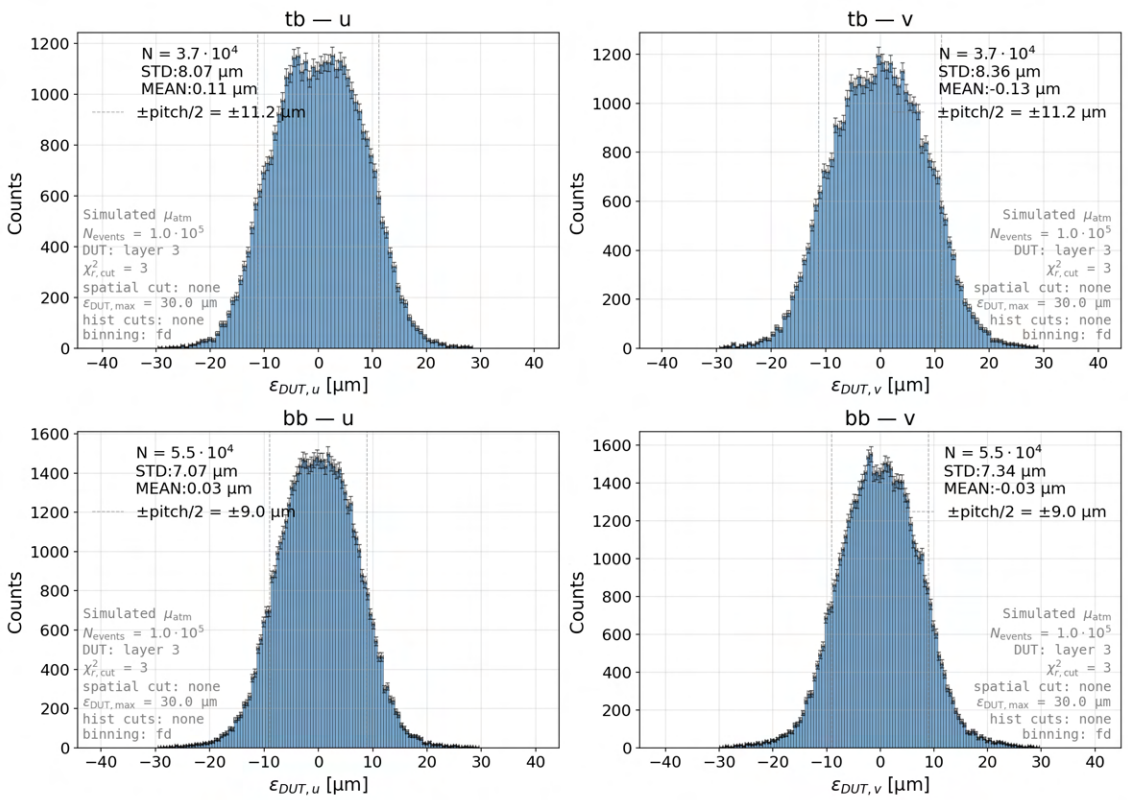


Figure A.12.: Unbiased residuals $\varepsilon_{\mathrm{DUT,traj}}$ between the simulated intersection point within the layer and the reconstructed track in local detector coordinates for the two HUs after the alignment of all three non-reference planes, obtained using $1 \cdot 10^5$ simulated ELSA events.

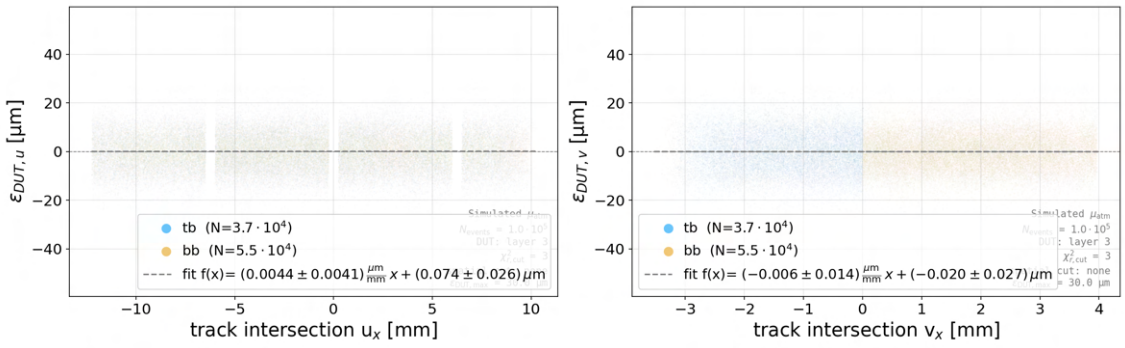


Figure A.13.: DUT residual ε_{DUT} of track intersection q_m and simulated measured position q_x plotted against the point of track intersection q_m in the respective dimension for the simulated alignment for the setup used at ELSA.

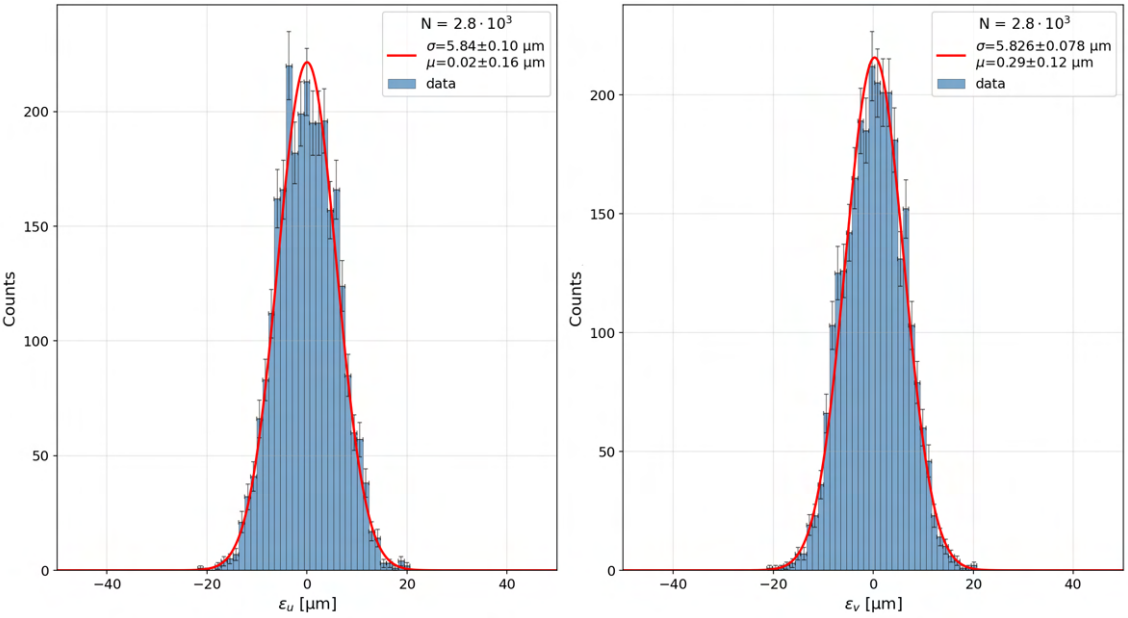


Figure A.14.: Exemplary track residual distribution $\varepsilon_{DUT,track}$ of bb region 0 of a dataset from the THR-scan carried out within the February 2025 ITS3 testbeam campaign at ELSA

Acknowledgments

First and foremost, I would like to thank my supervisor, Prof. Anton Andronic, who has guided me throughout this work and who is always committed to giving his students every opportunity to gain practical experience, broaden their knowledge and explore new ideas. I am equally grateful to the organisers of the various test beam campaigns, Iaroslav and Bogdan, from whom I learnt so much about this unique kind of work during these intensive periods. My thanks also go to Berkin, who made his work available as the foundation for my programme, and to Philip, who kept me constantly up to date and took on the task of organising the long, arduous journey of the babyMOSS from Bonn back to Münster. Thank you all for being there for me not only during the test beam campaigns, but also at any time when I had questions.
Also I would like to thank my inoffical supervisors Nicolas and Tim, who supported me during my first babyMOSS measurements, my first confusing journey to CERN, and on many other occasions.

My gratitude likewise goes to my test beam companions, Alex—who is in fact an organiser himself—and Marian, with whom I have learned so much and shared so many experiences, from the very first test beam to the very last and everything in between. I would also like to thank my office colleagues Alexander, Jesse and Anna, with whom I could always have a good discussion – whether technical or not – and who consistently supported me, either with their expertise or by working through problems together.

In addition to all these people, I would also like to give a very special thank you to my girlfriend Lea, without whose support none of this would have been possible and for whom I could never fully list all the things she has done for me. Without you, this thesis—and certainly much of the journey leading up to it—would not have been possible. Thank you for inspiring and supporting me so much, and for letting me discover this wonderful world together with you.

I would also like to express my heartfelt appreciation to my parents, Stefan and Birgit, who

have opened every door for me—through their support and advice, as well as through their unique way of looking at the world – and, of course, to my sister Amelie, who is always there for me with great empathy and whose courage and positivity I admire enormously.

For the improvement of the readability as well as for grammar and spell checking the tools [48],[49] and [29] were utilized during the preparation of this thesis.

Declaration of Academic Integrity

1 hereby confirm that this thesis, entitled

Development and Implementation of a Particle Tracking System Based on Monolithic Active Pixel Sensors

is solely my own work and that I have used no sources or aids other than the ones stated. All passages in my thesis for which other sources, including electronic media and AI Tools, have been used, be it direct quotes or content references, have been acknowledged as such and the sources cited. I am aware that plagiarism is considered an act of deception which can result in sanction in accordance with the examination regulations.

Münster, June 29, 2026
place, date

Lennart Halstenberg

I consent to having my thesis cross-checked with other texts to identify possible similarities and to having it stored in a database for this purpose.
I confirm that I have not submitted the following thesis in part or whole as an examination paper before.

Münster, June 29, 2026
place, date

Lennart Halstenberg